

# Surface brightness profiles and structural parameters for 53 rich stellar clusters in the Large Magellanic Cloud

A. D. Mackey<sup>1\*</sup> and G. F. Gilmore<sup>1</sup>

<sup>1</sup>*Institute of Astronomy, University of Cambridge, Madingley Road, Cambridge CB3 0HA*

Accepted – Received –

## ABSTRACT

We have compiled a pseudo-snapshot data set of two-colour observations from the *Hubble Space Telescope* archive for a sample of 53 rich LMC clusters with ages  $10^6 - 10^{10}$  yr. We present surface brightness profiles for the entire sample, and derive structural parameters for each cluster, including core radii, and luminosity and mass estimates. Because we expect the results presented here to form the basis for several further projects, we describe in detail the data reduction and surface brightness profile construction processes, and compare our results with those of previous ground-based studies.

The surface brightness profiles show a large amount of detail, including irregularities in the profiles of young clusters (such as bumps, dips, and sharp shoulders), and evidence for both double clusters and post core-collapse (PCC) clusters. In particular we find power-law profiles in the inner regions of several candidate PCC clusters, with slopes of approximately  $-0.7$ , but showing considerable variation. We estimate that  $20 \pm 7$  per cent of the old cluster population of the LMC has entered PCC evolution, a similar fraction to that for the Galactic globular cluster system. In addition, we examine the profile of R136 in detail and show that it is probably not a PCC cluster.

We also observe a trend in core radius with age that has been discovered and discussed in several previous publications by different authors. Our diagram has better resolution however, and appears to show a bifurcation at several hundred Myr. We argue that this observed relationship reflects true physical evolution in LMC clusters, with some experiencing small scale core expansion due to mass loss, and others large scale expansion due to some unidentified characteristic or physical process.

**Key words:** galaxies: star clusters – Magellanic Clouds – globular clusters: general – stars: statistics

## 1 INTRODUCTION

The star cluster system of the Large Magellanic Cloud (LMC) is unique in containing rich star clusters of masses comparable to Galactic globular clusters, but covering a wide age range ( $10^6 - 10^{10}$  yr) and being close enough for detailed observation. It therefore offers a seemingly perfect opportunity for studies of all aspects of star cluster astronomy, from cluster formation, evolution and dynamics, to luminosity and mass function studies, as well as investigations which shed light on the evolution history of the entire LMC. It is surprising then, that while catalogues of high resolution surface brightness profiles and structural parameters exist for Galactic globular clusters (e.g., Trager, King & Djorgovski (1995)), no such uniform catalogue exists for a large sample of the rich LMC clusters.

There has however been some considerable activity in this field. In particular, significant numbers of surface brightness and/or

density profiles have been published for young and intermediate age clusters (Elson, Fall & Freeman (1987), hereafter EFF87; Elson, Freeman & Lauer (1989); Elson (1991), hereafter E91; Elson (1992)); old clusters (Mateo 1987); and clusters with different spatial distributions – in the LMC disk (Kontizas, Chrysovergis & Kontizas (1987a)); in the LMC disk and within 5 kpc of the rotation centre (Chrysovergis, Kontizas & Kontizas (1989)); and in the LMC halo (Kontizas, Hadjidimitriou & Kontizas (1987b); Metaxa, Kontizas & Kontizas (1988)). These studies are all ground-based and therefore suffer from problems – primarily crowding and seeing related – which limit their resolution, particularly in the inner regions of clusters. This in turn renders the derivation of key parameters, such as the core radius, rather uncertain. In addition, each set of authors uses a different data set and makes different measurements (e.g., Elson and collaborators construct  $V$ -band surface brightness profiles; Mateo uses  $B$ -band profiles; and Kontizas and collaborators use number density profiles), so most of the important derived values are not strictly comparable between studies.

We have taken advantage of the presence of a large number of

\* E-mail: dmackey@ast.cam.ac.uk

observations of rich LMC clusters in the *Hubble Space Telescope* (*HST*) archive to compile a high resolution data set, unaffected by the problems which beset ground-based studies. Rather than simply providing an atlas of surface brightness profiles from this data, the aim of the present study is to obtain a statistically homogeneous set of profiles and key structural parameters for as many clusters as possible, for the purposes of differential comparison. To this end, we require a sample as free from bias as possible, and we have therefore applied a uniform selection and reduction process to the available observations. Because these procedures are rather detailed, and because we expect our measurements to form the basis of several additional projects, in this paper we discuss at length the data set and its selection (Section 2) and the reduction and profile construction processes (Sections 3 and 4 respectively). In Section 5 we present the surface brightness profiles and structural parameter measurements, compare these results with those of the authors previously mentioned, and examine some of the interesting subgroups present in the sample – such as binary clusters and post core-collapse clusters. Finally, in Section 6 we observe and discuss the relationship between core radius and age for the LMC cluster system. This relationship has previously been studied (Elson et al. (1989); E91; Elson (1992)); however our measurements are able to provide new insight into this problem.

The data presented in Tables 1, 2, 4, and 6, and the surface brightness profiles (Fig. 6) are available on-line at [http://www.ast.cam.ac.uk/STELLARPOPS/LMC\\_clusters/](http://www.ast.cam.ac.uk/STELLARPOPS/LMC_clusters/).

## 2 THE CLUSTER SAMPLE

### 2.1 Observations

The observational basis of this project is the presence in the *HST* archive of a snapshot survey of LMC (and SMC) clusters (*HST* project 5475). This data set consists of two Wide Field Planetary Camera 2 (WFPC2) exposures per cluster, through the F450W and F555W filters respectively, and with exposure times covering the range 20-300 s in F555W and 40-600 s in F450W, dependent on the age of the cluster under observation. The data were acquired between 1994 January 27 and 1994 December 25, but mostly before the WFPC2 cool-down on 1994 April 23.

Upon retrieval, we discovered that the sample was neither as large nor as varied as desired, and consequently we returned to the archive to obtain observations of as many additional clusters as possible. We located a further six suitable studies (*HST* projects 5114, 5897, 5904, 5916, 7307, and 8134), consisting of detailed observations of several clusters each. To maintain the uniformity of our selection as far as possible, we attempted to mimic the snapshot data by using only two frames per cluster, with exposure times as close as possible to the ranges described above, even though for many of the clusters from these six studies, an abundance of archival frames is available. To avoid biases such as that due to observer selection of “interesting targets,” it was necessary to limit the use of these extra frames to match the least observed clusters. This fit with our primary aim of investigating the LMC cluster system as a whole. For this purpose we required data for as large a sample of clusters as possible, but to be reduced within a reasonable time frame. Therefore, we had to balance ultimate accuracy (maximum data) for any given cluster in the sample against overall reduction time. Had our aim been simply to provide an atlas of surface brightness profiles, or to study one or two clusters in great detail, the extra data would certainly have been included. Nonetheless, we were careful

not to unnecessarily degrade the quality of our data. In cases where the neglect of additional data would have compromised our results (e.g., in extremely crowded clusters) we included minimal numbers of extra frames in order to proceed.

In the end, complete reproduction of the original snapshot data was not possible, with the only uniform choice of filters between the extra six studies being F555W and F814W. For nine clusters we retrieved both long ( $\sim 500$  s) and short ( $\sim 10$  s) exposures in order to overcome data degradation due to severe crowding and/or saturation (as mentioned above). The final cluster sample is listed in Table 1 together with the observational details<sup>†</sup>. The sample consists of 53 LMC clusters spanning the full age range. The entire sample is observed through the F555W filter, providing a unique high resolution data set. Thirty-one of the clusters are also observed through the F450W filter, with the remaining 22 clusters having F814W as their second filter – we note however that for our surface brightness profile construction process, the choice of the second colour is of little consequence.

### 2.2 Literature data

As a supplement to the above data set, and as a reference point for this and future publications, we have compiled nomenclature, position, age and metallicity data from the literature for the complete cluster sample. This information is displayed in Table 2. As with the data set construction, the emphasis is on obtaining as homogeneous a compilation as possible, while still maintaining the integrity and accuracy of the data. This means using the results of large surveys or studies for the most part, and supplementing these with the results of high quality observations where necessary. In the cases where several such high quality studies are available, we have chosen the values which represent approximately the convergence of the data. For several clusters, scarcity of information has necessitated the selection of older or lower quality data. This compilation does not purport to be a complete survey of the available literature; rather it is intended to provide a consistent set of age and metallicity estimates for use in this and subsequent projects.

#### 2.2.1 Cluster names and positions

We have taken position and nomenclature information from the Simbad Astronomical Database (<http://simbad.u-strasbg.fr/>). While almost all recognized identifiers for a cluster are included in this database, we have not compiled all such identifiers for our sample, rather only the most common. In general the principal designation is an NGC number, with the other identifiers and corresponding catalogues as follows: Hodge, (Hodge 1960); SL, (Shapley & Lindsay 1963); LW, (Lyngå & Westerlund 1963). In the Simbad database, J2000.0 positions for LMC objects are in general from the catalogue of Bica et al. (1999). Using these positions we calculate the projected angular distance  $R_{opt}$  to the optical centre of the LMC at  $\alpha = 05^h 20^m 56^s$ ,  $\delta = -69^\circ 28' 41''$  (J2000.0) (Bica et al. 1996), and the projected angular distance  $R_{rot}$  to the HI rotation curve centre at  $\alpha = 05^h 26^m 39^s$ ,  $\delta = -69^\circ 15' 36''$  (J2000.0) (Rohlf et al. 1984; Westerlund 1990). We later derive more accurate centres for each cluster; however, the literature values listed here are never substantially different from our calculated positions.

<sup>†</sup> Notes to Table 1:

<sup>a</sup> The archived images of this cluster are incorrectly labelled as NGC 2156.

<sup>b</sup> The archived images of this cluster are incorrectly labelled as SL 633.

Table 1. Cluster list and observation details.

Cluster Name	Program ID	Principal Frame				Secondary Frame			
		Filter	Data set	Date	Time (s)	Filter	Data set	Date	Time (s)
NGC1466	5897	F555W	u2xj0103t	22/10/1995	260	F814W	u2xj0101t	22/10/1995	260
NGC1651	5475	F555W	u26m0r02t	01/02/1994	120	F450W	u26m0r01t	01/02/1994	230
NGC1711	5904	F555W	u2y80502r	18/10/1997	300	F814W	u2y80504r	18/10/1997	300
NGC1718	5475	F555W	u26m0j02t	06/02/1994	120	F450W	u26m0j01t	06/02/1994	230
NGC1754	5916	F555W	u2xq0103t	21/10/1995	500	F814W	u2xq0109t	21/10/1995	600
		F555W	u2xq0101t	21/10/1995	20	F814W	u2xq0106t	21/10/1995	20
NGC1777	5475	F555W	u26m0u02t	23/11/1994	120	F450W	u26m0u01t	23/11/1994	230
NGC1786	5897	F555W	u2xj0203t	19/10/1995	260	F814W	u2xj0201t	19/10/1995	260
NGC1805	7307	F555W	u4ax0206r	25/07/1998	140	F814W	u4ax020br	25/07/1998	300
NGC1818	7307	F555W	u4ax3005r	25/09/1998	140	F814W	u4ax300cr	25/09/1998	300
NGC1831	5475	F555W	u26m1002t	27/01/1994	40	F450W	u26m1001t	27/01/1994	80
NGC1835	5916	F555W	u2xq0203t	18/10/1995	500	F814W	u2xq0209t	18/10/1995	600
		F555W	u2xq0201t	18/10/1995	20	F814W	u2xq0206t	18/10/1995	20
NGC1841	5897	F555W	u2xj0708t	14/11/1995	800	F814W	u2xj0707t	14/11/1995	800
NGC1847	5475	F555W	u26m1b02p	10/04/1994	20	F450W	u26m1b01p	10/04/1994	40
NGC1850	5475	F555W	u26m1e02t	15/05/1994	20	F450W	u26m1e01t	15/05/1994	40
NGC1856	5475	F555W	u26m1302t	06/02/1994	30	F450W	u26m1301t	06/02/1994	60
NGC1860	5475	F555W	u26m1202t	07/02/1994	40	F450W	u26m1201t	07/02/1994	80
NGC1866	8134	F555W	u5ay0601r	21/08/1999	350	F814W	u5ay0604r	22/08/1999	350
NGC1868	5475	F555W	u26m0z02t	10/04/1994	100	F450W	u26m0z01t	10/04/1994	200
NGC1898	5916	F555W	u2xq0304t	10/12/1995	500	F814W	u2xq0309t	10/12/1995	600
NGC1916	5916	F555W	u2xq0403t	10/12/1995	500	F814W	u2xq0409t	10/12/1995	600
		F555W	u2xq0401t	10/12/1995	20	F814W	u2xq0406t	10/12/1995	20
NGC1984	8134	F555W	u5ay0901r	08/07/2000	350	F814W	u5ay0904r	09/07/2000	350
		F555W	u5ay0903r	09/07/2000	10	F814W	u5ay0906r	09/07/2000	10
NGC2004	5475	F555W	u26m1d02t	21/04/1994	20	F450W	u26m1d01t	21/04/1994	40
NGC2005	5916	F555W	u2xq0503t	19/10/1995	500	F814W	u2xq0509t	19/10/1995	600
		F555W	u2xq0501t	19/10/1995	20	F814W	u2xq0506t	19/10/1995	20
NGC2011	8134	F555W	u5ay0801r	19/08/1999	350	F814W	u5ay0804r	20/08/1999	350
		F555W	u5ay0803r	19/08/1999	10	F814W	u5ay0806r	20/08/1999	10
NGC2019	5916	F555W	u2xq0603t	18/10/1995	500	F814W	u2xq0609t	18/10/1995	600
		F555W	u2xq0601t	18/10/1995	20	F814W	u2xq0606t	18/10/1995	20
NGC2031	5904	F555W	u2y80301t	20/10/1995	300	F814W	u2y80304p	20/10/1995	300
NGC2100	5475	F555W	u26m1c02n	21/04/1994	20	F450W	u26m1c01t	21/04/1994	40
NGC2121	5475	F555W	u26m0x02t	02/02/1994	120	F450W	u26m0x01t	02/02/1994	230
NGC2136	5475	F555W	u26m1702t	11/02/1994	30	F450W	u26m1701t	11/02/1994	60
NGC2153 <sup>a</sup>	5475	F555W	u26m1502t	19/04/1994	30	F450W	u26m1501t	19/04/1994	60
NGC2155	5475	F555W	u26m0k02t	01/02/1994	120	F450W	u26m0k01t	01/02/1994	230
NGC2156	8134	F555W	u5ay0301r	22/08/1999	350	F814W	u5ay0304r	22/08/1999	350
		F555W	u5ay0303r	22/08/1999	10	F814W	u5ay0306r	22/08/1999	10
NGC2157	5475	F555W	u26m1902t	26/03/1994	30	F450W	u26m1901t	26/03/1994	60
NGC2159	8134	F555W	u5ay0401r	16/10/1999	350	F814W	u5ay0404r	16/10/1999	350
NGC2162	5475	F555W	u26m0t02t	23/08/1994	120	F450W	u26m0t01t	23/08/1994	230
NGC2164	8134	F555W	u5ay0101r	24/09/1999	350	F814W	u5ay0105r	24/09/1999	350
NGC2172	8134	F555W	u5ay0502r	14/10/1999	350	F814W	u5ay0504r	14/10/1999	350
NGC2173	5475	F555W	u26m0m02t	02/02/1994	120	F450W	u26m0m01t	02/02/1994	230
NGC2193	5475	F555W	u26m0p02t	30/01/1994	120	F450W	u26m0p01t	30/01/1994	230
NGC2209	5475	F555W	u26m0w02t	01/02/1994	120	F450W	u26m0w01t	01/02/1994	230
NGC2210	5897	F555W	u2xj0403t	13/12/1995	260	F814W	u2xj0401t	13/12/1995	260
NGC2213	5475	F555W	u26m0v02t	25/12/1994	120	F450W	u26m0v01t	25/12/1994	230
NGC2214	5475	F555W	u26m1802t	16/02/1994	30	F450W	u26m1801t	16/02/1994	60
NGC2231	5475	F555W	u26m0s02t	06/02/1994	120	F450W	u26m0s01t	06/02/1994	230
NGC2249	5475	F555W	u26m0y02t	11/08/1994	120	F450W	u26m0y01t	11/08/1994	230
NGC2257	5475	F555W	u26m0d02t	05/02/1994	300	F450W	u26m0d01t	05/02/1994	600
SL663 <sup>b</sup>	5475	F555W	u26m0l02t	01/02/1994	120	F450W	u26m0l01t	01/02/1994	230
SL842	5475	F555W	u26m0h02t	01/02/1994	120	F450W	u26m0h01t	01/02/1994	230
SL855	5475	F555W	u26m0q02t	01/02/1994	120	F450W	u26m0q01t	01/02/1994	230
HODGE4	5475	F555W	u26m0o02t	01/02/1994	120	F450W	u26m0o01t	01/02/1994	230
HODGE11	5475	F555W	u26m0f02t	01/02/1994	300	F450W	u26m0f01t	01/02/1994	600
HODGE14	5475	F555W	u26m0n02t	18/09/1994	120	F450W	u26m0n01t	18/09/1994	230
R136	5114	F555W	u2hk0304t	25/09/1994	23	F814W	u2hk030rt	25/09/1994	40
		F555W	u2hk0302t	25/09/1994	3	F814W	u2hk030qt	25/09/1994	5

### 2.2.2 Cluster ages

Age determinations for LMC clusters are widely scattered across the literature, and involve a large variety of techniques. The most useful homogeneous data set we have located is the colour-magnitude diagram (CMD) study and age calibration of Geisler et al. (1997), which provides age estimates for 15 clusters in our sample. Following this lead we have adopted where possible for the remaining clusters age determinations based on high resolution photometric studies resulting in CMDs. Pre-eminent amongst these are *HST* studies, and we adopt the results of Rich, Shara & Zurek (2001) for 5 intermediate age clusters and the results of Olsen et al. (1998) for 5 old clusters. We take the age determinations from the ground-based studies of E91 for 9 clusters and those of Dirsch et al. (2000) for a further three clusters. For NGC 1805 and NGC 1818 we adopt the ages from the thorough discussion and review of de Grijs et al. (2002b) and similarly for R136 we take the age as discussed by Sirianni et al. (2000). Finally, we fill the remaining holes in our sample with the age estimates of Elson & Fall (1988), who provide an age calibration based on a large sample of literature CMDs. We correct these estimates to a distance modulus of 18.5 using their prescribed method. We could not locate a reliable age for NGC 1916, but Olsen et al. (1998) do present a CMD for this cluster along with CMDs and age estimates for five old LMC clusters. The CMD for NGC 1916, though suffering from serious differential reddening, is not evidently different from those for the other five clusters, so we average the ages of these clusters to obtain an estimate for NGC 1916.

### 2.2.3 Cluster metallicities

The definitive study of LMC cluster metallicities is by Olszewski et al. (1991) who derive metallicities for  $\sim 70$  LMC clusters from observations of the calcium triplet in the spectra of giants. From this study we adopt metallicities for 23 of the clusters in our sample. We also adopt one metallicity (NGC 1841) from a subsequent paper in the same series (Suntzeff et al. 1992). A further three abundances (NGC 1850, NGC 2004, NGC 2100) are taken from the spectroscopic study of Jasniewicz and Thévenin (1994). The authors report standard deviations of  $\pm 0.03$  dex in the averages of several observations for each of these clusters; however we prefer their errors per single observation of  $\sim 0.2$  dex, which are more consistent with the other errors in Table 2. We adopt another two abundances from the infra-red spectra of Oliva & Origlia (1998), and one (NGC 1866) from the VLT spectroscopy of Hill et al. (2000). These complete the spectroscopic studies suitable for our data set. For a few clusters we therefore rely on abundances derived from CMD fits and corresponding to the ages discussed in Section 2.2.2. Four come from the study of Dirsch et al. (2000), and two from the *HST* photometry of Rich et al. (2001). For NGC 1805 and NGC 1818 we again take the ranges adopted by de Grijs et al. (2002b) after their detailed literature review (see also Johnson et al. (2001)), and similarly for R136 we again adopt the abundance from the discussion of Sirianni et al. (2000); see also Hunter et al. (1995). For the remaining 14 clusters we were not able to obtain suitable abundance measurements from the literature so for each of these we average the literature results for all the clusters in our sample of comparable age. We emphasize that these values in particular are simply rather crude estimates and that any use of them must account for this. In this paper, we adopt these abundances solely for the purpose of estimating mass to light ratios later in the analysis – calculations which in any case are rather insensitive to the adopted metallicity. Natu-

rally, any subsequent use must be carefully judged on the nature of the calculation at hand.

## 3 PHOTOMETRY

As part of the archive retrieval process, all frames were reduced according to the standard *HST* pipeline, using the latest available calibrations. This is preferable to using the original data as reduced soon after observation because the latest calibrations have a much longer baseline for calculation and are therefore more accurate. Bearing in mind that our data set covers a span of more than five years of *HST* observations, we also maintain the homogeneity of our reduction process by using calibrations from a single epoch.

For photometric measurements we have found Dolphin's HSTphot (Dolphin 2000a) to be the most suitable software package. Our large number of observations requires the reduction process to be run automatically where possible, without sacrificing data integrity. HSTphot is well suited for running in batch mode and is specifically tailored to the reduction of WFPC2 frames, routinely accounting for the severely under-sampled PC/WFC point spread functions (PSFs) and their variation due to sub-pixel positioning. In particular, the *multi*phot routine has proven to be the most useful for our data set. This program first aligns accurately (to fractions of a WFC pixel) and then performs simultaneous photometry on multiple images of the same field, regardless of the filter combination. This makes it perfect for the current data set – with two frames per field, each through a different filter. Conventionally, this would make the removal of cosmic rays and cross identification of objects complicated and unreliable. By solving the two frames simultaneously, both these problems are accounted for.

Before starting *multi*phot each frame is readied with the image preparation utilities included with the HSTphot package. This procedure includes the masking of bad data<sup>‡</sup> as flagged by the STScI data quality image which accompanies each observation, a first attempt at the removal of cosmic rays (using a routine based on the IRAF task CRREJ), the removal of hot-pixels not flagged by the data quality image (using a  $\sigma$ -clipping algorithm), and the robust determination of a background image – used by *multi*phot for stellar detection and measurement.

Photometric measurements are made using *multi*phot in PSF fitting mode. While aperture photometry mode is also an option, we have found that PSF fitting produces main sequences on our CMDs that are at least as narrow as those from aperture photometry using 2 WFC pixel and 3 PC pixel radii. This is presumably because *multi*phot is designed specifically for measurements involving the unique WFPC2 PSFs. The detection algorithm used by *multi*phot is similar in principle to that of DoPHOT, being based around the recursive location and subtraction of objects at increasingly lower threshold levels. We set a minimum threshold level for detection of  $3\sigma$  above the background. In addition, we enable a feature of *multi*phot which calculates an adjustment to the background image before each photometry measurement using the pixels just beyond the photometry radius (Dolphin 2000a). This is designed to account for rapidly varying backgrounds such as those expected in observations of the crowded central regions of globular clusters.

The object classification, sharpness and  $\chi$  parameters produced from *multi*phot's PSF fitting are used to keep the photom-

<sup>‡</sup> Such as known bad pixels, saturated pixels, charge traps, bad columns, and the vignetted region between chips

**Table 2.** Literature nomenclature, position, age and metallicity data for the cluster sample.

Principal Name	Alternative Names	Position (J2000.0)				$\log \tau$ (yr)	Age Ref.	Metallicity [Fe/H]	Met. Ref.
		$\alpha$	$\delta$	$R_{opt} (^{\circ})^a$	$R_{rot} (^{\circ})^b$				
NGC1466	SL1, LW1	03 <sup>h</sup> 44 <sup>m</sup> 33 <sup>s</sup>	-71°40'18''	7.89	8.38	10.10 ± 0.01	5	-2.17 ± 0.20	12
NGC1651	SL7, LW12	04 <sup>h</sup> 37 <sup>m</sup> 32 <sup>s</sup>	-70°35'06''	3.77	4.29	9.30 <sup>+0.08</sup> <sub>-0.10</sub>	5	-0.37 ± 0.20	12
NGC1711	SL55	04 <sup>h</sup> 50 <sup>m</sup> 37 <sup>s</sup>	-69°59'06''	2.64	3.17	7.70 ± 0.05	2	-0.57 ± 0.17	2
NGC1718	SL65	04 <sup>h</sup> 52 <sup>m</sup> 25 <sup>s</sup>	-67°03'06''	3.69	4.00	9.30 ± 0.30	4	-0.42	*
NGC1754	SL91	04 <sup>h</sup> 54 <sup>m</sup> 17 <sup>s</sup>	-70°26'30''	2.43	2.96	10.19 <sup>+0.06</sup> <sub>-0.07</sub>	11	-1.54 ± 0.20	12
NGC1777	SL121, LW96	04 <sup>h</sup> 55 <sup>m</sup> 48 <sup>s</sup>	-74°17'00''	5.10	5.44	9.08 <sup>+0.12</sup> <sub>-0.18</sub>	5	-0.35 ± 0.20	12
NGC1786	SL149	04 <sup>h</sup> 59 <sup>m</sup> 06 <sup>s</sup>	-67°44'42''	2.70	3.02	10.18 ± 0.01	5	-1.87 ± 0.20	12
NGC1805	SL186	05 <sup>h</sup> 02 <sup>m</sup> 21 <sup>s</sup>	-66°06'42''	3.86	4.00	7.00 <sup>+0.30</sup> <sub>-0.10</sub>	1	0.00 to -0.40	1,9
NGC1818	SL201	05 <sup>h</sup> 04 <sup>m</sup> 14 <sup>s</sup>	-66°26'06''	3.47	3.61	7.40 <sup>+0.30</sup> <sub>-0.10</sub>	1	0.00 to -0.40	1,9
NGC1831	SL227, LW133	05 <sup>h</sup> 06 <sup>m</sup> 16 <sup>s</sup>	-64°55'06''	4.82	4.85	8.50 ± 0.30	4	+0.01 ± 0.20	12
NGC1835	SL215	05 <sup>h</sup> 05 <sup>m</sup> 05 <sup>s</sup>	-69°24'12''	1.40	1.90	10.22 <sup>+0.07</sup> <sub>-0.08</sub>	11	-1.79 ± 0.20	12
NGC1841		04 <sup>h</sup> 45 <sup>m</sup> 23 <sup>s</sup>	-83°59'48''	14.55	14.78	10.09 ± 0.01	5	-2.11 ± 0.10	15
NGC1847	SL240	05 <sup>h</sup> 07 <sup>m</sup> 08 <sup>s</sup>	-68°58'18''	1.34	1.77	7.42 ± 0.30	4	-0.37	*
NGC1850	SL261	05 <sup>h</sup> 08 <sup>m</sup> 44 <sup>s</sup>	-68°45'36''	1.32	1.70	7.50 ± 0.20	3	-0.12 ± 0.20	8
NGC1856	SL271	05 <sup>h</sup> 09 <sup>m</sup> 29 <sup>s</sup>	-69°07'36''	1.08	1.53	8.12 ± 0.30	4	-0.52	*
NGC1860	SL284	05 <sup>h</sup> 10 <sup>m</sup> 39 <sup>s</sup>	-68°45'12''	1.18	1.54	8.28 ± 0.30	4	-0.52	*
NGC1866	SL319, LW163	05 <sup>h</sup> 13 <sup>m</sup> 39 <sup>s</sup>	-65°27'54''	4.08	4.03	8.12 ± 0.30	4	-0.50 ± 0.10	6
NGC1868	SL330, LW169	05 <sup>h</sup> 14 <sup>m</sup> 36 <sup>s</sup>	-63°57'18''	5.57	5.47	8.74 ± 0.30	4	-0.50 ± 0.20	12
NGC1898	SL350	05 <sup>h</sup> 16 <sup>m</sup> 42 <sup>s</sup>	-69°39'24''	0.41	0.95	10.15 <sup>+0.06</sup> <sub>-0.08</sub>	11	-1.37 ± 0.20	12
NGC1916	SL361	05 <sup>h</sup> 18 <sup>m</sup> 39 <sup>s</sup>	-69°24'24''	0.21	0.72	10.20 ± 0.09	*	-2.08 ± 0.20	12
NGC1984	SL488	05 <sup>h</sup> 27 <sup>m</sup> 40 <sup>s</sup>	-69°08'06''	0.69	0.15	7.06 ± 0.30	4	-0.90 ± 0.40	10
NGC2004	SL523	05 <sup>h</sup> 30 <sup>m</sup> 40 <sup>s</sup>	-67°17'12''	2.38	2.01	7.30 ± 0.20	3	-0.56 ± 0.20	8
NGC2005	SL518	05 <sup>h</sup> 30 <sup>m</sup> 09 <sup>s</sup>	-69°45'06''	0.84	0.58	10.22 <sup>+0.12</sup> <sub>-0.16</sub>	11	-1.92 ± 0.20	12
NGC2011	SL559	05 <sup>h</sup> 32 <sup>m</sup> 19 <sup>s</sup>	-67°31'18''	2.24	1.82	6.99 ± 0.30	4	-0.47 ± 0.40	10
NGC2019	SL554	05 <sup>h</sup> 31 <sup>m</sup> 56 <sup>s</sup>	-70°09'36''	1.16	1.01	10.25 <sup>+0.07</sup> <sub>-0.09</sub>	11	-1.81 ± 0.20	12
NGC2031	SL577	05 <sup>h</sup> 33 <sup>m</sup> 41 <sup>s</sup>	-70°59'12''	1.83	1.82	8.20 ± 0.10	2	-0.52 ± 0.21	2
NGC2100	SL662	05 <sup>h</sup> 42 <sup>m</sup> 08 <sup>s</sup>	-69°24'42''	1.90	1.37	7.20 ± 0.20	3	-0.32 ± 0.20	8
NGC2121	SL725, LW303	05 <sup>h</sup> 48 <sup>m</sup> 12 <sup>s</sup>	-71°28'48''	2.95	2.80	9.51 <sup>+0.06</sup> <sub>-0.07</sub>	13	-0.61 ± 0.20	12
NGC2136	SL762	05 <sup>h</sup> 53 <sup>m</sup> 17 <sup>s</sup>	-69°31'42''	2.83	2.34	8.00 ± 0.10	2	-0.55 ± 0.23	2
NGC2153	SL792, LW341	05 <sup>h</sup> 57 <sup>m</sup> 51 <sup>s</sup>	-66°24'00''	4.81	4.23	9.11 <sup>+0.12</sup> <sub>-0.16</sub>	5	-0.42	*
NGC2155	SL803, LW347	05 <sup>h</sup> 58 <sup>m</sup> 33 <sup>s</sup>	-65°28'36''	5.59	5.03	9.51 <sup>+0.06</sup> <sub>-0.07</sub>	13	-0.55 ± 0.20	12
NGC2156	SL796	05 <sup>h</sup> 57 <sup>m</sup> 45 <sup>s</sup>	-68°27'36''	3.53	2.96	7.60 ± 0.20	3	-0.45	*
NGC2157	SL794	05 <sup>h</sup> 57 <sup>m</sup> 34 <sup>s</sup>	-69°11'48''	3.26	2.75	7.60 ± 0.20	3	-0.45	*
NGC2159	SL799	05 <sup>h</sup> 57 <sup>m</sup> 57 <sup>s</sup>	-68°37'24''	3.48	2.92	7.60 ± 0.20	3	-0.45	*
NGC2162	SL814, LW351	06 <sup>h</sup> 00 <sup>m</sup> 31 <sup>s</sup>	-63°43'18''	7.23	6.69	9.11 <sup>+0.12</sup> <sub>-0.16</sub>	5	-0.23 ± 0.20	12
NGC2164	SL808	05 <sup>h</sup> 58 <sup>m</sup> 54 <sup>s</sup>	-68°31'06''	3.61	3.04	7.70 ± 0.20	3	-0.45	*
NGC2172	SL812	06 <sup>h</sup> 00 <sup>m</sup> 05 <sup>s</sup>	-68°38'12''	3.66	3.11	7.60 ± 0.20	3	-0.44	*
NGC2173	SL807, LW348	05 <sup>h</sup> 57 <sup>m</sup> 58 <sup>s</sup>	-72°58'42''	4.43	4.37	9.33 <sup>+0.07</sup> <sub>-0.09</sub>	5	-0.24 ± 0.20	12
NGC2193	SL839, LW387	06 <sup>h</sup> 06 <sup>m</sup> 17 <sup>s</sup>	-65°05'54''	6.48	5.89	9.34 <sup>+0.09</sup> <sub>-0.11</sub>	13	-0.60 ± 0.20	13
NGC2209	SL849, LW408	06 <sup>h</sup> 08 <sup>m</sup> 34 <sup>s</sup>	-73°50'30''	5.48	5.43	8.98 <sup>+0.15</sup> <sub>-0.24</sub>	5	-0.47	*
NGC2210	SL858, LW423	06 <sup>h</sup> 11 <sup>m</sup> 31 <sup>s</sup>	-69°07'18''	4.52	4.00	10.20 ± 0.01	5	-1.97 ± 0.20	12
NGC2213	SL857, LW419	06 <sup>h</sup> 10 <sup>m</sup> 42 <sup>s</sup>	-71°31'42''	4.44	4.16	9.20 <sup>+0.10</sup> <sub>-0.12</sub>	5	-0.01 ± 0.20	12
NGC2214	SL860, LW426	06 <sup>h</sup> 12 <sup>m</sup> 57 <sup>s</sup>	-68°15'36''	4.97	4.40	7.60 ± 0.20	3	-0.45	*
NGC2231	SL884, LW466	06 <sup>h</sup> 20 <sup>m</sup> 44 <sup>s</sup>	-67°31'06''	6.04	5.46	9.18 <sup>+0.10</sup> <sub>-0.13</sub>	5	-0.67 ± 0.20	12
NGC2249	SL893, LW479	06 <sup>h</sup> 25 <sup>m</sup> 49 <sup>s</sup>	-68°55'12''	5.86	5.33	8.82 ± 0.30	4	-0.47	*
NGC2257	SL895, LW481	06 <sup>h</sup> 30 <sup>m</sup> 12 <sup>s</sup>	-64°19'36''	9.10	8.47	10.20 ± 0.10	2	-1.63 ± 0.21	2
SL663	LW273	05 <sup>h</sup> 42 <sup>m</sup> 29 <sup>s</sup>	-65°21'48''	4.69	4.23	9.51 <sup>+0.06</sup> <sub>-0.07</sub>	13	-0.60 ± 0.20	13
SL842	LW399	06 <sup>h</sup> 08 <sup>m</sup> 15 <sup>s</sup>	-62°59'18''	8.43	7.85	9.30 <sup>+0.08</sup> <sub>-0.10</sub>	5	-0.36 ± 0.20	12
SL855	LW420	06 <sup>h</sup> 10 <sup>m</sup> 53 <sup>s</sup>	-65°02'36''	6.88	6.29	9.13 ± 0.30	4	-0.42	*
HODGE4	SL556, LW237	05 <sup>h</sup> 31 <sup>m</sup> 54 <sup>s</sup>	-64°42'00''	4.92	4.59	9.34 <sup>+0.09</sup> <sub>-0.11</sub>	13	-0.15 ± 0.20	12
HODGE11	SL868, LW437	06 <sup>h</sup> 14 <sup>m</sup> 22 <sup>s</sup>	-69°50'54''	4.62	4.15	10.18 ± 0.01	5	-2.06 ± 0.20	12
HODGE14	SL506, LW220	05 <sup>h</sup> 28 <sup>m</sup> 39 <sup>s</sup>	-73°37'48''	4.19	4.37	9.26 <sup>+0.09</sup> <sub>-0.11</sub>	5	-0.66 ± 0.20	12
R136	NGC2070, 30Dor	05 <sup>h</sup> 38 <sup>m</sup> 43 <sup>s</sup>	-69°06'03''	1.63	1.09	6.48 <sup>+0.12</sup> <sub>-0.18</sub>	14	~ -0.4	7,14

Reference list: 1. de Grijs et al. (2002b); 2. Dirsch et al. (2000); 3. Elson (1991); 4. Elson & Fall (1988); 5. Geisler et al. (1997); 6. Hill et al. (2000); 7. Hunter et al. (1995); 8. Jasniewicz & Thévenin (1994); 9. Johnson et al. (2001); 10. Oliva & Origlia (1998); 11. Olsen et al. (1998); 12. Olszewski et al. (1991); 13. Rich et al. (2001); 14. Sirianni et al. (2000); 15. Suntzeff et al. (1992).

\* Calculated metallicity (or age for NGC 1916), as described in the text.

<sup>a</sup> Relative to the optical centre of the LMC bar, at  $\alpha = 05^{\text{h}}20^{\text{m}}56^{\text{s}}$ ,  $\delta = -69^{\circ}28'41''$  (J2000.0) (Bica et al. 1996).

<sup>b</sup> Relative to the H I rotation centre of the LMC, at  $\alpha = 05^{\text{h}}26^{\text{m}}39^{\text{s}}$ ,  $\delta = -69^{\circ}15'36''$  (J2000.0) (Rohlf et al. 1984; Westerlund 1990)

entry clean of non-stellar objects and spurious detections. The object classification parameter is a determination as to which prototype PSF the measured profile of an object conforms to – the options being stellar (or a marginally resolved stellar pair), extended (galaxy), or single pixel (cosmic ray). The sharpness value for an object is a measure of how sharp its profile is in comparison with the stellar PSF, being negative if the profile is too broad, zero if the object is a perfect fit and positive if the profile is too sharp. Finally, the  $\chi$  value simply measures the quality of fit of the PSF to the object profile. After some experimentation, we found that selecting objects with sharpness between  $-0.6$  and  $+0.6$  and  $\chi \leq 3.5$  provided a mostly complete stellar sample for the purpose of constructing surface brightness profiles. For the construction of clean CMDs, these values would be somewhat stricter.

The final photometric measurements obtained from *multiplot* are from PSFs corrected for geometric distortion (Holtzman et al. 1995a), the filter-dependent plate scale changes (determined empirically) (Dolphin 2000a), and the 34th row error (Shaklan, Sharman & Pravdo 1995; Anderson & King 1999). The magnitudes are also corrected for charge-transfer efficiency (CTE) effects using the longest baseline calibration available – that of Dolphin (2000b). Notably, this calibration also provides corrections for “warm” data – that is, observations taken before the WFPC2 cool-down of 1994 April 23. This is especially important for our data set, since 25 clusters were observed in warm conditions. The stellar magnitudes are also corrected for PSF residuals and to an aperture of  $0''.5$  using groups of isolated stars selected according to a set of strict criteria (Dolphin 2000a). Finally, *multiplot* uses the zero-points from the Dolphin (2000b) calibration. We do not convert from the *HST* instrumental system to the Johnson-Cousins system because this transformation is not important for the construction of surface brightness profiles, instead adding unnecessary scatter to the photometry. Dolphin (2000a) estimates the limiting photometric and astrometric accuracy of *multiplot* to be 0.011 to 0.014 mag and 0.05 pixels ( $2.5 \times 10^{-3}$  arcsec on the PC and  $5.4 \times 10^{-3}$  arcsec on the WFCs) respectively.

## 4 SURFACE BRIGHTNESS PROFILES

Constructing a surface brightness profile for a given cluster is simple in concept; however in practice, our calculations were complicated by the high resolution and peculiar chip geometry of WFPC2. The procedure is similar to that for ground-based data however, and we broadly follow the techniques outlined by Djorgovski (1987).

### 4.1 Astrometry and centre determination

One problem presented by the data was due to the four chip structure of WFPC2. In order to maintain the accurate relative spatial positioning of stars from chip to chip, we overlaid a uniform coordinate system, accounting for the geometric distortion from *HST*'s optical system, the changes in pixel scale from the PC to WFCs and the separations between the chips. This was achieved using the IRAF STSDAS task METRIC, which converts the chip and pixel coordinates for a list of stars to pixel coordinates relative to the WFPC2 chip, making the appropriate geometric corrections, and then converts these corrected pixel coordinates to  $(\alpha, \delta)$  (J2000.0) using the positional information in the image headers. This header information is not always reliable, and can introduce errors into the  $(\alpha, \delta)$  so calculated. To avoid this, we took the corrected pixel coordinates from METRIC for each star and derived angular separa-

tions using the WFC pixel scale of  $0.0996$  arcsec pixel $^{-1}$ , rather than taking the  $(\alpha, \delta)$  for each star and calculating angular separations from these. All centering calculations, annulus construction, and completeness and area corrections (see below) used these corrected pixel coordinates. The only results which incorporate image header positional information are the calculated centre coordinates expressed in  $(\alpha, \delta)$  (see Table 4).

The next task was to locate accurately the centre of any given cluster<sup>§</sup>. Poor centering will tend to artificially flatten a surface brightness profile, and this in turn can lead to large systematic errors in any structural parameters derived from the profile, and may obscure important dynamical information such as the presence of a post-collapse core. There are several algorithms for locating a cluster's centre which rely on the symmetry properties of the cluster, one example being the mirror-autocorrelation method described by Djorgovski (1987). However, such algorithms were not completely suitable for our data. Unlike Galactic globular clusters, many Magellanic Cloud clusters do not have smooth profiles, but instead are clumpy, irregular and not particularly symmetric, making it difficult to apply symmetry-algorithms robustly and uniformly across the sample. In addition, and compounded by the high resolution and small field of view of WFPC2, several clusters have very low surface brightness, adding to the problem. The high resolution in particular means that it is not sufficient to simply apply spatial smoothing to most clusters, because the magnitude of the smoothing required degrades the intrinsic accuracy of the centre determination, and the process therefore loses its value.

Instead, we employed a Monte Carlo style method to locate our cluster centres. In this procedure, each chip is first split into boxes of equal area ( $\sim 100$  WFC pixels on a side). For each box, the surface brightness is calculated by adding up the fluxes for all stars in the box (including completeness corrections – see Section 4.2.2) and dividing by the area of the box. The search is then narrowed to the region covered by the box with the highest surface brightness, and the eight boxes surrounding it. It does not matter if this region falls across more than one CCD – we simply account for the vignetted area (where no stars are detected) in the subsequent calculations. If the box with the highest surface brightness falls right on the edge of a CCD, where it is not joined by another CCD, then the number of surrounding boxes is less (five if the central box is on an edge; three if it lies in a corner) and the amalgamated region is correspondingly smaller. Within this amalgamated region, points are randomly generated and the surface brightness calculated (as for the boxes) in a circle of radius  $r$  about each point. If part of one of these circles falls off the edge of a chip or over a vignetted region, this “lost area” is accounted for in the calculation. After  $N$  tries, the point corresponding to the circle with the highest surface brightness is taken to be the cluster centre.

This routine has the disadvantage that it is very good at finding the brightest star in a cluster, and although this does represent a surface brightness peak, it generally does not correspond to the overall cluster surface brightness peak. To avoid this, we would ideally like to exclude the few brightest stars in a cluster from the above calculations, and instead use a sub-sample which should closely trace the cluster's surface brightness profile (i.e., a sample which has its greatest density coincident with the cluster's surface brightness peak). Main sequence stars are such an ensemble, and so for each cluster we impose colour and magnitude limits on the cluster CMD to select only these stars for the centre determination. In gen-

<sup>§</sup> Or more correctly, the central surface brightness peak.

eral this procedure worked well; however for clusters with severe central crowding, it was necessary to relax the limits and include brighter stars from the giant branch (or upper main sequence in the case of very young clusters).

While inelegant and computationally expensive, our random sampling method is robust and easily adapted for clusters of different concentration and richness simply by variation of  $r$  and  $N$ . As a consistency check, we run the centering algorithm independently on both colour frames for a field. For  $N = 2000$  the centering is repeatable to a limiting accuracy of approximately  $\pm 10$  WFC pixels – approximately  $\pm 1''$ . As noted above however, the conversion from pixel coordinates to  $(\alpha, \delta)$  may introduce large errors if the image header information is inaccurate. A comparison of our calculated centres (Table 4) with those in Table 2 shows good agreement, meaning that we have not introduced any large errors. We note however that this comparison is not sensitive to small (several arcsecond) errors. Notwithstanding this, we expect that our calculated centres are at least as accurate as the literature values.

## 4.2 Annulus construction and flux corrections

For each frame (two per cluster), four sets of circular annuli were constructed about the cluster centre. Two sets had narrow annulus widths of  $1''.5$  and  $2''$  respectively and were designed for sampling the central regions of a cluster. To this end, the  $1''.5$  annuli were calculated to a radius of  $\sim 20''$  and the  $2''$  annuli to  $\sim 30''$ . The two other annulus sets had larger widths of  $3''$  and  $4''$  respectively, and were used primarily for sampling the outer (less dense) regions of a cluster. These two profiles were therefore extended to the maximum radii possible. Although many LMC clusters have slightly elliptical isophotes at extended radii, there is little evidence to suggest that the mass distribution in inner regions is in general not spherical (cf. E91) – hence we fit circular annuli. In addition, because of the small WFPC2 field of view, none of the images in the data set fully cover any cluster, making the use of elliptical annuli impractical.

Because of the high resolution of our images we simply counted stars to calculate the surface brightness for an annulus. For each set, the surface brightness  $\mu_i$  of the  $i$ -th annulus is given by:

$$\mu_i = \frac{A_i}{\pi(b_i^2 - a_i^2)} \sum_{j=1}^{N_s} C_j F_j \quad (1)$$

where  $b_i$  and  $a_i$  are the outer and inner radii of the annulus respectively,  $N_s$  is the number of stars in the annulus, and  $F_j$  is the flux of the  $j$ -th star. The factors  $A_i$  and  $C_j$  are the area correction for an annulus and the completeness correction for a star respectively, and must be determined before the annulus is constructed. We outline the meaning of these factors and their methods of calculation individually below.

### 4.2.1 Area corrections

The area correction  $A_i$  for the  $i$ -th annulus is used simply to normalize the flux in the annulus to that for a full annulus. This is necessary because the shape of WFPC2 means that for all clusters, most annuli are not completely covered by the field of view. Since the flux through an annulus is directly related to the annulus area, variations in the fractions of annuli covered cause artificial fluctuations in a surface brightness profile, and must therefore be accounted for.

The process of determining the area correction for an annulus is complicated by the WFPC2 chip geometry (including the small

separations between the CCDs), the centering of the cluster on the camera and the roll angle of *HST* at the time of observation. The arbitrary nature of the second two factors from cluster to cluster once again led us to resort to an inelegant but robust Monte Carlo scheme. For a given cluster we determine corrected pixel coordinates for the sixteen CCD corner pixels which define the WFPC2 field of view, and from these we derive the border equations of the four CCDs. A large number of points are then randomly generated over the full area of each annulus, and using the CCD boundary equations we determine which points fall on the WFPC2 camera, and which do not. The area correction  $A_i$  for the  $i$ -th annulus is the total number of points generated divided by the number “imaged”. Again, while computationally inefficient, this method is very robust and can easily account for the arbitrary geometry of any particular observation, with an accuracy limited only by the number of random points. A small amount of experimentation showed ten thousand points per annulus to be sufficient. To avoid introducing large uncertainties into the data we do not use annuli for which the fraction covered falls below a third. This limits the maximum radius for a surface brightness profile to be  $\sim 75 - 80''$ .

An example of the process is shown in Fig. 1 – a pointing for NGC 1841. Annuli of width  $4''$  have been drawn about the centre to  $100''$ , and for every second annulus the random points falling in the field of view have been plotted. The accuracy with which the process handles the complicated geometry is quite evident – note particularly the small separations of the chips due to the vignetted regions masked by HSTphot, and the significant errors these can cause to an annulus of the right radius which falls tangent. At  $100''$  the area correction factor is approximately 4, and in practice the process was halted at  $r = 78''$ .

### 4.2.2 Completeness corrections

Even with *HST* resolution, crowding and saturation can cause significant numbers of stars to be missed by automated detection software such as HSTphot. This missing flux can seriously affect a cluster’s surface brightness profile and must be accounted for. To quantify the correction we used the artificial star routine attached to *multiphot*. For each cluster, we set this routine to generate  $\sim 3.5 \times 10^5$  stars per CCD (i.e.,  $\sim 1.4 \times 10^6$  stars per cluster) on a CMD, the limits of which are set to be two magnitudes above the saturation limit and two magnitudes below the faint limit for an image, and 0.5 magnitudes redder than the reddest region of the cluster’s CMD and 0.5 magnitudes bluer than the bluest region. The stars are spatially distributed according to the flux of the image. Each star is placed on the image and solved (one at a time) by *multiphot*, using the same settings as for the real data. Stars are flagged if they are not recovered. The output photometry file is exactly similar to the *multiphot* output for real stars, and we run this artificial photometry through our classification, sharpness and  $\chi$  selection criteria, again flagging stars which are removed from the sample.

To determine the completeness function for a given chip, the fake stars are binned according to their  $x$ - and  $y$ -position on the chip, magnitude and colour. Bin sizes are typically 160 pixels in  $x$  and  $y$  in uncrowded regions (independent of chip), 0.2 magnitudes in brightness and 0.25 magnitudes in colour. A large majority of our sample suffers little or no crowding, even in the central regions of a cluster. This means that the binning resolution described above, particularly in the positional sense, is perfectly adequate to account for the gradual spatial variations in completeness. This is demonstrated below, in the example for NGC 2213, which is a typical cluster in the sample. For severely crowded regions however,

the completeness may suffer rapid and significant spatial variation, and in these cases the resolution of the positional binning was increased to account for this. In the very worst cases, the inclusion of short exposures (see Section 4.2.3 below) usually significantly alleviated any crowding problems.

The completeness  $c$  for a given bin is the number of successfully recovered (unflagged) stars divided by the total number of stars generated in that bin, and the completeness correction  $C_j$  for the  $j$ -th star in an annulus the inverse of  $c$  for the appropriate bin. To avoid large uncertainties, we eliminated any stars with completeness less than  $c_l = 0.25$ . Experimentation showed that variation of this limit (i.e.,  $0.05 \leq c_l \leq 0.5$ ) had a negligible effect on most profiles, reflecting the fact that incompleteness was not an issue for the large majority of clusters.

Examples of the completeness functions for two clusters (the relatively open cluster NGC 2213 and the extremely compact cluster NGC 2005) are shown in Fig. 2 together with the PC F555W images of the centres of these clusters. For ease of visualization the completeness functions have been integrated over position and colour to be functions of brightness only. For NGC 2213, crowding and saturation are not significant, and the completeness functions reflect this. The core of the cluster is imaged on the PC chip (solid line), and the completeness function for this chip matches well the completeness functions for the three WFC chips, which imaged the outer regions of the cluster. If incompleteness (or rapid spatial variation of completeness) was a significant issue in the central regions, then the position averaged PC function would be significantly degraded in comparison to the three WFC functions. The second cluster in Fig. 2, NGC 2005, is an example of this. The effect of this cluster's extremely compact core on the PC completeness function is clear, and it is evident that a positional resolution of 160 pixels is not adequate to fully describe the completeness variations. In fact, in the very central regions, the situation is even worse than this – the completeness is so low that the measurements become meaningless. To demonstrate this, from the three WFC functions, we expect the non-crowded regions of the PC to have  $c \sim 0.85$  at  $V_{555} \sim 24$ , whereas we measure a spatially averaged value of  $c \sim 0.45$ . From the PC image, approximately half of the chip may be non-crowded, implying that the integrated completeness in the crowded region must be  $c \lesssim 0.05$  at  $V_{555} \sim 24$  (cf. Fig. 3(b)). In a case such as this, we had to use additional information from a short exposure (see Section 4.2.3, below), otherwise the surface brightness profile became useless.

We note that none of the completeness functions plotted in Fig. 2 ever reaches  $c = 1$  – this is due to the integration over colour and position, since bad pixels and bright stars prevent *all* fake stars being recovered. Certainly however, individual bins in position-brightness-colour space can (and do) have full completeness. Completeness functions can also tell us a small amount about the background field near a cluster. The degradation evident in the WFC completeness functions for NGC 2005 is primarily due to the dense field population in the region of this cluster (NGC 2005 lies very near the LMC bar). By comparison, the field population near NGC 2213 is quite sparse.

#### 4.2.3 Short exposures

As discussed in Section 4.2.2, in nine cases where severe crowding and/or saturation significantly degraded the completeness in parts of an image, we used information from short exposure images to complete the surface brightness profiles. This occurred specifically for the very old, compact clusters NGC 1754, NGC 1835, NGC

1916, NGC 2005, and NGC 2019, and the very young clusters NGC 1984, NGC 2011, NGC 2156, and R136. NGC 1786 required correction but no additional data was available.

To add the short exposure data is a relatively straightforward process. For a given cluster, the short exposure image is reduced in exactly the same manner as the original image, and a surface brightness profile constructed. When plotted over the original surface brightness profile, the short exposure profile is found to have a shape matching that of the original at large radii (where neither crowding nor saturation are an issue), but with a larger scatter and brighter by some tenths of a magnitude. This offset is a product of the shorter image having a brighter saturation limit and therefore including more bright stars in its profile than the longer image, whereas the larger scatter is due to both the inclusion of many of the brightest stars in the cluster (see also Section 4.2.4) and the exclusion of large numbers of faint stars, which do not get measured on the short image. To eliminate the offset, we impose a brightness limit  $V_{lim}$  on the short exposure photometry to cut out the brightest stars, and vary  $V_{lim}$  until the profiles overlap in their outer regions. This is equivalent to removing the brightest stars in the cluster from the calculations, as discussed below in Section 4.2.4, and so also reduces the noise in the short exposure profile. It is then simple to measure the radius  $r_{dev}$  at which incompleteness becomes an issue and the two profiles begin to deviate, and form a composite profile using photometry for stars with  $r \leq r_{dev}$  from the short exposure (with  $V_{lim}$  imposed) and the remainder (with  $r > r_{dev}$ ) from the long exposure. This keeps scatter to a minimum while alleviating the incompleteness at small radii.

Fig. 3 shows an example of this process for NGC 2005. In the previous Section (4.2.2) we showed that the long exposure photometry for this cluster suffered serious incompleteness in the central region. Further evidence of this can be seen in Fig. 3(a). The two surface brightness profiles show a similar shape up to  $\log r_{dev} \sim 0.8$ , or  $r_{dev} \sim 6''.3$ . At this point incompleteness in the long exposure photometry becomes significant and the surface brightness profile eventually turns over because of the amount of missing flux. Not only is the completeness very low in this region, but it must vary on a scale shorter than  $\sim 6''$ , or  $\sim 130$  pixels. To account for the crowding, measurements are taken from the short photometry within  $6''.3$ . The advantage gained from this is evident in Fig. 3(b), which shows the completeness functions for the long and short exposure photometry, for  $r < r_{dev}$ . As before, the completeness functions have been integrated over position and colour to be a function of brightness only. The terrible incompleteness in the long exposure photometry is very evident. It is also clear that the short exposure photometry within the central region accounts very well for this incompleteness, and we are therefore justified in using only the short exposure photometry for the surface brightness profile in this region.

#### 4.2.4 Saturated stars

At this stage we comment briefly on the treatment of saturated stars in our images. Such stars were not measured by *multiphot* and were therefore not included in the construction of surface brightness profiles. For most clusters, saturated stars are not a significant factor. Of the 53 clusters in the sample, thirty had less than five saturated stars within approximately two core radii of the centre. When data from short exposures were included to circumvent extreme crowding and saturation (see Section 4.2.3), this number rose to 39. For all of these clusters, the presence of so few saturated stars meant that their neglect did not significantly alter the surface brightness



**Table 3.** Clusters with more than five saturated stars within two core radii.

Cluster	$\log \tau$ (yr)	$N_s^a$	$f_s^b$
NGC1466	10.10	15	0.002
NGC1711	7.70	45	0.018
NGC1786	10.18	$\sim 20^c$	$\sim 0.008$
NGC1805	7.00	30	0.034
NGC1818	7.40	35	0.016
NGC1841	10.09	$\sim 50^d$	0.003
NGC1866	8.12	30	0.009
NGC1898	10.15	35	0.006
NGC2031	8.20	35	0.012
NGC2159	7.60	25	0.022
NGC2164	7.70	30	0.016
NGC2172	7.60	30	0.033
NGC2210	10.20	30	0.005
NGC2257	10.20	10	0.001

<sup>a</sup> Approximate number of saturated stars within two core radii.

<sup>b</sup>  $N_s$  divided by the total number of stars within two core radii.

<sup>c</sup> This figure is an estimate since NGC 1786 suffers from extreme crowding and no short exposure was available.

<sup>d</sup> NGC 1841 has an extremely large core radius.

profiles derived for these clusters, especially given that on average several thousand stars were measured in the central regions of each.

The remaining fourteen clusters are listed in Table 3, along with an estimate of the total number of saturated stars within two core radii for each cluster. We felt comfortable leaving these stars out of the calculations, for the following reasons. Firstly, their presence did not degrade the quality of the images or the measurements made from these images (otherwise short exposure data would have been obtained – see Section 4.2.3). Secondly, it is clear that for each cluster, the fraction listed in Table 3 is tiny (although larger than for the other 39 clusters). The fourteen clusters in Table 3 are either young ( $\tau \lesssim 100$  Myr) or very old ( $\tau > 10$  Gyr). In such clusters, the brightest stars are either giants or upper main-sequence stars and are in very brief (but very luminous) phases of evolution, especially compared to the dynamical timescales (e.g., the median relaxation time) of the clusters they are in. They therefore may not in general represent the spatial distribution of the underlying stellar population. It does not make sense to measure a surface brightness profile which is dominated by the output of an essentially randomly distributed tiny fraction of the stars in a cluster – in practice, this simply adds large amounts of noise to the profile.

Removing these stars from the calculations provides less noisy profiles without compromising the measurement of structural parameters. Elson and collaborators for example (Elson et al. (1989); E91; Elson (1992)) routinely remove the brightest stars when calculating their surface brightness profiles, in order to make sure the profile reflects the underlying stellar distribution. Specifically, Elson et al. (1989) found that the removal of these stars (in the construction of their “cleaned” profiles) reduced the scatter in their parameter measurements by  $\sim 40$  per cent on average without altering the parameters by more than 5 per cent. Elson (1992) removed the brightest 120 stars per cluster in the construction of her cleaned profiles – again, this provided much smoother profiles without altering the derived structural parameters by a significant amount. Some experimentation on our part showed similar results. While we do not find it necessary to remove quite so many stars, in the

cases listed in Table 3, it is evident from the final results presented in Fig. 6 that leaving the brightest (saturated) stars out of the construction process has resulted in clean, low noise profiles, which should reflect the underlying stellar distribution of each cluster.

#### 4.2.5 Error estimation

To estimate the internal error  $\sigma_i$  for an annulus we divided it into eight sectors of equal area, and calculated the surface brightness in each using Eq. 1 with the factors  $A_i$  set to unity. The internal error for the annulus is the standard deviation of the surface brightness values for these eight sectors (Djorgovski 1987). This technique ensures that the internal error of an annulus reflects the error due to the discreteness of the light distribution – that is, clumps of stars or single bright stars will increase the surface brightness of an annulus, but also its error by an appropriate amount. This is essential in the case of LMC clusters, many of which are patchy and irregular. Similarly, the error for an annulus reflects the width of that annulus – important given our four different annulus sets.

In the outer regions of most clusters however, we found that the error bars so calculated were considerably smaller than the random scatter in the points. As an example see Fig. 5, which demonstrates the background subtraction technique described in Section 4.3.2 but also well illustrates the present issue. The under-estimation is caused because  $A_i \sim 3$  for the outer annuli, so that while the flux for such an annulus is scaled to that for the full area, the errors are calculated over only a third of the full area and therefore do not reflect any large scale variations for that annulus. This effect is coupled with field star contamination for many clusters. This background is negligible in the inner regions of a cluster, but it can become significant in the outer regions. The background tends to be much more smoothly distributed than the cluster itself, and so artificially shrinks the error bars determined using sectors. To solve this problem, for every annulus we also calculated the error from Poisson statistics. When this became significantly larger than the sector error, we took the Poisson error instead. This condition only ever became true in the outer regions of clusters, meaning that in the central regions of a cluster the errors are sector errors, while in the outer regions they are Poisson errors, with a smooth transition across some intermediate region (usually  $\log r \sim 1.6$ ). The Poisson errors tend to over-estimate the scatter between points – this is due to the relatively low numbers of stars in the large outer annuli – but we find this preferable to an under-estimate, especially given our process of background subtraction (see Section 4.3.2).

Finally, we note that for some clusters, the (inner) sector errors are also larger than the RMS point-to-point scatter. In considering this, it is important that only the points in a single annulus set are compared – consecutive points from different annulus sets use at least some of the same information, so one would expect their scatter to be small. One should also examine the brightness range of a profile – some cover up to 9 magnitudes while others only 2 or 3 magnitudes. This can give the impression of enormous error bars on some profiles and tiny ones on others. Nonetheless, particularly in low surface brightness clusters such as NGC 1841, NGC 2121, NGC 2209, SL 663, and SL855, the effect persists. It is due to the low density of these clusters – the stars (especially the bright stars) are sparsely distributed. Therefore, while the surface brightness for each annulus is the azimuthal average over a comparatively large area, the eight sectors used to calculate the error for an annulus may have a considerable standard deviation in their surface brightnesses and correspondingly result in errors which are larger than the RMS scatter between points. In the richer clusters (e.g., NGC

1466, NGC 1805, NGC 1831, NGC 2210, etc) the errors match the RMS point-to-point scatter well.

### 4.3 Profile fitting and background subtraction

#### 4.3.1 King versus EFF profiles

Traditionally, the surface brightness profiles of old globular clusters are described by families of King-type models – for example the empirical King (1962) models:

$$\mu(r) = k \left\{ \frac{1}{[1 + (r/r_c)^2]^{\frac{1}{2}}} - \frac{1}{[1 + (r_t/r_c)^2]^{\frac{1}{2}}} \right\}^2 \quad (2)$$

where  $r_t$  is the tidal radius of the cluster, and  $r_c$  the core radius. Provided  $r_t \gg r_c$ , the core radius may be taken as the radius at which the surface brightness has dropped to half its central value. It is therefore useful to define the concentration parameter  $c = \log(r_t/r_c)$ . For LMC clusters, concentration parameters of  $1.0 \lesssim c \lesssim 2.0$  are measured (cf. EFF87) implying ratios  $10 \lesssim r_t/r_c \lesssim 100$ .

However, studies of young LMC clusters by Elson and collaborators (EFF87; Elson et al. (1989); E91) have shown that these clusters do not appear to be tidally truncated, even at radii of several hundred arcseconds. EFF87 argue that the lack of tidal truncation in a young cluster is due to the cluster expanding over its Roche limit as a result of mass loss or violent relaxation. Given that a young cluster has only completed a fraction of its orbit about the LMC, any stars outside the Roche limit will not have been tidally stripped and instead surround the cluster in an unbound halo. In this case, a more suitable profile is:

$$\mu(r) = \mu_0 \left( 1 + \frac{r^2}{a^2} \right)^{-\frac{\gamma}{2}} \quad (3)$$

where  $\mu_0$  is the central surface brightness,  $a$  is a measure of the core radius and  $\gamma$  is the power-law slope at large radii. For  $\gamma \sim 2$  this is essentially Eq. 2 with  $r_t \rightarrow \infty$ . We hereafter refer to profiles of the form of Eq. 3 as EFF models, after Elson, Fall & Freeman (1987), who first introduced them into star cluster research. Fig. 4 shows an empirical King model compared with an EFF model, both having been calculated with a core radius of  $r_c = 10''$ , typical of the LMC clusters measured by EFF87 and Mateo (1987). For the King profile we take  $c = 1.5$ . It is evident that there is little deviation between the two profiles in the inner regions. The difference only becomes large at radii approaching  $r_t$ .

The presence of both very young and very old clusters in our sample raises a potential dilemma over the fitting of one type of profile or the other, particularly for intermediate age clusters. Fortunately this is solved for us by the small field of view of WFPC2, which limits our surface brightness profiles to have maximum radii of  $r \sim 80''$  or  $\log r \sim 1.9$ . From Fig. 4 we see that at such radii the two profiles are essentially indistinguishable, and so we may fit either. Because of the virtual impossibility of obtaining any accurate information about  $r_t$  without measuring to at least this radius, we chose to fit EFF profiles to our data.

The parameter  $a$  in an EFF profile may be linked to the King core radius by setting  $\mu = \mu_0/2$  in Eq. 3 and rearranging to obtain

$$r_c = a(2^{2/\gamma} - 1)^{1/2} \quad (4)$$

We note that this assumes  $r_t \gg r_c$ , which is valid for most of the clusters in our sample. For several however (e.g., NGC 1841 and

NGC 2257)  $r_c$  is very large and  $\gamma$  quite steep. In such cases, Eq. 4 may underestimate the core radius by 3 to 10 per cent (Elson 1992).

#### 4.3.2 Fitting procedure and background subtraction

When fitting the profiles described in the previous section, in most cases it was necessary to correct for field star contamination. Especially for clusters near the LMC bar, the stellar background contribution is not negligible and tends to flatten out the cluster profiles in their outer regions (see e.g., Fig. 3). Because  $\gamma$  is largely determined from the slope of a profile well away from the core and is therefore very sensitive to field star contamination, we had to subtract the background level in order to avoid large systematic errors. Traditionally one would use an observation well away from the cluster to obtain the local background, and subtract this level from each annulus. However, we had no access to such background fields for our entire sample, nor were any of our fields large enough in area to allow background determinations away from a cluster. We therefore had to try and determine the background levels individually from each surface brightness profile.

One way of doing this is to fit Eq. 3 but with an extra parameter  $\phi(r)$  added – we set  $\phi$  as a constant to represent a simple background. However, these four-parameter fits did not work as well as desired – they tended to over-estimate the background, causing  $\gamma$  to be too steep by factors of up to three. The reason for this is not clear; it would seem that the creation of an additional degree of freedom degraded the quality of the fit for the original three parameters. We therefore implemented a recursive method using the fact that for  $r \gg a$ , Eq. 3 with a background contribution  $\phi$  becomes:

$$\begin{aligned} \mu(r) &\approx \mu_0 \left( \frac{r}{a} \right)^{-\gamma} + \phi \\ &\approx \mu_0 \left( \frac{r}{r_c} \right)^{-\gamma} (2^{2/\gamma} - 1)^{-\gamma/2} + \phi \end{aligned} \quad (5)$$

with Eq. 4 substituted for  $a$ .

We first fit an EFF model to the inner region of a cluster profile using the two narrow annulus sets, to estimate  $\mu_0$  and  $r_c$ . In this region ( $r \lesssim 30''$ ) the background contribution is negligible, in all cases being at least 5 magnitudes below the central surface brightness. The background therefore does not affect a measurement of the central surface brightness  $\mu_0$  nor the core radius  $r_c$ , which is essentially the shape of the profile in the inner region. Hence it is a good approximation to determine these without subtracting any background. We next use these estimated values and fit a two-parameter model ( $\gamma, \phi$ ) of the form of Eq. 5 to the outer region of the profile, using the two wider annulus sets and ensuring  $r \gg a$ . This allowed us to determine  $\phi$  and subtract it from every annulus. After the background subtraction, we calculate the Poisson errors for each point and substitute as appropriate (see Section 4.2.5). Finally, we fit another EFF model to the new subtracted profiles, using all four annulus sets, and thereby determine the best-fitting parameters. This method allows us to treat severely contaminated clusters (e.g., NGC 1898 and NGC 1916) equally with clusters that have no evident background contribution (e.g., Hodge 11 and NGC 1841).

To test the approximation described above, we examined the final parameters ( $\mu_0, r_c$ ) to see how well they corresponded to the determinations from the central fit. In no cases did we observe significant deviation, suggesting that the approximation is good. In addition, we checked for any systematic errors introduced by this method by comparing our determinations of  $\gamma$ , which is very sensitive to the background level, with previously published work. This

is presented in Section 5.1.1, and suggests that we introduced no significant systematic errors. A final point concerns the effect of non-constant backgrounds such as might be encountered near the bar – in this case,  $\phi = \phi(r)$ . Such a background would have two effects given the procedure described above. The first would be to cause a very small inaccuracy in our determined centre. The second would be to increase the noise in the outer region of a profile, because of the fact that we image only a fraction of any outer annulus. This in turn would cause a larger random error in the determination of  $\gamma$ , but this would be accounted for by our bootstrapping method of determining errors in the derived parameters (see below).

Fig. 5 shows an example of the background fitting, again for NGC 2005. In this case, the estimated parameters from the initial fit were  $a \sim 4''$  and  $\mu_0 \sim 16.9$ , and the background measured as  $V_{bg} = 21.83$ . As mentioned in Section 4.2.2, NGC 2005 is very near the LMC bar, and has a densely populated background field. The derived background intensities for this cluster and the others in the sample are consistent with the LMC isophote maps of de Vaucouleurs (1957). Equivalently, a plot of background intensity vs.  $R_{opt}$  shows the expected decrease with increasing  $R$ .

In implementing each fit, we develop a grid in parameter space and choose the combination of parameters which minimizes the weighted sum:

$$\chi^2 = \sum_{i=1}^{N_a} \left( \frac{\mu_i - \mu(r_i, \mu_0, a, \gamma)}{\sigma_i} \right)^2 \quad (6)$$

where  $\mu_i$  is the surface brightness of the  $i$ -th annulus,  $\sigma_i$  is the error in this value,  $N_a$  is the total number of annuli in the set in question, and the other parameters are as defined in Eq. 3. A refined mesh is then expanded about this parameter combination and the iteration continued until convergence. Given that our parameter space is topologically well behaved, this method was accurate and efficient, with convergence typically within ten iterations. Because our technique of using four annulus widths effectively counts each star four times, to maintain independence between data points we fit each annulus set individually as appropriate. To obtain the best fit curve for an iteration we average the individual fits, weighted by their  $\chi^2$  values. We determined errors in the three parameters obtained from the final fits to the background-subtracted profiles using a bootstrap method (Press et al. 1992, p691) with 1000 recursions per fit. Again, this was done separately for each annulus set to maintain the independence of the points. The errors so determined represent random errors in the best-fit parameters. Systematic errors such as those potentially introduced by the background fitting are not included in the estimation.

## 5 RESULTS

### 5.1 Profiles and structural parameters

The background-subtracted F555W surface brightness profiles for each of the 53 clusters are presented in Fig. 6. We plot each of the four annulus sets on the same axes, to demonstrate the high degree of consistency between them. For each cluster, the best fit EFF profile is also plotted, the core radius indicated, and the best fit parameters listed. These results are summarized in Table 4 along with their corresponding errors, the calculated centre of each cluster and the maximum radial extent  $r_m$  of each profile. Three of the profiles (NGC 1754, NGC 1786, NGC 1916) are incomplete in their inner regions – this is due to the effects of crowding, even including supplementary photometry from short exposures (a short expo-

sure was unavailable for NGC 1786, however). The derived core radii for these clusters, and for the clusters NGC 1835, NGC 2005, NGC 2019 and R136 which also required short exposure photometry, should be considered upper limits.

This is one of the largest published studies of LMC cluster surface brightness profiles, and as far as we are aware, the only one to use *HST* data. In addition, approximately one quarter of the clusters in the sample do not have previously published surface brightness profiles. There is much to be learned from such detailed data, covering many aspects of globular cluster and LMC astronomy. We can however split the sample into sub-groups and obtain some immediate and interesting results, which we discuss below. We first compare our results with those from the several other published large-scale studies.

#### 5.1.1 Comparison with previous work

At least three-quarters of the clusters studied in this paper have published surface brightness profiles, concentrated mainly in four large studies – those of EFF87, Mateo (1987), E91 (see also Elson et al. (1989)), and Kontizas and collaborators (Kontizas et al. 1987a; Kontizas et al. 1987b; Metaxa et al. 1988; Chrysovergis et al. 1989). It is useful to compare our results to those from these papers and thereby establish the validity of our reduction procedure.

In particular, our background subtraction procedure might introduce systematic errors into the measured structural parameters. We checked this by comparing our derived values for  $\gamma$  with those from EFF87 for the 10 young clusters ( $\tau \leq 3 \times 10^8$  yr) in their sample, since  $\gamma$  is very sensitive to the subtracted background. The comparison is plotted in Fig. 7. The profiles from EFF87 extend to typically  $r_m \sim 250''$  and their background measurements are made at these large radii. The agreement with our fitted values of  $\gamma$  is generally good, and within the errors for most points. If anything there is a slight tendency for our  $\gamma$  measurements to be slightly larger than those from EFF87 (i.e., we slightly over-estimated the background – as would be expected), but this discrepancy is not significant. EFF87 find a range of  $2.2 \lesssim \gamma \lesssim 3.2$  and a median value  $\gamma \approx 2.6$ . For the same ten clusters we find a range of  $2.26 \lesssim \gamma \lesssim 3.45$  but a median value  $\gamma \approx 2.95$ . We note however that the sample size is barely large enough for meaningful statistics. Extending the average to cover the 22 clusters in our sample with  $\tau \leq 3 \times 10^8$  yr we obtain a range  $2.01 \lesssim \gamma \lesssim 3.79$  and a median  $\gamma \approx 2.59$ . We are therefore confident that our background subtraction method has not introduced any significant systematic errors into the structural parameter measurements.

We have also taken the core radii from the first three studies listed above for all the clusters in common with our sample, and plotted these against our measured values (Fig. 8). Again, the agreement is relatively good; however there is some considerable scatter in the plot. Nonetheless, there are good explanations for many of the errant points. Our core radii are generally somewhat larger than those measured by EFF87 (filled triangles) – however the inner regions of the profiles from EFF87 are a combination of literature data and photomultiplier aperture measurements and the errors quoted for  $a$  are up to 50 per cent and more, which would bring most if not all of our results well into the error margins. More encouraging is the good agreement of our measurements with those from E91 (filled circles), again for relatively young clusters ( $10^7 < \tau < 10^9$  yr). The profiles from this study were measured from CCD images, with backgrounds determined at  $r \sim 200''$ . The most errant point (falling well below the equality line) is for the young cluster NGC 2100. We speculate that the different satu-

**Table 4.** Structural parameters for the cluster sample derived from the best-fitting F555W EFF profiles.

Cluster Name	Centre (J2000.0) <sup>a</sup>		$\mu_{555}(0)^b$	$a$	$\gamma$	$r_c$	$r_c$	$r_m$
	$\alpha$	$\delta$		( $''$ )		( $''$ )	(pc) <sup>c</sup>	( $''$ )
NGC1466	03 <sup>h</sup> 44 <sup>m</sup> 32 <sup>s</sup> .9	-71°40'13"	19.08 ± 0.05	14.89 ± 0.79	3.31 ± 0.12	10.73 ± 0.36	2.61 ± 0.09	76
NGC1651	04 <sup>h</sup> 37 <sup>m</sup> 31 <sup>s</sup> .1	-70°35'02"	20.38 ± 0.04	15.82 ± 1.26	2.21 ± 0.12	14.75 ± 0.70	3.58 ± 0.17	76
NGC1711	04 <sup>h</sup> 50 <sup>m</sup> 37 <sup>s</sup> .3	-69°59'04"	18.28 ± 0.05	10.93 ± 0.83	2.78 ± 0.13	8.78 ± 0.44	2.13 ± 0.11	72
NGC1718	04 <sup>h</sup> 52 <sup>m</sup> 25 <sup>s</sup> .6	-67°03'06"	19.18 ± 0.07	9.38 ± 0.76	2.31 ± 0.10	8.52 ± 0.49	2.07 ± 0.12	76
NGC1754	04 <sup>h</sup> 54 <sup>m</sup> 18 <sup>s</sup> .9	-70°26'31"	17.48 ± 0.26	4.12 ± 0.65	2.43 ± 0.09	3.61 ± 0.49	0.88 ± 0.12	76
NGC1777	04 <sup>h</sup> 55 <sup>m</sup> 48 <sup>s</sup> .9	-74°17'03"	20.01 ± 0.02	16.62 ± 0.89	2.60 ± 0.10	13.96 ± 0.44	3.39 ± 0.11	76
NGC1786	04 <sup>h</sup> 59 <sup>m</sup> 07 <sup>s</sup> .9	-67°44'45"	17.46 ± 0.11	6.79 ± 0.67	2.78 ± 0.13	5.45 ± 0.38	1.33 ± 0.09	76
NGC1805	05 <sup>h</sup> 02 <sup>m</sup> 21 <sup>s</sup> .8	-66°06'42"	18.01 ± 0.06	6.84 ± 0.42	2.81 ± 0.10	5.47 ± 0.23	1.33 ± 0.06	69
NGC1818	05 <sup>h</sup> 04 <sup>m</sup> 13 <sup>s</sup> .8	-66°26'02"	18.36 ± 0.05	12.50 ± 0.78	2.76 ± 0.12	10.10 ± 0.39	2.45 ± 0.09	76
NGC1831	05 <sup>h</sup> 06 <sup>m</sup> 17 <sup>s</sup> .4	-64°55'11"	19.08 ± 0.04	25.81 ± 1.59	3.41 ± 0.19	18.28 ± 0.59	4.44 ± 0.14	76
NGC1835	05 <sup>h</sup> 05 <sup>m</sup> 06 <sup>s</sup> .7	-69°24'15"	16.37 ± 0.08	6.35 ± 0.46	3.11 ± 0.10	4.76 ± 0.26	1.16 ± 0.06	76
NGC1841	04 <sup>h</sup> 45 <sup>m</sup> 23 <sup>s</sup> .9	-83°59'56"	21.59 ± 0.02	53.62 ± 5.07	4.55 ± 0.61	32.00 ± 0.72	7.77 ± 0.17	78
NGC1847	05 <sup>h</sup> 07 <sup>m</sup> 07 <sup>s</sup> .7	-68°58'17"	18.54 ± 0.06	8.58 ± 0.44	2.05 ± 0.13	8.44 ± 0.34	2.05 ± 0.08	42
NGC1850	05 <sup>h</sup> 08 <sup>m</sup> 41 <sup>s</sup> .2	-68°45'31"	16.70 ± 0.07	11.11 ± 1.03	2.18 ± 0.11	10.48 ± 0.64	2.55 ± 0.16	69
NGC1856	05 <sup>h</sup> 09 <sup>m</sup> 31 <sup>s</sup> .5	-69°07'46"	16.68 ± 0.07	6.81 ± 0.46	2.01 ± 0.05	6.80 ± 0.36	1.65 ± 0.09	76
NGC1860	05 <sup>h</sup> 10 <sup>m</sup> 38 <sup>s</sup> .9	-68°45'12"	19.72 ± 0.11	9.74 ± 0.53	2.25 ± 0.13	9.00 ± 0.50	2.19 ± 0.12	76
NGC1866	05 <sup>h</sup> 13 <sup>m</sup> 38 <sup>s</sup> .9	-65°27'52"	18.52 ± 0.02	18.60 ± 0.72	3.04 ± 0.09	14.15 ± 0.32	3.44 ± 0.08	76
NGC1868	05 <sup>h</sup> 14 <sup>m</sup> 36 <sup>s</sup> .2	-63°57'14"	17.99 ± 0.04	8.83 ± 0.41	3.07 ± 0.10	6.67 ± 0.19	1.62 ± 0.05	76
NGC1898	05 <sup>h</sup> 16 <sup>m</sup> 42 <sup>s</sup> .4	-69°39'25"	19.05 ± 0.06	8.79 ± 0.91	2.14 ± 0.14	8.40 ± 0.55	2.04 ± 0.13	76
NGC1916	05 <sup>h</sup> 18 <sup>m</sup> 37 <sup>s</sup> .5	-69°24'25"	15.93 ± 0.09	4.08 ± 0.28	2.70 ± 0.08	3.35 ± 0.18	0.81 ± 0.04	76
NGC1984	05 <sup>h</sup> 27 <sup>m</sup> 40 <sup>s</sup> .8	-69°08'05"	18.62 ± 0.11	4.44 ± 0.41	2.27 ± 0.11	4.07 ± 0.28	0.99 ± 0.07	76
NGC2004	05 <sup>h</sup> 30 <sup>m</sup> 40 <sup>s</sup> .9	-67°17'09"	16.93 ± 0.08	7.56 ± 0.86	2.53 ± 0.12	6.47 ± 0.53	1.57 ± 0.13	76
NGC2005	05 <sup>h</sup> 30 <sup>m</sup> 10 <sup>s</sup> .3	-69°45'09"	17.04 ± 0.13	4.33 ± 0.54	2.60 ± 0.14	3.63 ± 0.33	0.88 ± 0.08	69
NGC2011	05 <sup>h</sup> 32 <sup>m</sup> 19 <sup>s</sup> .6	-67°31'14"	18.93 ± 0.15	5.17 ± 0.60	2.22 ± 0.09	4.81 ± 0.51	1.17 ± 0.12	76
NGC2019	05 <sup>h</sup> 31 <sup>m</sup> 56 <sup>s</sup> .6	-70°09'33"	16.73 ± 0.10	4.21 ± 0.37	2.52 ± 0.09	3.61 ± 0.24	0.88 ± 0.06	76
NGC2031	05 <sup>h</sup> 33 <sup>m</sup> 41 <sup>s</sup> .1	-70°59'13"	18.93 ± 0.06	11.13 ± 0.98	2.09 ± 0.11	10.81 ± 0.61	2.63 ± 0.15	76
NGC2100	05 <sup>h</sup> 42 <sup>m</sup> 08 <sup>s</sup> .6	-69°12'44"	16.26 ± 0.14	5.73 ± 0.75	2.44 ± 0.14	5.02 ± 0.50	1.22 ± 0.12	76
NGC2121	05 <sup>h</sup> 48 <sup>m</sup> 11 <sup>s</sup> .6	-71°28'51"	20.90 ± 0.02	33.83 ± 3.83	2.25 ± 0.28	31.22 ± 1.14	7.59 ± 0.28	76
NGC2136	05 <sup>h</sup> 52 <sup>m</sup> 58 <sup>s</sup> .0	-69°29'36"	17.37 ± 0.09	12.33 ± 1.06	3.79 ± 0.23	8.19 ± 0.43	1.99 ± 0.10	69
NGC2153	05 <sup>h</sup> 57 <sup>m</sup> 51 <sup>s</sup> .2	-66°23'58"	19.17 ± 0.09	4.71 ± 0.79	2.64 ± 0.22	3.91 ± 0.44	0.95 ± 0.11	69
NGC2155	05 <sup>h</sup> 58 <sup>m</sup> 33 <sup>s</sup> .3	-65°28'35"	20.44 ± 0.05	20.30 ± 2.20	2.85 ± 0.25	16.06 ± 0.98	3.90 ± 0.24	76
NGC2156	05 <sup>h</sup> 57 <sup>m</sup> 49 <sup>s</sup> .7	-68°27'41"	18.98 ± 0.07	8.15 ± 0.51	2.79 ± 0.09	6.53 ± 0.31	1.59 ± 0.08	76
NGC2157	05 <sup>h</sup> 57 <sup>m</sup> 32 <sup>s</sup> .4	-69°11'49"	17.78 ± 0.05	13.76 ± 0.91	3.45 ± 0.18	9.68 ± 0.36	2.35 ± 0.09	76
NGC2159	05 <sup>h</sup> 58 <sup>m</sup> 03 <sup>s</sup> .0	-68°37'27"	19.66 ± 0.05	12.73 ± 0.94	3.00 ± 0.15	9.77 ± 0.47	2.37 ± 0.11	69
NGC2162	06 <sup>h</sup> 00 <sup>m</sup> 30 <sup>s</sup> .4	-63°43'19"	19.92 ± 0.08	12.97 ± 1.40	2.91 ± 0.23	10.13 ± 0.66	2.46 ± 0.16	76
NGC2164	05 <sup>h</sup> 58 <sup>m</sup> 55 <sup>s</sup> .9	-68°31'00"	18.22 ± 0.05	10.16 ± 0.43	2.96 ± 0.07	7.85 ± 0.24	1.91 ± 0.06	72
NGC2172	06 <sup>h</sup> 00 <sup>m</sup> 06 <sup>s</sup> .4	-68°38'15"	20.21 ± 0.07	13.77 ± 0.97	2.94 ± 0.14	10.68 ± 0.49	2.60 ± 0.12	76
NGC2173	05 <sup>h</sup> 57 <sup>m</sup> 58 <sup>s</sup> .5	-72°58'40"	19.86 ± 0.05	13.13 ± 1.35	2.37 ± 0.16	11.70 ± 0.74	2.84 ± 0.18	76
NGC2193	06 <sup>h</sup> 06 <sup>m</sup> 17 <sup>s</sup> .0	-65°05'54"	19.77 ± 0.08	7.65 ± 0.71	2.50 ± 0.11	6.59 ± 0.43	1.60 ± 0.10	72
NGC2209	06 <sup>h</sup> 08 <sup>m</sup> 34 <sup>s</sup> .8	-73°50'12"	22.09 ± 0.06	22.97 ± 2.39	2.08 ± 0.16	22.34 ± 1.34	5.43 ± 0.33	76
NGC2210	06 <sup>h</sup> 11 <sup>m</sup> 31 <sup>s</sup> .5	-69°07'17"	18.18 ± 0.05	11.75 ± 0.56	3.51 ± 0.12	8.18 ± 0.24	1.99 ± 0.06	76
NGC2213	06 <sup>h</sup> 10 <sup>m</sup> 42 <sup>s</sup> .2	-71°31'46"	19.16 ± 0.05	9.36 ± 0.69	2.84 ± 0.13	7.43 ± 0.36	1.80 ± 0.09	76
NGC2214	06 <sup>h</sup> 12 <sup>m</sup> 55 <sup>s</sup> .8	-68°15'38"	18.36 ± 0.07	9.55 ± 0.99	2.26 ± 0.14	8.79 ± 0.59	2.14 ± 0.14	76
NGC2231	06 <sup>h</sup> 20 <sup>m</sup> 42 <sup>s</sup> .7	-67°31'10"	20.48 ± 0.12	11.42 ± 2.79	2.07 ± 0.26	11.14 ± 1.55	2.71 ± 0.38	76
NGC2249	06 <sup>h</sup> 25 <sup>m</sup> 49 <sup>s</sup> .8	-68°55'13"	19.05 ± 0.04	12.13 ± 0.83	3.40 ± 0.17	8.61 ± 0.35	2.09 ± 0.09	76
NGC2257	06 <sup>h</sup> 30 <sup>m</sup> 12 <sup>s</sup> .1	-64°19'42"	20.93 ± 0.03	38.61 ± 2.71	3.54 ± 0.27	26.75 ± 0.73	6.50 ± 0.18	76
SL663	05 <sup>h</sup> 42 <sup>m</sup> 28 <sup>s</sup> .8	-65°21'44"	22.40 ± 0.05	28.83 ± 2.24	2.13 ± 0.15	27.60 ± 1.27	6.71 ± 0.31	76
SL842	06 <sup>h</sup> 08 <sup>m</sup> 14 <sup>s</sup> .9	-62°59'15"	21.07 ± 0.11	14.55 ± 1.75	3.37 ± 0.29	10.37 ± 0.76	2.52 ± 0.18	69
SL855	06 <sup>h</sup> 10 <sup>m</sup> 53 <sup>s</sup> .7	-65°02'30"	22.93 ± 0.03	23.10 ± 2.91	2.12 ± 0.23	22.18 ± 1.35	5.39 ± 0.33	76
HODGE4	05 <sup>h</sup> 32 <sup>m</sup> 25 <sup>s</sup> .2	-64°44'11"	20.59 ± 0.06	15.84 ± 1.65	2.13 ± 0.15	15.20 ± 1.08	3.69 ± 0.26	76
HODGE11	06 <sup>h</sup> 14 <sup>m</sup> 22 <sup>s</sup> .3	-69°50'50"	19.60 ± 0.05	13.66 ± 1.17	2.38 ± 0.12	12.14 ± 0.66	2.95 ± 0.16	76
HODGE14	05 <sup>h</sup> 28 <sup>m</sup> 39 <sup>s</sup> .3	-73°37'49"	20.28 ± 0.09	8.38 ± 0.93	2.41 ± 0.16	7.39 ± 0.56	1.80 ± 0.14	76
R136	05 <sup>h</sup> 38 <sup>m</sup> 42 <sup>s</sup> .5	-69°06'03"	12.66 ± 0.09	1.48 ± 0.12	2.43 ± 0.09	1.30 ± 0.08	0.32 ± 0.02	10

<sup>a</sup> We find our centering algorithm to be repeatable to approximately  $\pm 1''$ , notwithstanding image header inaccuracies (see Section 4.1). Given this precision, coordinates in  $\delta$  are provided to the nearest arcsecond. Those in  $\alpha$  are reported to the nearest tenth of a second, but the reader should bear in mind that at  $\delta = -69^\circ$ , one second of RA corresponds to approximately five seconds of arc – in other words, the uncertainty in  $\alpha$  is approximately  $\pm 0.2$ .

<sup>b</sup> The  $V_{555}$  magnitude of one square arcsecond at the centre of a given cluster.

<sup>c</sup> When converting to parsecs we assume an LMC distance modulus of 18.5 which equates to a scale of 4.116 arcsec pc<sup>-1</sup>.

ration limits between the two studies ( $12 \lesssim V \lesssim 19$  from E91 as compared with  $15 \lesssim V_{555} \lesssim 22$  from the present study) might be the root of this difference. Furthermore, we have adopted the core radius measurements from E91 not corrected for seeing, because there is some evidence of over-correction in the quoted values. The seeing corrections move the errant point considerably to the left on the plot, but also move most of the other points to the left and away from the equality line.

Both the studies by EFF87 and E91 describe the profiles of many young LMC clusters as being very irregular in comparison to the smooth profiles typical of old globular clusters. We also observe such irregularities, in the same forms as those noted by E91 – that is, bumps (e.g., NGC 2004), steps and wiggles (e.g., NGC 1711, NGC 1856), sharp shoulders or dips near the core radius (e.g., NGC 1850, NGC 1860, NGC 1984) and central dips (e.g., NGC 2031).

The measurements from the study of Mateo (1987) for old LMC clusters (filled squares), are from *B*-band images and so are not strictly comparable with ours; however we proceed for the sake of completeness. Again, there are no significant systematic differences, and most errant points can be explained. The four smallest core radii from Mateo all correspond to upper limit measurements in our study – so the points likely lie closer to the equality line than indicated. The two errant points to the right of the plot are estimates taken from the literature – the exact method of estimation is not clear, but we conjecture that it might be a significant cause of the observed differences. We also note good agreement with the core radius for NGC 2257 ( $25''.1$  as compared with our measurement of  $26''.75 \pm 0''.73$ ), which falls outside the plot.

It is more difficult to reconcile our results with those from the four studies of Kontizas et al. (1987a; 1987b), Metaxa et al. (1988), and Chrysovergis et al. (1989), which use density profiles from number counts. While this again means the derived parameters are not strictly comparable with ours, the two sets should be roughly similar. However, we observe a large, apparently random scatter between them. The authors report that their core radius estimates are derived from King model fits to the density profiles, which yield  $r_t$  and the concentration  $c$ , and that the errors are  $\sim 15$  per cent in  $r_t$  and  $\pm 0.25$  in  $c$ , which is  $\sim 20$  per cent in the typical value  $c \approx 1.5$ . We estimate that these errors could cause uncertainties of the order of  $\pm 60$  per cent or more in derived values of  $r_c$ , consistent with the difficulties associated with counting stars in crowded regions on photographic plates and the resolution of the profiles (most do not extend within  $\sim 25''$ ). Such uncertainties can account for most of the observed scatter. Nonetheless, several measurements are discrepant by factors of up to 10 (e.g.,  $r_c \approx 55''$  for NGC 1805 as compared with our measurement of  $r_c = 5''.5$ ) and we are unable offer a plausible explanation to fully reconcile these.

### 5.1.2 Double clusters and profile bumps

There is a small amount of evidence for double clusters in our sample. In particular, NGC 1850 is a well known double cluster, with a much smaller and younger companion – NGC 1850B – separated by approximately  $32''$  (see e.g., Gilmozzi et al. (1994)). It is not clear that NGC 1850B is physically associated with NGC 1850 – it may be a chance superposition of two clusters along the same line of sight. Measurements of the mass of each cluster, and their three dimensional separation and relative velocity are required to settle this issue.

Nonetheless, NGC 1850B appears in our images, and its presence can be seen in the surface brightness profile for NGC 1850 as a bump at  $\log r \sim 1.55$ . We also show our WFC2 *V*-band image of

NGC1850 in Fig. 9 – in this image, the centre of NGC1850 is to the lower left, and NGC1850B is evident to the upper right of the main cluster. The over-sampling of our data has the effect of smearing out sharp features in the surface brightness profiles. For example, a very bright star will appear once in each annulus set, resulting in four points at slightly different radii and giving the impression of a bump rather than a spike. This makes the bump in the profile of NGC 1850 almost indistinguishable from that which would be caused by a bright star, although upon examination of the actual image, the nature of NGC 1850B is immediately apparent. Our unpublished CMD for NGC 1850 also shows evidence of this young sub-cluster in the form of a few main sequence stars above the turn-off for the main cluster. We also note that because each annulus is essentially an azimuthal average, the amplitude of the bump due to NGC 1850B is reduced – that is, the peak surface brightness of NGC 1850B is certainly much greater than indicated in the surface brightness profile for NGC 1850.

The above result prompted us to search the other cluster images and profiles (correlating the two against each other) for similar evidence of double clusters, even though only two of our sample, NGC 2011 and NGC 2136, appear in the catalogue of LMC double clusters published by Bhatia et al. (1991). None of the images showed any evident double clusters. Surprisingly, we did however locate two very prominent bumps in the profiles of NGC 2153 and NGC 2213, at  $\log r \sim 1.15$  ( $14''$ ) and  $\log r \sim 1.25$  ( $18''$ ) respectively. We show DSS2 *R*-band images of each of these clusters in Fig.9. It is clear from these images, and from our WFPC2 images, that secondary clusters are not the cause of these bumps. Furthermore, although it is evident from the images that each cluster contains bright stars, neither of the bumps can be due to a single bright star, because each bump appears in at least two consecutive points from single annulus sets (the  $1''.5$ ,  $2''$  and  $3''$  sets for NGC 2156, and the  $1''.5$  and  $2''$  sets for NGC 2213). It is therefore not clear what the cause of either bump is. It is however clear that the binarity of a cluster cannot be judged from its surface brightness profile, because these examples show that even single clusters can have significant bumps in their profiles.

One possibility which is evident from the DSS images (but not necessarily so clear on the high resolution WFPC2 images) is that the chance positioning of several bright stars at exactly the right distance from a given cluster's centre but with different position angles could result in a bump. For NGC 2153, there is an arc of stars to the north of the main cluster and a fainter arc to the south which are at approximately the right distance to match the bump in the profile. There is also a bright star to the south, but this is saturated on our WFPC2 images. Whether these arcs are simply random placement of several stars, or a physical association is not clear. For NGC 2213, it would appear that there are several bright stars at approximately the right distance from the centre but at different angles about the cluster, which might cause the bump in its profile. Again, whether any physical significance can be attached to this bump is uncertain.

In addition, three other clusters – NGC 2004, NGC 2155, and NGC 2159 – have less statistically significant bumps in their profiles, at  $\log r \sim 1.25$  ( $18''$ ),  $\log r \sim 1.3$  ( $20''$ ), and  $\log r \sim 1.3$  ( $20''$ ) respectively. We show DSS2 *R*-band images of these clusters, also in Fig. 9. Just as for NGC 2153 and NGC 2213, it is not immediately clear what the causes of these bumps are. Certainly they are not due to single bright stars, and again there are no clear sub-clusters like NGC 1850B. NGC 2004 shows a ring of bright stars about its centre, but these are at too great a radius to cause the observed bump. We do note a slight extension of the main cluster

towards the upper left – this is also apparent in the WFPC2 image and might be the source of the bump in the profile. Again, the physical significance of this extension is not clear. For NGC 2155, there is no evident source for the bump, although this cluster does show a clumpy and dispersed structure. Finally, for NGC 2159, again the bump may be caused by several bright stars at the right distance from the centre but at different position angles. There is no other structure evident which might cause the bump in its profile.

The profiles for NGC 2011 and NGC 2136, the only clusters in our sample apart from NGC 1850 to appear in the catalogue by Bhatia et al. (1991) do not show any structure that might be due to their binary nature. However, both companions lie outside the respective fields of view for these clusters. NGC 1818 also likely has a small companion (see e.g., de Grijs et al. (2002a)) but the separation is  $\sim 90''$  and it again lies outside our field of view. NGC 2214 is regarded by some authors as a binary cluster in the late stages of a merger (Bhatia & MacGillivray 1988), and has been noted to have an anomalous core (Meylan & Djorgovski 1987). We do not observe any significant bumps in our surface brightness profile for this cluster, or any interesting structure in our image, but we do see a similar effect to that described by Meylan & Djorgovski where the surface brightness profile in the core appears similar to that for a post core-collapse cluster. That NGC 2214 is such a cluster is unlikely given its age ( $\sim 60$  Myr). Finally, NGC 2156 is rendered interesting because of the results of de Oliveira et al. (2000) who measure this cluster to have somewhat elliptical isophotes. Upon comparison with the results of  $N$ -body simulations of star cluster encounters, they conclude that this ellipticity could result from a binary cluster interaction, given a favourable viewing angle. Moreover, the young age of NGC 2156 combined with the behaviour of the simulation suggests that the merging cluster will not yet have been disrupted. However, we observe no evidence for such a distinct sub-cluster in our images, or any structure in the surface brightness profile.

### 5.1.3 Post core-collapse clusters

We find strong evidence for several post core-collapse (PCC) clusters amongst the old clusters in our sample. Theoretical studies, as well as observations of the Galactic globular cluster system have shown that the surface brightness profiles of PCC clusters are characterized by power-law cusps in their central regions, rather than ordinary King-type models. We have identified two clusters with profiles which clearly show such cusps as well as breaks to the power-law regions, and another two clusters which show cusps and breaks at lower significance. A further three clusters have incomplete profiles in their central regions (a result of severe crowding in these regions – see Section 4.2.2 and the beginning of Section 5) but do appear to show breaks similar to the other four PCC candidates. The three groups of clusters are, respectively: NGC 2005 and NGC 2019; NGC 1835 and NGC 1898; and NGC 1754, NGC 1786, and NGC 1916.

We first address NGC 2005 and NGC 2019, which have profiles clearly showing PCC-like cusps. This has previously been noted by Mateo (1987) for both clusters, and by Meylan & Djorgovski (1987) for NGC 2019. Mateo estimates power-law slopes of  $\beta \sim 1$  for both clusters, where we assume the profile goes as  $r^{-\beta}$  in the central regions. He also notes sharp breaks in both profiles at the transition to the power-law region, which occur at  $4''.4 \pm 0''.4$  for NGC 2005 and  $3''.6 \pm 0''.4$  for NGC 2019. We observe well defined power-law regions for both clusters, with sharp breaks at  $5''.6 \pm 0''.3$  for NGC 2005 and  $5''.0 \pm 0''.6$  for NGC 2019, both slightly larger

than the measurements of Mateo. If we fit power-law profiles to these inner sections, we obtain slopes of  $\beta = 0.74$  for NGC 2005 and  $\beta = 0.71$  for NGC 2019. The profiles and power-law models are shown in Fig. 10(a) and (b), together with the best fitting EFF models. Clearly, for each cluster the power-law is a better fit in the centre than the EFF model. Further, it is interesting that studies of Galactic PCC clusters have measured slopes in the range 0.6 to 0.8 (Lugger, Cohn & Grindlay 1995), or with a median value  $\beta \approx 0.9$  (Djorgovski & King 1986), and many of the PCC Galactic clusters also show breaks in their profiles (see Fig. 2 in Djorgovski & King, and Fig. 2(a-r) in Lugger et al.).

NGC 1835 and NGC 1898 also appear to show power-law cusps and breaks, but at lower significance than NGC 2005 and NGC 2019. The profiles for these two clusters are shown in Fig. 10(c) and (d) respectively, along with power-law fits to the central profile regions, and the best fitting EFF models. For each cluster, a power-law seems to model the central data better than an EFF profile, although for NGC 1898 the difference is small. The power law slopes are  $\beta = 0.45$  for NGC 1835, and  $\beta = 0.30$  for NGC 1898, and the break radii are  $4''.2 \pm 0''.4$  and  $6''.3 \pm 1''.2$  respectively. Profiles for NGC 1835 have been published by both Elson & Freeman (1985) and Mateo (1987); however, while both show NGC 1835 to have a small core, neither find a power law region or a break.

The three remaining clusters have incomplete profiles in their inner regions because of severe crowding. Even using short exposure photometry (Section 4.2.3) for NGC 1754 and NGC 1916, the incompleteness could not be overcome, while NGC 1786 had no supplementary images available. The profiles for these three clusters are shown in Fig. 10(e-g). Given the lack of data, we cannot assert even that these three clusters are PCC candidates; nonetheless, they warrant further attention because they all appear to show breaks in their profiles at very similar radii to those observed for NGC 2005 and NGC 2019. Clusters with ordinary King-type profiles should not show such breaks. Each of the three profiles is complete to several points further in than its break, and we attempted to fit power-law models to these points even though there are very few of them in each case – the idea being to explore the matter further by comparing potential power-law models to the best fitting EFF models. We obtained slopes of  $\beta = 0.74$  for NGC 1754,  $\beta = 0.90$  for NGC 1786, and  $\beta = 1.17$  for NGC 1916. Interestingly, these values are very close to those found for NGC 2005 and NGC 2019, especially given that the uncertainties for fits to only a few points (just three in the case of NGC 1754) are large.

Profiles for both NGC 1754 and NGC 1786 are given by Mateo (1987); however he finds that neither show power-law regions or breaks. Similarly, Meylan & Djorgovski (1987) observe NGC 1786, and they classify it as having a normal King-type profile. There is no published profile for NGC 1916. We find that for each of the three clusters, both the power-law profile and the EFF profile fit the data equally well around the break radius – hence we do not assert that these three clusters are PCC candidates. However, we believe that all three clusters warrant further high resolution observations to obtain complete profiles. It is suggestive that not only do these clusters seem to show breaks in their profiles, but each appears at least as compact as both NGC 2005 and NGC 2019, which are our leading PCC candidates, but which do not suffer as badly from crowding as do NGC 1754, NGC 1786 and NGC 1916.

The results of the power-law fits for the seven clusters are summarized in Table 5, including the break radius for each cluster. On the basis of the above analysis, we conclude that NGC 2005 and NGC 2019 are strong PCC candidates, while NGC 1754, NGC 1786, and NGC 1916 deserve further detailed study. The status of

**Table 5.** Power-law slopes and break radii for seven potential PCC clusters.

Cluster	$r_c$ (")	$\beta$	$\log r_{break}$ (")	$r_{break}$ (")
NGC2005	$3.63 \pm 0.33$	0.74	$0.75 \pm 0.02$	$5.6 \pm 0.3$
NGC2019	$3.61 \pm 0.24$	0.71	$0.70 \pm 0.05$	$5.0 \pm 0.6$
NGC1835	$4.76 \pm 0.26$	0.45	$0.62 \pm 0.04$	$4.2 \pm 0.4$
NGC1898	$8.40 \pm 0.55$	0.30	$0.80 \pm 0.08$	$6.3 \pm 1.2$
NGC1754	$3.61 \pm 0.41$	0.74	$0.62 \pm 0.04$	$4.2 \pm 0.4$
NGC1786	$5.45 \pm 0.38$	0.90	$0.75 \pm 0.04$	$5.6 \pm 0.5$
NGC1916	$3.35 \pm 0.18$	1.17	$0.82 \pm 0.07$	$6.6 \pm 1.1$

Note:  $r_c$  is the core radius of the best fitting EFF profile, from Table 4;  $\beta$  is the slope of the best fitting power-law model;  $r_{break}$  is the break radius observed from Fig. 10 with errors estimated by eye.

NGC 1835 and NGC 1898 is unclear. While they both have central regions which are fit better by power-law models than EFF models, the power-law slopes are shallower than those typically associated with PCC clusters. However, both show breaks at similar radii to NGC 2005 and NGC 2019. Physically, NGC 1835 is very similar in appearance to these two clusters, and we therefore consider it also a PCC candidate. NGC 1898 is a much more open cluster, and we speculate that it is perhaps on the verge of core-collapse. It is interesting that Olsen et al. (1998) find NGC 1898 to be  $\sim 3$  Gyr younger than NGC 1835, NGC 2005 and NGC 2019.

Given these results, we briefly consider the LMC old cluster population as a whole. In addition to the twelve clusters in the present sample (adding NGC 1466, NGC 1841, NGC 2210, NGC 2257, and Hodge 11 to the seven discussed above) there are three more suspected old LMC clusters – Reticulum, which is definitely old and likely a member of the LMC based on its radial velocity (Suntzeff et al. 1992); and NGC 1928 and NGC 1939, which are definitely LMC members and likely to be old based on the spectroscopic study of Dutra et al. (1999). Of the twelve measured in the present study, we suggest that  $3 \pm 1$  are good PCC candidates. Of the three not measured in the present study, Reticulum is definitely not (Suntzeff et al. (1992) estimate a core radius of  $\sim 13$  pc), and NGC 1928 and NGC 1939 are unknown as far as we are aware. Therefore we estimate that  $20 \pm 7$  per cent of old LMC clusters are PCC clusters, a value which matches well the  $\sim 20$  per cent estimated by Djorgovski & King (1986) for Galactic clusters. In addition, all the candidate LMC PCC clusters, as well as NGC 1754, NGC 1786, NGC 1916, NGC 1928 and NGC 1939 (which all require further study) are in the bar region, at projected radii less than  $\sim 2.5^\circ$  from the optical centre of the LMC. Similarly, Djorgovski & King find the Galactic PCC clusters to be centrally concentrated.

### 5.1.4 R136

R136 is the extremely compact, very young ( $\tau = 3$  Myr) central cluster of the 30 Doradus H II region, which is the most luminous H II region in the local group. Because of its unique characteristics, we briefly describe it separately here.

The surface brightness profile for R136 and the surrounding cluster NGC 2070 is clearly separable into two regions – an inner region which is well fit by an EFF profile with  $r_c = 1''.3$  and  $\gamma = 2.43$  to a radius  $r \sim 10''$  (see Fig. 6 and Table 4), and beyond this,

a break to a shallower profile. This is consistent with the review of Meylan (1993) in which he finds a two-component King model necessary to fit his observed surface brightness profile. The first component in his model has core radius  $r_c = 1''.3$ , equivalent with our measurement, and the second component a core radius  $r_c = 15''$ . Following in this vein, we attempted a two-component fit to our profile. Fitting two EFF profiles, we found the best fitting core component to match our previously measured core profile, with the outer profile best fit by  $\mu \sim 18.7$ ,  $\gamma \sim 2.6$ , and  $a \sim 39''.4$ , meaning a core radius  $r_c \approx 33''$ . This composite profile is plotted in Fig. 11 (dashed line). It is clear that it provides a good fit to the entire profile, as opposed to our original one-component profile, which only fit the core.

In the very outer part of our measured profile, we noticed a turn-down at low significance – this may be evidence for a tidal cut-off. If so, it would be more suitable to fit a King profile (Eq. 2) as the second component. Doing so, we found that once again the core was well fit by our original EFF model, with the King component having  $k \sim 18.2$ ,  $r_t \sim 130''$ , and concentration  $c \sim 0.6$ , meaning a core radius  $r_c \approx 33''$ , which matches well the value from the two component EFF profile. The composite EFF-King profile is the solid line in Fig. 11. It is clear that it differs significantly from the two component EFF profile only in the very outer regions.

Fitting two-component models to our overall profile did not alter our original core radius measurement for R136, which suggests a degree of robustness to our result. There is considerable variation in the previously published values of this core radius. Meylan (1993) finds  $r_c = 1''.3$  from ground based data, while Elson et al. (1992) find  $r_c = 0''.5$  from *HST* observations. Malumuth & Heap (1994) obtain  $r_c = 0''.96$  from a mass-density profile based on *HST* data, and Hunter et al. (1995) find  $r_c < 0''.08$ , also using *HST* observations. Campbell et al. (1992) measure  $r_c = 0''.25$  based on a pure power-law surface brightness fit, again derived from *HST* observations. Our measured core radius of  $r_c = 1''.3$  is consistent with that of Meylan, but considerably larger than the other three. We reiterate however, that our measurement is an upper limit, due to the crowding in our images and also because our selected annulus widths mean that we are not equipped to measure core radii smaller than  $r_c \sim 1''.5$  accurately. Brandl et al. (1996) find considerable evidence for mass segregation in R136, and show that the derived core radius is therefore sensitive to the lower luminosity/mass cut-off for stars used in its calculation. For example, they find a core radius of  $r_c = 0''.48$  using stars with  $m > 15M_\odot$ , but increasing to  $r_c = 0''.97$  using stars with  $m > 4M_\odot$ . This may go some way towards explaining the above variations.

Similarly, there is some argument in the literature as to whether R136 might have undergone core collapse (see e.g., Campbell et al. (1992); Malumuth & Heap (1994)) – mostly the arguments are dependent on the core radius assumed for the cluster, and the relaxation time chosen to characterize the system. Campbell et al. calculate the relaxation time at the centre (their Eq. 2), and using their measured core radius (0.06 pc) and central density ( $5 \times 10^4 M_\odot \text{pc}^{-3}$ ) obtain an estimate of several  $\times 10^4$  yr – much shorter than the age of the cluster. They therefore suggest that R136 is likely in an advanced state of dynamical evolution and has undergone core collapse. In contrast, Malumuth & Heap derive a core radius four times larger, and a correspondingly larger central relaxation time – comparable to the age of the cluster. They also calculate the relaxation time at the median (half-mass) radius (their Eq. 5) and obtain a similar estimate, therefore concluding that R136 is probably mass-segregated but not post core collapse (according to Binney & Tremaine (1987) p527, core collapse occurs at 12 to 19

median relaxation times). Similarly, Brandl et al. (1996) show that dynamical mass segregation is likely to have occurred, at least for the most massive stars in the system, but that the median relaxation time is too long for core collapse to have taken place.

Even though our resolution is not quite sufficient to provide more than an upper limit for the core radius of R136, our surface brightness profile can help shed some light on the issue. If R136 is a PCC cluster then its profile should show a cusp similar to those observed for the old clusters discussed in Section 5.1.3. Both Campbell et al. (1992) and Brandl et al. (1996) show that the profile of R136 can be fit by a power law (although in the case of Brandl et al., this is only for stars with  $m > 40M_{\odot}$ ). We observe a small amount of evidence for such a power-law cusp and a break. The central region of the profile is plotted in Fig. 12, along with the best fitting power-law model and EFF model. We measure a slope  $\beta = 1.17$  with the break at  $r \sim 2'.6$ . This is only marginally consistent with the values of  $\beta$  measured for the old PCC candidates. From Fig. 12 it is also clear that the EFF profile fits equally well, unlike for the best old PCC candidates. It is likely then that in the case of R136 the apparent power-law structure in the central region of the profile is due to the brightest stars in the cluster residing in this space, consistent with the argument of Brandl et al. We can calculate the median relaxation time (in the form of Malumuth & Heap (1994), but see also e.g., Spitzer & Hart (1971); Spitzer (1987); Binney & Tremaine (1987); Meylan (1987)):

$$t_{rh} = \frac{6.5 \times 10^8}{\ln(0.4N)} \left( \frac{r_h^{3/2}}{m} \right) \left( \frac{M_{tot}}{10^5} \right)^{1/2} \text{ yr} \quad (7)$$

where  $N$  is the total number of stars and  $m$  is the typical stellar mass,  $M_{tot}$  is the total mass of the cluster and  $r_h$  is the median (or half mass) radius. Eq. 7 is essentially equivalent to Eq. 4.5 from Brandl et al. In the following Section (5.2) we derive estimates for the total masses of all the clusters studied in this paper. For R136 we obtain  $M_{tot} \sim 2.5 \times 10^4 M_{\odot}$ , and using this and Eq. 11 we can solve for the half-mass radius, obtaining  $r_h \sim 1.25$  pc. Both this radius and the total mass are entirely consistent with the values obtained by Brandl et al. ( $3 \times 10^4 M_{\odot}$  and 1.1 pc respectively). Following Brandl et al., we adopt  $m \sim 0.5M_{\odot}$  and therefore estimate  $N \sim 5 \times 10^4$ . Substituting these values into Eq. 7 provides us with  $t_{rh} \sim 2.1 \times 10^8$  yr, very similar to the estimate of Brandl et al. ( $t_{rh} \sim 2.5 \times 10^8$  yr). For the most massive stars (i.e.,  $m \sim 40M_{\odot}$ ) we obtain  $t_{rh} \sim 2.1 \times 10^6$  yr, which is comparable to the age of the cluster. This suggests that for these stars, dynamical mass segregation has indeed had time to occur, but both calculated values of  $t_{rh}$  argue strongly against core collapse having happened. In confirmation of this, we can estimate the central relaxation time (in the form of Campbell et al. (1992), but see also e.g., Spitzer (1987); Binney & Tremaine (1987); Meylan (1987)):

$$t_{r0} \approx 3 \times 10^4 \left( \frac{10M_{\odot}}{m} \right) \left( \frac{r_c}{0.06\text{pc}} \right)^3 \times \left( \frac{\rho_0}{5 \times 10^4 M_{\odot}\text{pc}^{-3}} \right)^{1/2} \left( \frac{1.4}{\ln(0.4N)} \right) \text{ yr} \quad (8)$$

where  $r_c$  is the core radius and  $\rho_0$  the central mass density. In the following Section (5.2) we also estimate the central mass densities for all the clusters studied in this paper. Using our derived value of  $\rho_0 \sim 3 \times 10^4 M_{\odot}\text{pc}^{-3}$  for R136, and our upper limit for the core radius of  $r_c \sim 0.32$  pc, we obtain  $t_{r0} \sim 1 \times 10^7$  yr for  $m \sim 0.5M_{\odot}$ , again considerably longer than the estimated age of the cluster. Given that  $t_{r0} \propto r_c^3$ , the true core radius would have to

be at least five times smaller than our upper limit in order to bring the central relaxation timescale down to the size required to make R136 dynamically old enough to be in the epoch of core collapse ( $t_{r0} \sim 1 \times 10^5$  yr).

## 5.2 Luminosity and mass estimates

We can use our measured structural parameters to obtain luminosity and mass estimates for each cluster. Eq. 3 must first be deprojected, which is done by means of an Abel integral equation (EFF87; see also Binney & Tremaine (1987), Section 4.2 and Appendix 1.B.4) for the luminosity density  $j(r)$  of the cluster in question. We obtain:

$$j(r) = j_0 \left( 1 + \frac{r^2}{a^2} \right)^{-\frac{(\gamma+1)}{2}} \quad (9)$$

which has the same functional form as the surface brightness profile  $\mu(r)$  but with index  $\gamma + 1$ . In Eq. 9,  $j_0$  represents the central luminosity density and is given by

$$j_0 = \frac{\mu_0 \Gamma\left(\frac{\gamma+1}{2}\right)}{a\sqrt{\pi} \Gamma\left(\frac{\gamma}{2}\right)} \quad (10)$$

where  $\Gamma$  is a standard gamma function. To obtain the measured enclosed luminosity  $L$  as a function of radius, we integrate Eq. 9 within a cylinder of radius  $r$  along the line of sight, since this is the relevant observational quantity. This gives:

$$L(r) = 4\pi j_0 \int_0^{\infty} \int_0^r \ell \left( 1 + \frac{x^2 + \ell^2}{a^2} \right)^{-\frac{(\gamma+1)}{2}} d\ell dx \quad (11)$$

where  $\ell$  is the radial variable and  $x$  the line-of-sight variable. Evaluating the integral for  $r = r_m$ , the maximum radial extent of the measured surface brightness profile, gives:

$$L_m = \frac{2\pi\mu_0}{\gamma-2} \left( a^2 - a^{\gamma} (a^2 + r_m^2)^{-\frac{(\gamma-2)}{2}} \right) \quad (12)$$

By taking the limit  $r_m \rightarrow \infty$ , we can also obtain an estimate for the asymptotic cluster luminosity  $L_{\infty}$ :

$$L_{\infty} = \frac{2\pi\mu_0 a^2}{\gamma-2} \quad (13)$$

provided  $\gamma > 2$ , otherwise the limit is divergent.

The calculated values for  $j_0$ ,  $L_{\infty}$  and  $L_m$  are listed in Table 6. When calculating  $L_m$  we take  $r_m$  from Table 4. In order to use Eq. 10, 12 and 13, we must have  $\mu_0$ ,  $a$  and  $r_m$  in physical units. As always, to convert to parsecs we take the LMC distance modulus to be  $DM = 18.5$ , which implies a scale of  $4.116 \text{ arcsec pc}^{-1}$ . This takes care of  $a$  and  $r_m$ , but to convert  $\mu_0$  to  $L_{\odot}\text{pc}^{-2}$  is more complicated. We first need to know the  $V_{555}$  magnitude of the sun. We assume an absolute standard magnitude of  $V = +4.82$  and a standard colour  $B - V = +0.65$  and combine Eq. 7 and 8 from Holtzman et al. (1995b):

$$\text{WFPC2} = \text{SMAG} - T_{1,FS} \times \text{SCOL} - T_{2,FS} \times \text{SCOL}^2 + Z_{FG} - Z_{FS} \quad (14)$$

where the notation is as in Holtzman et al. (1995b). Using our assumed standard solar magnitude and colour,  $Z_{FG}$  from Table 6 of Holtzman et al., and  $T_{1,FS}$ ,  $T_{2,FS}$  and  $Z_{FS}$  from Table 7 of Holtzman et al., we obtain  $V_{555}^{\odot} = +4.85$ . Alternatively, using Eq. 11 and 12 from Dolphin (2000b) provides an identical result. The central surface brightness for each cluster must be corrected for absorption, and we use  $E(B - V) = 0.10$ , which is a reasonable average



in the direction of the LMC (cf. EFF87). R136 however, has significantly higher reddening, with  $E(B - V) = 0.38$  (Hunter et al. 1995). Armed with these numbers, we use the relation

$$\log \mu_0 = 0.4(V_{555}^{\odot} - \mu_{555}(0) + DM + 3.1E(B - V)) + \log(4.116^2) L_{\odot} \text{ pc}^{-2} \quad (15)$$

to convert  $\mu_0$  to physical units.

We calculate mass and density estimates for each cluster by multiplying the appropriate luminosity equations by the average mass to light ratio  $M/L_V$  for the cluster in question. The density  $\rho(r)$  then corresponds to Eq. 9, with the central density  $\rho_0$  obtained from Eq. 10. Similarly, the mass  $M_m$  inside  $r_m$  is given by Eq. 12 multiplied by  $M/L_V$  and the asymptotic mass  $M_{\infty}$  is given by Eq. 13 times this ratio.

To estimate  $M/L_V$  for each cluster, we use the evolutionary synthesis code of Fioc & Rocca-Volmerange (1997) (PEGASE v2.0, 1999). This code determines the integrated properties of a synthetic stellar population as a function of time, using libraries of isochrones and stellar spectra to make the detailed calculations, and accounting for factors such as the IMF of the system, a range of metallicities, and any ongoing star-formation. We proceed using the simplest possible model – a population of stars formed simultaneously in one initial burst and with the same metallicity – presumably a fairly good approximation to the formation of a rich stellar cluster. For the initial burst, we assume the IMF of Kroupa, Tout & Gilmore (1993) over the mass range 0.1 to  $120M_{\odot}$ . There are four available initial abundances which cover the metallicity range of the cluster sample –  $Z = 0.0001$  ( $[\text{Fe}/\text{H}] \approx -2.25$ );  $Z = 0.0004$  ( $[\text{Fe}/\text{H}] \approx -1.65$ );  $Z = 0.004$  ( $[\text{Fe}/\text{H}] \approx -0.64$ ); and  $Z = 0.008$  ( $[\text{Fe}/\text{H}] \approx -0.33$ ). The  $M/L_V$  values for each metallicity are plotted as a function of cluster age in Fig. 13. Although the mass-to-light ratios obtained from these models are purely theoretical, they do agree well with observations (see e.g., Parmentier & Gilmore (2001)). From Fig. 13, it is clear that for most of the evolution, the  $M/L_V$  ratio is relatively insensitive to the chosen abundance. For completeness, we adopt the metallicity for each cluster based on the estimates in Table 2. Because of the insensitivity of the calculation to the selected abundance, we are confident in using even those abundances which were calculated as averages rather than being taken directly from the literature – it is sufficient to be able to differentiate between “metal poor” ( $[\text{Fe}/\text{H}] \approx -2.25$ ) and “metal rich” ( $[\text{Fe}/\text{H}] \approx -0.33$ ). We then use the age estimates from Table 2 to obtain a mass to light ratio from the appropriate evolutionary synthesis model. The adopted abundances, and values for  $M/L_V$ ,  $\rho_0$ ,  $M_{\infty}$  and  $M_m$  are listed in Table 6.

The values of  $L_{\infty}$  and  $M_{\infty}$  are intended to provide reasonable estimates of total cluster luminosities and masses in the absence of tidal limit information. There is very little difference in the result obtained from using Eq. 12 with  $r_m$  several hundred arcseconds (a reasonable tidal cut-off), and the result obtained from Eq. 13. We provide estimates of  $L_m$  and  $M_m$  to show the luminosity and mass over the radial range we actually measure, and as such, these provide reliable lower limits for total cluster luminosities and masses. For most clusters there is not a great difference between these values and the asymptotic values; however, for clusters with  $\gamma \approx 2$ , the value of  $L_{\infty}$  (and  $M_{\infty}$ ) can become unreasonably large (e.g. NGC 1856), and the extrapolation  $r \rightarrow \infty$  may not be justified.

The presence of saturated stars on some images, and the imposition of brightness limits on others (see Sections 4.2.3 and 4.2.4) causes some luminosity (and mass) to be unaccounted for in several surface brightness profiles (that is, the zero-point  $\mu_{555}(0)$  is

fainter than would be expected were the brightest stars included in the profiles). However, this effect is not particularly significant. It is most pronounced in the youngest clusters, where bright stars are relatively massive. At worst we miss  $\sim 30$  stars from any young cluster, which results in  $\lesssim 600M_{\odot}$  being neglected. Addition of this missing mass gives totals still within the quoted uncertainties for such clusters. The errors listed in Table 6 represent the uncertainties in the calculated parameters due to the random errors in the values of  $\mu_0$ ,  $\gamma$  and  $a$ . We do not account for any systematic errors such as those introduced by any saturated stars or those which might be present in the calculated values for  $M/L_V$ .

## 6 THE CORE RADIUS VS. AGE RELATIONSHIP

With a large sample such as this, there is the opportunity for a full statistical analysis of the parameters presented in Tables 2, 4 and 6, in search of correlations and physical insight into the overall properties of the LMC cluster system. Such an analysis is beyond the scope of the present paper and will be presented in the future. We do however observe one particularly noteworthy trend.

When core radius is plotted against age for all clusters in the sample (Fig. 14), a clear relationship exists between these two parameters – namely that the spread in core radius increases significantly with increasing cluster age. Without exception, all of the young clusters have compact cores with  $r_c \lesssim 2.5$  pc, while for clusters older than  $\log \tau \sim 9$  the full range  $r_c \approx 0 - 8$  pc is covered. This trend has previously been discovered and discussed by Elson et al. (1989), E91 and Elson (1992), using a combination of literature data and ground-based measurements.

The key question is whether this observed relationship is indicative of true structural evolution in LMC clusters as they grow older, or is merely the result of a secondary correlation, a product of the reduction process or a selection effect (i.e., we systematically missed all the young, low surface brightness clusters from our sample). The fact that we confirm exactly the result of Elson, using a larger (and distinct) sample, space-based observations, and uniformly selected and reduced data is argument against the relationship being a reduction artifact, or due to a selection effect. In addition, we did not choose our young clusters in a systematic fashion, but rather simply used all those available in the *HST* archive – in effect, a random sample. This adds weight to the argument against a selection effect being responsible for the observed upper envelope; however we cannot guarantee that there are not very low surface brightness young clusters with large cores in the LMC system. It is likely however, that such diffuse clusters would not remain bound for long, and so their presence (or otherwise) does not affect the discussion and conclusions below.

Given that the radius-age relationship does not seem to be the product of data reduction or a selection effect, E91 discusses the possibility that a correlation between mass and core radius and between mass and age might be responsible – that is, if both more massive clusters (with larger cores) and less massive clusters (with smaller cores) were formed in the past, but only less massive clusters (with smaller cores) formed recently, it might seem that core radius evolves with age. However, Elson observed no such correlations in her sample of 10 young clusters.

Similarly, we plot  $M_{\infty}$  against age, and  $M_{\infty}$  against  $r_c$  for our (much larger) sample, to look for correlations. These plots are Fig. 15 and Fig. 16 respectively. While  $M_{\infty}$  is not always a reliable extrapolation to the true mass of a cluster, we use it here as a convenient parameter for eliminating the age bias in  $L_m$  and  $L_{\infty}$

**Table 6.** Luminosity and mass estimates calculated using the structural parameters from the best fitting EFF profiles.

Cluster	$\log \mu_0^a$ ( $L_\odot \text{ pc}^{-2}$ )	Adopted [Fe/H]	Adopted $M/L_V$	$\log j_0$ ( $L_\odot \text{ pc}^{-3}$ )	$\log L_\infty$ ( $L_\odot$ )	$\log L_m$ ( $L_\odot$ )	$\log \rho_0$ ( $M_\odot \text{ pc}^{-3}$ )	$\log M_\infty$ ( $M_\odot$ )	$\log M_m$ ( $M_\odot$ )
NGC1466	$3.06 \pm 0.02$	-2.25	2.80	$2.33 \pm 0.05$	$4.86 \pm 0.11$	$4.80 \pm 0.09$	$2.78 \pm 0.05$	$5.31 \pm 0.11$	$5.25 \pm 0.09$
NGC1651	$2.54 \pm 0.02$	-0.33	1.14	$1.68^{+0.07}_{-0.06}$	$5.19^{+0.45}_{-0.28}$	$4.64^{+0.10}_{-0.11}$	$1.74^{+0.07}_{-0.06}$	$5.24^{+0.45}_{-0.28}$	$4.70^{+0.10}_{-0.11}$
NGC1711	$3.38 \pm 0.02$	-0.64	0.12	$2.74^{+0.07}_{-0.06}$	$5.14 \pm 0.16$	$5.02^{+0.11}_{-0.12}$	$1.82^{+0.07}_{-0.06}$	$4.21 \pm 0.16$	$4.10^{+0.11}_{-0.12}$
NGC1718	$3.02 \pm 0.03$	-0.33	1.14	$2.40^{+0.26}_{-0.07}$	$5.04^{+0.26}_{-0.22}$	$4.72 \pm 0.13$	$2.46^{+0.08}_{-0.07}$	$5.10^{+0.26}_{-0.22}$	$4.78 \pm 0.13$
NGC1754	$3.70 \pm 0.10$	-1.65	3.36	$3.45^{+0.19}_{-0.18}$	$4.87^{+0.33}_{-0.34}$	$4.72^{+0.26}_{-0.28}$	$3.98^{+0.19}_{-0.18}$	$5.39^{+0.33}_{-0.34}$	$5.25^{+0.26}_{-0.28}$
NGC1777	$2.69 \pm 0.01$	-0.33	0.67	$1.85 \pm 0.04$	$4.92^{+0.13}_{-0.12}$	$4.70^{+0.07}_{-0.08}$	$1.68 \pm 0.04$	$4.75^{+0.13}_{-0.12}$	$4.53^{+0.07}_{-0.08}$
NGC1786	$3.71 \pm 0.04$	-1.65	3.29	$3.28 \pm 0.10$	$5.05 \pm 0.20$	$4.98^{+0.16}_{-0.17}$	$3.79 \pm 0.10$	$5.57 \pm 0.20$	$5.50^{+0.16}_{-0.17}$
NGC1805	$3.49 \pm 0.02$	-0.33	0.05	$3.06 \pm 0.06$	$4.82 \pm 0.13$	$4.75^{+0.10}_{-0.11}$	$1.75 \pm 0.06$	$3.52 \pm 0.13$	$3.45^{+0.10}_{-0.11}$
NGC1818	$3.35 \pm 0.02$	-0.33	0.08	$2.65 \pm 0.06$	$5.23^{+0.15}_{-0.14}$	$5.11 \pm 0.10$	$1.55 \pm 0.06$	$4.13^{+0.15}_{-0.14}$	$4.01 \pm 0.10$
NGC1831	$3.06 \pm 0.02$	-0.33	0.32	$2.10 \pm 0.06$	$5.30 \pm 0.13$	$5.21^{+0.09}_{-0.10}$	$1.60 \pm 0.06$	$4.81 \pm 0.13$	$4.71^{+0.09}_{-0.10}$
NGC1835	$4.14 \pm 0.03$	-1.65	3.56	$3.77 \pm 0.07$	$5.27 \pm 0.13$	$5.24 \pm 0.12$	$4.32 \pm 0.07$	$5.83 \pm 0.13$	$5.79 \pm 0.12$
NGC1841	$2.06 \pm 0.01$	-2.25	2.75	$0.85 \pm 0.08$	$4.68^{+0.21}_{-0.19}$	$4.57^{+0.12}_{-0.14}$	$1.29 \pm 0.08$	$5.12^{+0.21}_{-0.19}$	$5.00^{+0.12}_{-0.14}$
NGC1847	$3.28 \pm 0.02$	-0.33	0.09	$2.66 \pm 0.06$	$6.01^{+0.48}_{-0.63}$	$4.91^{+0.09}_{-0.10}$	$1.62 \pm 0.06$	$4.97^{+0.48}_{-0.63}$	$3.86^{+0.09}_{-0.10}$
NGC1850	$4.01 \pm 0.03$	-0.33	0.10	$3.30 \pm 0.08$	$6.42^{+0.52}_{-0.32}$	$5.87^{+0.13}_{-0.14}$	$2.30 \pm 0.08$	$5.42^{+0.52}_{-0.32}$	$4.87^{+0.13}_{-0.14}$
NGC1856	$4.02 \pm 0.03$	-0.64	0.18	$3.50 \pm 0.06$	$7.26^{+0.69}_{-0.87}$	$5.63^{+0.10}_{-0.11}$	$2.76 \pm 0.06$	$6.51^{+0.69}_{-0.87}$	$4.89^{+0.10}_{-0.11}$
NGC1860	$2.80 \pm 0.04$	-0.64	0.22	$2.16 \pm 0.08$	$4.95^{+0.41}_{-0.27}$	$4.55^{+0.12}_{-0.13}$	$1.50 \pm 0.08$	$4.30^{+0.41}_{-0.27}$	$3.90^{+0.12}_{-0.13}$
NGC1866	$3.28 \pm 0.01$	-0.64	0.18	$2.44 \pm 0.03$	$5.38 \pm 0.08$	$5.26 \pm 0.06$	$1.69 \pm 0.03$	$4.63 \pm 0.08$	$4.52 \pm 0.06$
NGC1868	$3.50 \pm 0.02$	-0.64	0.40	$2.97 \pm 0.04$	$4.93 \pm 0.10$	$4.89 \pm 0.09$	$2.58 \pm 0.04$	$4.53 \pm 0.10$	$4.49 \pm 0.09$
NGC1898	$3.07 \pm 0.02$	-1.65	3.13	$2.46^{+0.09}_{-0.08}$	$5.38^{+0.19}_{-0.42}$	$4.80^{+0.15}_{-0.16}$	$2.96^{+0.09}_{-0.08}$	$5.88^{+0.19}_{-0.42}$	$5.29^{+0.15}_{-0.16}$
NGC1916	$4.32 \pm 0.04$	-2.25	3.37	$4.10 \pm 0.07$	$5.27^{+0.15}_{-0.14}$	$5.21^{+0.12}_{-0.13}$	$4.63 \pm 0.07$	$5.79^{+0.15}_{-0.14}$	$5.73^{+0.12}_{-0.13}$
NGC1984	$3.24 \pm 0.04$	-0.64	0.05	$2.94 \pm 0.10$	$4.68^{+0.35}_{-0.28}$	$4.40^{+0.16}_{-0.17}$	$1.64 \pm 0.10$	$3.38^{+0.35}_{-0.28}$	$3.10^{+0.16}_{-0.17}$
NGC2004	$3.92 \pm 0.03$	-0.64	0.08	$3.42^{+0.10}_{-0.09}$	$5.52^{+0.24}_{-0.23}$	$5.37^{+0.16}_{-0.17}$	$2.32^{+0.10}_{-0.09}$	$4.43^{+0.24}_{-0.23}$	$4.27^{+0.16}_{-0.17}$
NGC2005	$3.88 \pm 0.05$	-1.65	3.56	$3.62 \pm 0.12$	$4.94^{+0.27}_{-0.26}$	$4.85^{+0.21}_{-0.22}$	$4.17 \pm 0.12$	$5.49^{+0.27}_{-0.26}$	$5.40^{+0.21}_{-0.22}$
NGC2011	$3.12 \pm 0.06$	-0.33	0.05	$2.75 \pm 0.12$	$4.77^{+0.38}_{-0.32}$	$4.42^{+0.19}_{-0.20}$	$1.45 \pm 0.12$	$3.47^{+0.38}_{-0.32}$	$3.12^{+0.19}_{-0.20}$
NGC2019	$4.00 \pm 0.04$	-1.65	3.80	$3.75 \pm 0.09$	$5.10^{+0.20}_{-0.19}$	$4.99 \pm 0.15$	$4.33 \pm 0.09$	$5.68^{+0.20}_{-0.19}$	$5.57 \pm 0.15$
NGC2031	$3.12 \pm 0.02$	-0.64	0.20	$2.40 \pm 0.08$	$5.83^{+0.24}_{-0.45}$	$5.03^{+0.12}_{-0.13}$	$1.70 \pm 0.08$	$5.13^{+0.24}_{-0.45}$	$4.33^{+0.12}_{-0.13}$
NGC2100	$4.19 \pm 0.06$	-0.33	0.07	$3.80^{+0.13}_{-0.12}$	$5.63^{+0.33}_{-0.30}$	$5.46^{+0.22}_{-0.23}$	$2.64^{+0.13}_{-0.12}$	$4.48^{+0.33}_{-0.30}$	$4.31^{+0.22}_{-0.23}$
NGC2121	$2.33 \pm 0.01$	-0.64	1.33	$1.15 \pm 0.09$	$5.56^{+0.22}_{-0.44}$	$4.86^{+0.11}_{-0.13}$	$1.27 \pm 0.09$	$5.69^{+0.22}_{-0.44}$	$4.99^{+0.11}_{-0.13}$
NGC2136	$3.74 \pm 0.04$	-0.64	0.16	$3.13 \pm 0.09$	$5.24 \pm 0.17$	$5.22 \pm 0.16$	$2.33 \pm 0.09$	$4.45 \pm 0.17$	$4.42 \pm 0.16$
NGC2153	$3.02 \pm 0.04$	-0.33	0.69	$2.74^{+0.14}_{-0.13}$	$4.13^{+0.35}_{-0.32}$	$4.04^{+0.26}_{-0.28}$	$2.58^{+0.14}_{-0.13}$	$3.97^{+0.35}_{-0.32}$	$3.88^{+0.26}_{-0.28}$
NGC2155	$2.52 \pm 0.02$	-0.64	1.33	$1.61 \pm 0.09$	$4.77^{+0.26}_{-0.23}$	$4.61^{+0.15}_{-0.16}$	$1.74 \pm 0.09$	$4.90^{+0.26}_{-0.23}$	$4.73^{+0.15}_{-0.16}$
NGC2156	$3.10 \pm 0.03$	-0.33	0.11	$2.59^{+0.07}_{-0.06}$	$4.59^{+0.14}_{-0.13}$	$4.51^{+0.10}_{-0.11}$	$1.63^{+0.07}_{-0.06}$	$3.63^{+0.14}_{-0.13}$	$3.55^{+0.10}_{-0.11}$
NGC2157	$3.58 \pm 0.02$	-0.33	0.11	$2.90 \pm 0.06$	$5.27 \pm 0.13$	$5.23 \pm 0.11$	$1.94 \pm 0.06$	$4.31 \pm 0.13$	$4.27 \pm 0.11$
NGC2159	$2.83 \pm 0.02$	-0.33	0.11	$2.14^{+0.07}_{-0.06}$	$4.61 \pm 0.15$	$4.52 \pm 0.12$	$1.18^{+0.07}_{-0.06}$	$3.65 \pm 0.15$	$3.56 \pm 0.12$
NGC2162	$2.72 \pm 0.03$	-0.33	0.69	$2.02 \pm 0.10$	$4.56^{+0.25}_{-0.23}$	$4.46^{+0.17}_{-0.18}$	$1.86 \pm 0.10$	$4.40^{+0.25}_{-0.23}$	$4.30^{+0.17}_{-0.18}$
NGC2164	$3.40 \pm 0.02$	-0.33	0.13	$2.81 \pm 0.04$	$5.01 \pm 0.09$	$4.93 \pm 0.07$	$1.93 \pm 0.04$	$4.12 \pm 0.09$	$4.04 \pm 0.07$
NGC2172	$2.61 \pm 0.03$	-0.33	0.11	$1.88 \pm 0.07$	$4.48^{+0.16}_{-0.15}$	$4.39^{+0.12}_{-0.13}$	$0.92 \pm 0.07$	$3.52^{+0.16}_{-0.15}$	$3.43^{+0.12}_{-0.13}$
NGC2173	$2.75 \pm 0.02$	-0.33	1.19	$1.99 \pm 0.08$	$4.99^{+0.35}_{-0.27}$	$4.67^{+0.14}_{-0.15}$	$2.06 \pm 0.08$	$5.06^{+0.35}_{-0.27}$	$4.75^{+0.14}_{-0.15}$
NGC2193	$2.78 \pm 0.03$	-0.64	1.00	$2.27^{+0.09}_{-0.08}$	$4.42^{+0.22}_{-0.20}$	$4.25 \pm 0.14$	$2.27^{+0.09}_{-0.08}$	$4.42^{+0.22}_{-0.20}$	$4.25 \pm 0.14$
NGC2209	$1.86 \pm 0.02$	-0.33	0.61	$0.82 \pm 0.09$	$5.25^{+0.36}_{-0.60}$	$4.22^{+0.11}_{-0.13}$	$0.60 \pm 0.09$	$5.03^{+0.36}_{-0.60}$	$4.01^{+0.11}_{-0.13}$
NGC2210	$3.42 \pm 0.02$	-2.25	3.37	$2.81 \pm 0.05$	$4.95 \pm 0.10$	$4.92^{+0.08}_{-0.09}$	$3.34 \pm 0.05$	$5.48 \pm 0.10$	$5.45^{+0.08}_{-0.09}$
NGC2213	$3.03 \pm 0.02$	-0.33	0.87	$2.46 \pm 0.06$	$4.62 \pm 0.15$	$4.54^{+0.11}_{-0.12}$	$2.40 \pm 0.06$	$4.56 \pm 0.15$	$4.48^{+0.11}_{-0.12}$
NGC2214	$3.35 \pm 0.03$	-0.33	0.11	$2.71 \pm 0.09$	$5.46^{+0.45}_{-0.31}$	$5.09^{+0.16}_{-0.17}$	$1.76 \pm 0.09$	$4.50^{+0.45}_{-0.31}$	$4.13^{+0.16}_{-0.17}$
NGC2231	$2.50 \pm 0.05$	-0.64	0.69	$1.77^{+0.20}_{-0.18}$	$5.34^{+0.43}_{-0.96}$	$4.44^{+0.29}_{-0.35}$	$1.60^{+0.20}_{-0.18}$	$5.18^{+0.43}_{-0.96}$	$4.28^{+0.29}_{-0.35}$
NGC2249	$3.07 \pm 0.02$	-0.33	0.48	$2.44 \pm 0.06$	$4.66 \pm 0.13$	$4.63 \pm 0.12$	$2.12 \pm 0.06$	$4.35 \pm 0.13$	$4.31 \pm 0.12$
NGC2257	$2.32 \pm 0.01$	-1.65	3.43	$1.19 \pm 0.06$	$4.88 \pm 0.15$	$4.72^{+0.09}_{-0.10}$	$1.73 \pm 0.06$	$5.41 \pm 0.15$	$5.26^{+0.09}_{-0.10}$
SL663	$1.73 \pm 0.02$	-0.64	1.33	$0.60 \pm 0.07$	$5.11^{+0.24}_{-0.42}$	$4.21^{+0.09}_{-0.10}$	$0.73 \pm 0.07$	$5.23^{+0.24}_{-0.42}$	$4.33^{+0.09}_{-0.10}$
SL842	$2.26 \pm 0.04$	-0.33	1.14	$1.55 \pm 0.12$	$4.02^{+0.35}_{-0.34}$	$3.97^{+0.20}_{-0.21}$	$1.61 \pm 0.12$	$4.08^{+0.35}_{-0.34}$	$4.02^{+0.20}_{-0.21}$
SL855	$1.52 \pm 0.01$	-0.33	0.70	$0.49^{+0.10}_{-0.09}$	$4.74^{+0.34}_{-0.59}$	$3.88^{+0.13}_{-0.15}$	$0.33^{+0.10}_{-0.09}$	$4.58^{+0.34}_{-0.59}$	$3.72^{+0.13}_{-0.15}$
HODGE4	$2.46 \pm 0.02$	-0.33	1.21	$1.59 \pm 0.09$	$5.31^{+0.22}_{-0.45}$	$4.59^{+0.13}_{-0.14}$	$1.67 \pm 0.09$	$5.39^{+0.22}_{-0.45}$	$4.67^{+0.13}_{-0.14}$
HODGE11	$2.85 \pm 0.02$	-2.25	3.25	$2.08 \pm 0.07$	$5.11^{+0.26}_{-0.22}$	$4.79^{+0.11}_{-0.12}$	$2.59 \pm 0.07$	$5.63^{+0.26}_{-0.22}$	$5.31^{+0.11}_{-0.12}$
HODGE14	$2.58 \pm 0.04$	-0.64	0.88	$2.02 \pm 0.10$	$4.38^{+0.34}_{-0.28}$	$4.16^{+0.18}_{-0.19}$	$1.96 \pm 0.10$	$4.33^{+0.34}_{-0.28}$	$4.10^{+0.18}_{-0.19}$
R136 <sup>b</sup>	$5.98 \pm 0.04^c$	-0.33	0.02	$6.17 \pm 0.08$	$6.25^{+0.21}_{-0.19}$	$6.01 \pm 0.13$	$4.47 \pm 0.08$	$4.55^{+0.21}_{-0.19}$	$4.31 \pm 0.13$

<sup>a</sup> Corrected for reddening using  $E(B - V) = 0.10$ .<sup>b</sup> Luminosity and mass calculated using the structural parameters derived for the inner regions only – that is, those parameters listed in Table 4. Given the break to a shallower profile at  $r \sim 15''$ , we likely under-estimate  $L_\infty$  and  $M_\infty$  – the asymptotic luminosity and mass including NGC 2070.<sup>c</sup> Corrected for reddening using  $E(B - V) = 0.38$  (see text).

(i.e., young clusters are intrinsically more luminous than old clusters), as well as any observational bias present in  $M_m$  (i.e., a cluster with  $\gamma \sim 2$  will have more mass at large radii, where we did not observe, than a cluster with  $\gamma \sim 4$ , and consequently will likely have a correspondingly small  $M_m$ ). In Fig. 15, we see no significant correlation of mass with age. It is true that there are a few young clusters with low masses, and that all the old clusters seem to have larger masses; however we attribute this to the fact that the low-mass young clusters will have faded and probably dispersed by age  $10^{10}$  yr – explaining why there are no low-mass old clusters (a detailed discussion of this effect is presented in Meylan (1993)). There is no evidence for any significant intrinsic difference between the masses of the largest newly formed clusters and the old clusters in the sample. In Fig. 16 we also see no evidence for a strong correlation. While it is true that those clusters with large core radii all seem to be relatively massive, they are not more massive than most of the clusters with smaller core radii.

We therefore conclude, like Elson, that the trend observed in Fig. 14 represents real evolution in the structure of clusters as they grow older. Given this, it is useful to return to Fig. 14 and examine closely the distribution of clusters, which seems to exhibit a bifurcation at around several  $\times 10^8$  yr. This bifurcation grows into a large separation by 10 Gyr. It is possible that the apparent dearth of older clusters with core radii in the range 3 – 6 pc could be a small-sample effect. A simple Kolmogorov-Smirnov test on the distribution of core radii for all clusters older than 10 Gyr, shows that they are not drawn from a uniform distribution, at about the 99 per cent level. If we increase the sample size by including all clusters older than 1 Gyr, the significance increases to better than 99.5 per cent. The bifurcation is therefore statistically significant.

The lower branch in the radius-age diagram represents the standard picture of (isolated) cluster evolution, where a newly formed cluster suffers significant and rapid mass-loss due to stellar evolution, causing the cluster to expand. The rate of expansion is regulated by the initial mass spectrum present in the cluster (i.e., the slope of the mass function) (see e.g., Chernoff & Weinberg (1990)). The more heavily weighted the high mass end of a cluster's mass function is, the more severe the early mass loss. As the cluster grows older and evolves, the expansion slows and is eventually reversed by core collapse. E91 present Fokker-Planck models of evolving clusters with different IMF slopes, plotted over the equivalent of Fig. 14. Clusters with IMF slopes similar to that for the Salpeter IMF ( $x = 1.35$ , where the IMF is given by  $\Phi \propto m^{-(1+x)}$ ) and steeper follow tracks which match well the shape of the lower branch in Fig. 14.

There is a noticeable scatter about this sequence, but its cause is not clear. Because the IMF slope governs the rate of expansion, IMF variations could be responsible. However, more and more evidence is pointing towards the universality of the IMF – Gilmore (2001) provides a detailed review, and more recently de Grijs et al. (2002c) have shown that a sample of six LMC clusters (widely scattered on Fig. 14) must have had very similar IMFs. It therefore seems likely that a combination of other factors is instead responsible. Even the youngest clusters in the present sample have a spread in core radii – this probably reflects the different formation conditions of each cluster (E91), as well as the spread in initial mass (Fig. 15). Variations in initial mass would cause a spread in the lower sequence – it may be that this alone could reproduce the required scatter. A second possibility is that the scatter is a result of the cluster sample being spread over a considerable range of distances from the LMC centre (Table 2). Gilmore (2001) shows that tidal forces are at least as significant in the comparative evolution

of Galactic globular clusters as IMF variations between clusters. The spread in the lower sequence of Fig. 14 might simply reflect the spread in orbital radii between clusters. We are currently employing  $N$ -body simulations to explore these two mechanisms in detail, to measure their relative effects, and to see whether either (or a combination of both) is able to reproduce the lower region of Fig. 14 for a suitable cluster sample.

The fact that the models of isolated evolving clusters presented by E91 match the lower sequence of Fig. 14 so well adds plausibility to our argument that the radius-age plot tracks the physical evolution of LMC clusters. This renders the clusters which follow the upper branch especially intriguing. What makes these clusters different – why do they diverge from the standard sequence beyond a few  $\times 10^8$  yr, to finish in the upper right of the plot? Possibly, these clusters are on the verge of dissolution – after a certain time, mass loss can be so significant that rather than undergoing core collapse, a cluster simply dissipates. However, the upper sequence covers the timescale  $10^8$  to  $10^{10}$  yr, which is far too long for dissolution. In addition, Fig. 16 shows that clusters with large core radii are all relatively massive, whereas one would expect a cluster dissolving due to mass loss to be less massive. Upper sequence clusters are therefore probably not undergoing dissolution, but are expanding for another reason. Given this, we suggest two ways in which upper sequence clusters might be distinguished from the “standard” clusters – either they have (or have had) radically different stellar populations, or they have been influenced by some external process (i.e., they are not isolated).

Examples falling into the first category include very flat IMF slopes, and very large binary star fractions. It seems unlikely that either could cause the degree of core expansion observed. As discussed previously, the IMF slope for a cluster regulates its early expansion, but the rapid expansion phase does not last the entire lifetime of the cluster (as would be required for the cluster to evolve along the upper sequence). In addition, as shown by E91, a cluster with a very flat IMF suffers such extreme early mass loss that it becomes unbound after only a very short time ( $\sim 10^7$  yrs). Our earlier argument with respect to the universality of the IMF also holds here. Similarly, although the binary star fraction in a cluster is important in the context of halting core collapse, binary stars alone cannot drive the large scale core expansion we have observed. To extract energy from a cluster's binary stars requires close stellar encounters, and an expanding core radius implies lower stellar density and therefore fewer encounters in a given period. It is unlikely therefore that significant cluster expansion can be driven by binary stars over the required timescale, even given an exceptional binary fraction.

Two examples which fall into the second category are the merger of double clusters and the effects of strongly variable, perturbative tidal fields. Again, from simple physical arguments, it is difficult to see how either mechanism could produce the scale of core expansion which is observed without destroying the clusters in question. Double cluster pairs are relatively common in the LMC (Bhatia et al. 1991; de Oliveira et al. 1998; de Oliveira et al. 2000), and Bhatia & Hatzidimitriou (1988) have shown that it is statistically unlikely that they are *all* coincidental alignments – hence some are likely gravitationally bound and interacting. An interacting pair will merge after a relatively brief period (Bhatia 1990), and  $N$ -body studies by de Oliveira et al. (1998; 2000) have shown that a binary cluster merger can result in a single cluster with a structure which is stable after  $\sim 200$  Myr and distinct from the structure of the original clusters. However, it is unclear whether large scale core expansion is a result – small scale expansion implies many

mergers would be required, and this is statistically very unlikely. In the case of tidal forces, it is uncertain as to what effects a tidal field can have on a cluster core. Tidal forces increase as the cube of the distance from the centre of a cluster and therefore affect mainly the outer parts. A tidal force strong enough to significantly alter a cluster's core would probably destroy the cluster. However, as with the merger of double clusters, no models have been explored in the context of core expansion, and so neither mechanism can yet be quantitatively eliminated. We are currently carrying out detailed  $N$ -body simulations (e.g., Wilkinson et al., in prep.) to explore this further.

## 7 SUMMARY AND CONCLUSIONS

We have compiled a pseudo-snapshot data set of two-colour observations from the *HST* archive for a sample of 53 rich LMC clusters spanning the full age range  $10^6$  to  $10^{10}$  yr. The emphasis has been on trying to make this compilation and the subsequent reduction process as homogeneous as possible without sacrificing data integrity. We have also compiled literature estimates for the ages and metallicities of these clusters, again trying to maintain consistency as far as possible. From the *HST* observations, we have constructed surface brightness profiles for the entire sample and obtained structural parameters for each cluster, including the core radius and power-law slope at large radii. Using these parameters we have also estimated the total luminosity and mass for each cluster. These data, along with the surface brightness profiles, are available on-line at [http://www.ast.cam.ac.uk/STELLARPOPS/LMC\\_clusters/](http://www.ast.cam.ac.uk/STELLARPOPS/LMC_clusters/).

The surface brightness profiles show a rich amount of detail, with young clusters in particular exhibiting bumps, shoulders and dips in their profiles. We see evidence for double clusters in our sample, as well as post core-collapse clusters. The PCC candidates are especially interesting – the two best examples show clear power-law profiles at small radii, with slopes  $\beta \sim 0.7$  in the  $\log \mu - \log r$  plane. Our sample covers twelve of the fifteen definite old LMC globular clusters, and we are able to estimate that  $20 \pm 7$  per cent of these clusters are PCC objects, matching the 20 per cent estimated for the Galactic globular cluster system. We have also shown that R136 requires a two component fit to its profile, and that it is likely not yet in a PCC state.

If core radius is plotted against age for the entire sample, we see that while all the young clusters have compact cores, the spread in core radius increases with age, with the oldest clusters covering the full range of core radii measured. We have argued that this trend reflects real evolution in cluster structure with age. The distribution of clusters on the plot suggests a bifurcation at several hundred Myr, with most clusters maintaining small cores consistent with standard isolated globular cluster evolution, but with several moving to the upper right of the diagram and evolving large diffuse cores. We suggest that these clusters must be different to the “standard” clusters, either by having exceptional stellar populations, or by being subjected to an external influence. We are currently employing  $N$ -body simulations to explore several physical processes which fall into these categories.

## ACKNOWLEDGMENTS

We would like to thank Mark Wilkinson, Richard de Grijs and Jarrod Hurley for useful discussions and suggestions. ADM is

supported by a Trinity College ERS grant and a British government ORS award. This paper is based on observations made with the NASA/ESA *Hubble Space Telescope*, obtained from the data archive at the Space Telescope Institute. STScI is operated by the association of Universities for Research in Astronomy, Inc. under the NASA contract NAS 5-26555.

## REFERENCES

- Anderson J., King I. R., 1999, *PASP*, 111, 1095  
 Bhatia R. K., 1990, *PASJ*, 42, 757  
 Bhatia R. K., Hatzidimitriou D., 1988, *MNRAS*, 230, 125  
 Bhatia R. K., MacGillivray H. T., 1988, *A&A*, 203, L5  
 Bhatia R. K., Read M. A., Hatzidimitriou D., Tritton S., 1991, *A&AS*, 87, 335  
 Bica E., Clariá J. J., Dottori H., Santos Jr. J. F. C., Piatti A. E., 1996, *ApJS*, 102, 57  
 Bica E. L. D., Schmitt H. R., Dutra C. M., Oliveira H. L., 1999, *AJ*, 117, 238  
 Binney J., Tremaine S., 1987, *Galactic Dynamics*. Princeton University Press, Princeton  
 Brandl B., et al., 1996, *ApJ*, 466, 254  
 Campbell B., et al., 1992, *AJ*, 104, 1721  
 Chernoff D., Weinberg M., 1990, *ApJ*, 351, 121  
 Chrysovergis M., Kontizas M., Kontizas E., 1989, *A&AS*, 77, 357  
 de Grijs R., Johnson R. A., Gilmore G. F., Frayn C. M., 2002a, *MNRAS*, 331, 228  
 de Grijs R., Gilmore G. F., Johnson R. A., Mackey A. D., 2002b, *MNRAS*, 331, 245  
 de Grijs R., Gilmore G. F., Mackey A. D., Wilkinson M. I., Beaulieu S. F., Johnson R. A., Santiago B. X., 2002c, *MNRAS*, in press  
 de Oliveira M. R., Dottori H., Bica E., 1998, *MNRAS*, 295, 921  
 de Oliveira M. R., Bica E., Dottori H., 2000, *MNRAS*, 311, 589  
 de Vaucouleurs G., 1957, *AJ*, 62, 69  
 Dirsch B., Richtler T., Gieren W. P., Hilker M., 2000, *A&A*, 360, 133  
 Dutra C. M., Bica E., Clariá J. J., Piatti A. E., 1999, *MNRAS*, 305, 373  
 Djorgovski S., King I. R., 1986, *ApJ*, 305, L61  
 Djorgovski S., 1987, in Grindlay J., Philip A. G. D., eds, *Proc. IAU Symp.* 126, *Globular Cluster Systems in Galaxies*. Kluwer, Dordrecht, p. 333  
 Dolphin A. E., 2000a, *PASP*, 112, 1383  
 Dolphin A. E., 2000b, *PASP*, 112, 1397  
 Elson R. A. W., 1991, *ApJS*, 76, 185 (E91)  
 Elson R. A. W., 1992, *MNRAS*, 256, 515  
 Elson R. A. W., Freeman K. C., 1985, *ApJ*, 323, 54  
 Elson R. A. W., Fall S. M., 1988, *AJ*, 96, 1383  
 Elson R. A. W., Fall S. M., Freeman K. C., 1987, *ApJ*, 323, 54 (EFF87)  
 Elson R. A. W., Freeman, K. C., Lauer, T. R., 1989, *ApJ*, 347, L69  
 Elson R. A. W., Schade D. J., Thomson R. C., Mackay C. D., 1992, *MNRAS*, 258, 103  
 Fioc M., Rocca-Volmerange B., 1997, *A&A*, 326, 950  
 Geisler D., Bica E., Dottori H., Clariá J. J., Piatti A. E., Santos Jr. J. F. C., 1997, *AJ*, 114, 1920  
 Gilmore G., 2001, in press (astro-ph/0102189)  
 Gilmozzi R., Kinney E. K., Ewald S. P., Panagia N., Romaniello M., 1994, *ApJ*, 435, L43  
 Hill V., François P., Spite M., Primas F., Spite F., 2000, *A&A*, 364, L19  
 Hodge P. W., 1960, *ApJ*, 161, 351  
 Holtzman J., et al., 1995, *PASP*, 107, 156  
 Holtzman J., et al., 1995, *PASP*, 107, 1065  
 Hunter D. A., Shaya E. J., Holtzman J. A., Light R. M., O'Neil E. J. Jr., Lynds R., 1995, *ApJ*, 448, 179  
 Jasniewicz G., Thévenin F., 1994, *A&A*, 282, 717  
 Johnson R. A., Beaulieu S. F., Gilmore G. F., Hurley J., Santiago B. X., Tanvir N. R., Elson R. A. W., 2001, *MNRAS*, 324, 367  
 King I., *AJ*, 1962, 67, 471  
 Kontizas M., Chrysovergis M., Kontizas E., 1987, *A&AS*, 68, 147

- Kontizas M., Hadjidimitriou D., Kontizas E., 1987, *A&AS*, 68, 493
- Kroupa P., Tout C. A., Gilmore G. F., 1993, *MNRAS*, 262, 545
- Lugger P. M., Cohn H. N., Grindlay J. E., 1995, *ApJ*, 439, 191
- Lyngå G., Westerlund B. E., 1963, *MNRAS*, 127, 31
- Malumuth E. M., Heap S. R., 1994, *AJ*, 107, 1054
- Mateo M., 1987, *ApJ*, 323, L41
- Metaxa M., Kontizas E., Kontizas M., 1988, *A&AS*, 73, 373
- Meylan G., 1987, *A&A*, 184, 144
- Meylan G., 1993, in Smith G. H., Brodie J. P., eds, *ASP Conf. Ser. Vol. 48, The Globular Cluster-Galaxy Connection*. Astron. Soc. Pac., San Francisco, p. 588
- Meylan G., Djorgovski S., 1987, *ApJ*, 322, L91
- Oliva E., Origlia L., 1998, *A&A*, 332, 46
- Olsen K. A. G., Hodge P. W., Mateo M., Olszewski E. W., Schommer R. A., Suntzeff N. B., Walker A. R., 1998, *MNRAS*, 300, 665
- Olszewski E. W., Schommer R. A., Suntzeff N. B., Harris H. C., 1991, *AJ*, 101, 515
- Parmentier G., Gilmore G., 2001, *A&A*, 378, 97
- Press W. H., Teukolsky S. A., Vetterling W. T., Flannerty B. P., 1992, *Numerical Recipes in C: The Art of Scientific Computing*, (2nd Edition). Cambridge University Press, New York
- Rich R. M., Shara M. M., Zurek D., 2001, *AJ*, 122, 842
- Rohlf K., Kreitschmann J., Siegman B. C., Feitzinger J. V., 1984, *A&A*, 137, 343
- Shaklan S., Sharman M. C., Pravdo S. H., 1995, *Appl. Opt.*, 34, 6672
- Shapley H., Lindsay E. M., 1963, *Irish Astron. J.*, 6, 74
- Sirianni M., Nota A., Leitherer C., De Marchi G., Clampin M., 2000, *ApJ*, 533, 203
- Spitzer L., 1987, *Dynamical Evolution of Globular Clusters*. Princeton University Press, Princeton
- Spitzer L., Hart M. H., 1971, *ApJ*, 164, 399
- Suntzeff N. B., Schommer R. A., Olszewski E. W., Walker A. R., 1992, *AJ*, 104, 1743
- Trager S. C., King I. R., Djorgovski S., 1995, *AJ*, 109, 218
- Westerlund B. E., 1990, *A&AR*, 2, 29

This paper has been produced using the Royal Astronomical Society/Blackwell Science  $\LaTeX$  style file.

## FIGURE CAPTIONS

**Figure 1.** Observation geometry and area correction points for cluster NGC 1841. The centre of the cluster falls on WFC3 at pixel coordinates (417, 401) and is marked with a small cross. Annuli of width  $4''$  have been drawn to radius  $100''$  and the random points falling in the field of view are plotted for every second annulus.

**Figure 2.** Completeness functions for NGC 2213 (left) and NGC 2005 (right). The function for the PC is denoted by the solid line, that for WFC2 by the long-dashed line, that for WFC3 by the short-dashed line, and that for WFC4 by the dotted line. The functions have been integrated over position and colour to be a function of  $V_{555}$  magnitude only. Shown above the completeness functions are the PC F555W images of the core of each cluster, with exposure times of 120 s (NGC 2213) and 500 s (NGC 2005). The images are slightly cropped to be approximately 730 pixels ( $33''.2$ ) on a side. It is clear from these images that the core of NGC 2005 is extremely compact, on a scale less than  $\sim 160$  pixels, while NGC 2213 is well resolved even in its very centre.

**Figure 3.** An example of the inclusion of information from a short exposure to alleviate significant incompleteness due to crowding, in this case for NGC 2005. Our long exposure image of the core of this cluster is shown in Fig. 2. (a) Surface brightness profiles for all four annulus widths, calculated from the original exposure (solid circles) and short exposure (open squares). The dotted line shows the approximate radius  $r_{dev}$  at which the profiles start to deviate. (b) Completeness functions for the short exposure (solid line) and original exposure (dashed line) within  $r_{dev}$ . The completeness functions have been integrated over colour and position within  $r_{dev}$  to be a function of  $V_{555}$  only. The vertical dotted line marks the brightness limit  $V_{lim}$  imposed on the short exposure photometry to remove the offset between the two surface brightness profiles.

**Figure 4.** Surface brightness profiles for an EFF model (solid line) and empirical King model (dashed line). The profiles both have core radii of  $r_c = 10''$  and central surface brightnesses of  $\mu(0) = 17$ . For the EFF profile we have chosen  $\gamma = 2.5$  which is approximately the median value measured by EFF87 for young LMC clusters, and this implies  $a = 11''.62$  to obtain the correct  $r_c$ . For the King profile we have chosen a concentration  $c = 1.5$ , implying  $r_t = 316''$  and  $k = 16.93$ . The core and tidal radii are marked. The vertical dotted line shows the typical maximum radius for surface brightness profiles constructed in the present paper.

**Figure 5.** Background fit for NGC 2005. Models of the form of Eq. 5 were fit to the profiles with annulus widths  $3''$  (filled triangles) and  $4''$  (filled circles) beyond  $r = 20''$ . The two estimated parameters were  $a \sim 4''$  and  $\mu_0 \sim 16.9$ . The solid line shows the average of the two best-fitting models, used to determine the background level  $V_{bg} = -2.5 \log \phi = 21.83$ , marked with an arrow. Errors shown are those determined from the light distribution (Section 4.2.5) rather than the Poisson errors, which are necessarily calculated after the background subtraction but before the final fit (see text). Note the apparent under-estimation of the scatter at large radii.

**Figure 6.** Background-subtracted F555W surface brightness profiles for each of the 53 clusters in the sample. The four different annulus widths are marked with different point types:  $1''.5$  width are crosses,  $2''$  width are open squares,  $3''$  width are filled triangles, and  $4''$  width are filled circles. Error bars marked with down-pointing arrows fall below the bottom of their plot. The solid lines show the best-fit EFF profiles. For each cluster the core radius  $r_c$  is indicated and the best-fit parameters listed. When converting to parsecs, we assume an LMC distance modulus of 18.5.

**Figure 7.** Measured values of  $\gamma$  plotted against those determined by EFF87 from measurements extending to  $r \sim 250''$  for ten young clusters. Errors in the  $y$ -direction represent the random errors determined as described in Section 4.2.5 and do not include any estimation of the systematic errors which may be introduced by our background fitting algorithm. The dashed line is plotted for reference and indicates equality between the two sets of measurements.

**Figure 8.** Measured values of  $r_c$  plotted against those determined from the following studies: EFF87 (filled triangles); Mateo (1987) (filled squares); Elson (1991) (not seeing corrected) (filled circles). The cross marks the value measured for NGC 1856 by Elson (1992). Errors in the  $x$ -direction are those quoted by the various authors, and in the  $y$ -direction are those determined as described in Section 4.2.5. The dashed line is plotted for reference and indicates equality between the measurements. Radii are in arcseconds to account for the different distance moduli adopted in each study.

**Figure 9.** Images of the six clusters described in the text of Section 5.1.2. *Top left:* Our WFC2 image of the centre of NGC 1850 (lower left) and NGC 1850B (centre). The image is approximately  $70''$  (730 WFC pixels) on a side. *Top centre:* NGC 2153. *Top right:* NGC 2213. *Bottom row, left to right:* NGC 2004, NGC 2155, and NGC 2159. Each of the latter five is an  $R$ -band DSS2 image, approximately  $195''$  on a side.

**Figure 10.** Central surface brightness profiles and power-law fits for the seven PCC cluster candidates in the present sample. On the left are shown the four clusters with complete profiles; on the right those three with incomplete profiles, but which seem to exhibit breaks. The four different point styles represent the four annulus sets, as in Fig. 6. The best fitting power-law models are shown, and the radii of the breaks to the power-law regions are indicated by arrows, with errors indicated. The slopes  $\beta$  of the power-law models are listed. Note that because of the magnitude scale the slopes of the models as plotted are  $2.5\beta$ .

**Figure 11.** Two-component fits for the complete surface brightness profile of R136/NGC 2070. The four different point styles represent the four annulus sets, as in Fig. 6. We show two different two-component profiles. The solid line represents an EFF profile for the core (R136) and a King profile for the outer region, while the dashed line represents an EFF profile in the core and an EFF profile in the outer region. Best-fit parameters for each of the two models are as discussed in the text. Note that the two only differ significantly at large radii.

**Figure 12.** Power-law fit to the inner core of R136. The four different point styles represent the four annulus sets, as in Fig. 6. The best-fit EFF and power-law profiles are shown as is the power-law slope ( $\beta$ ) and break radius (arrow), just as for the PCC candidate clusters in Fig. 10. Again, because of the magnitude scale, the slopes of the power-law model as plotted is  $2.5\beta$ .

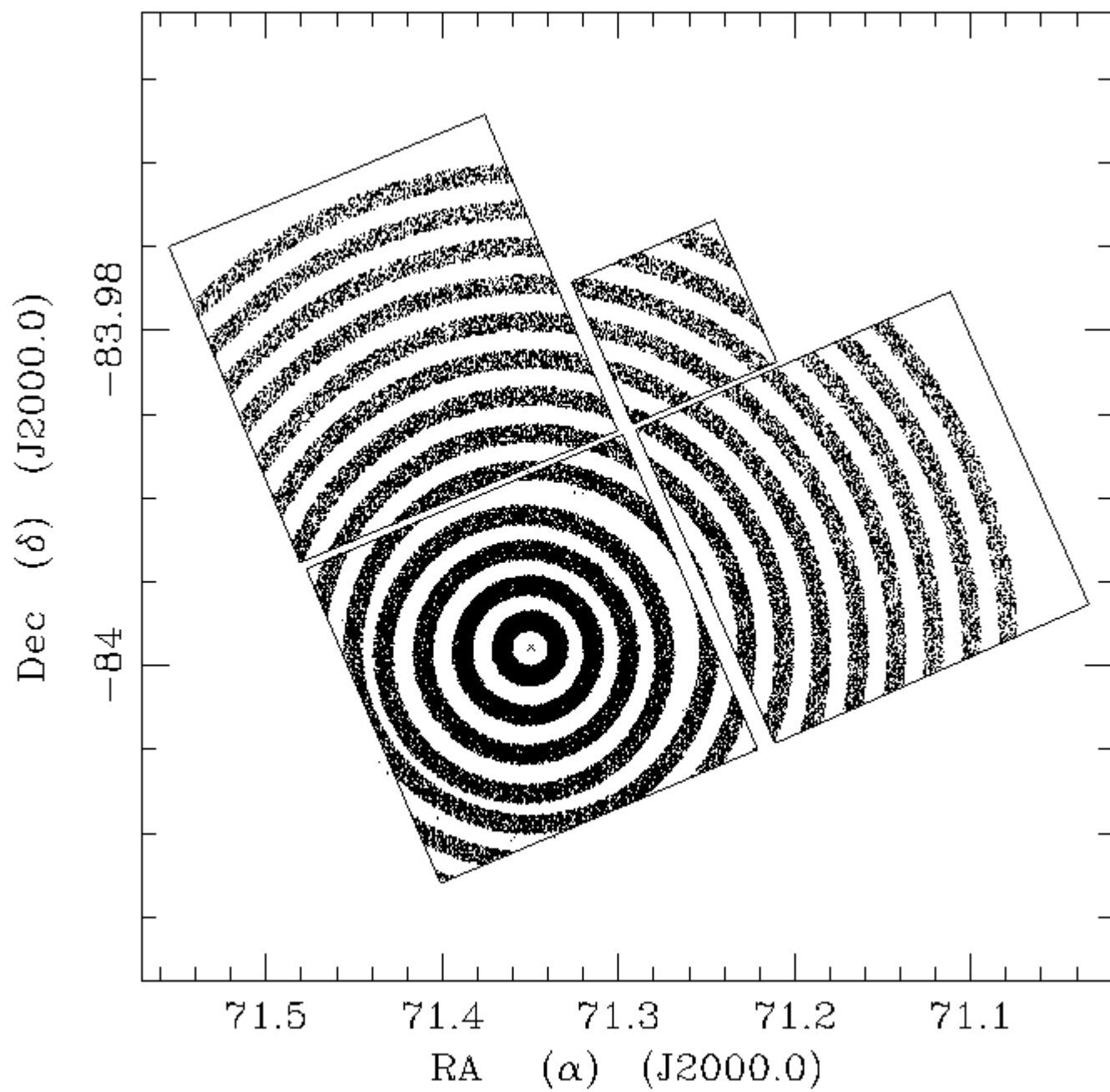
**Figure 13.** Mass to light ratios predicted from the single-burst stellar population models of Floc & Rocca-Volmerange (1997) (PEGASE v2.0, 1999), using the IMF of Kroupa, Tout & Gilmore (1993) over the mass range 0.1 to  $120M_{\odot}$ , and calculated for the four available abundances which cover the range spanned by the cluster sample:  $[\text{Fe}/\text{H}] = -2.25$  (long dashes);  $[\text{Fe}/\text{H}] = -1.65$  (solid line);  $[\text{Fe}/\text{H}] = -0.64$  (short dashes); and  $[\text{Fe}/\text{H}] = -0.33$  (dotted line).

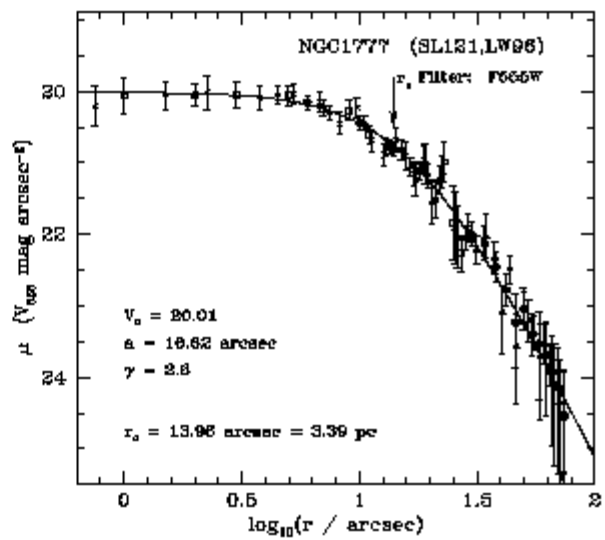
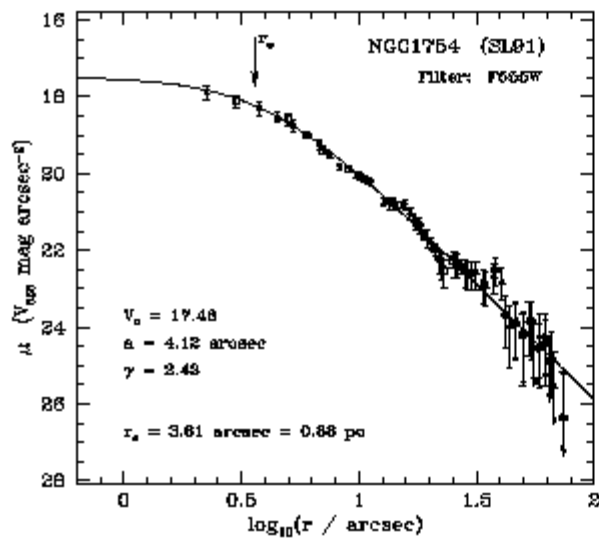
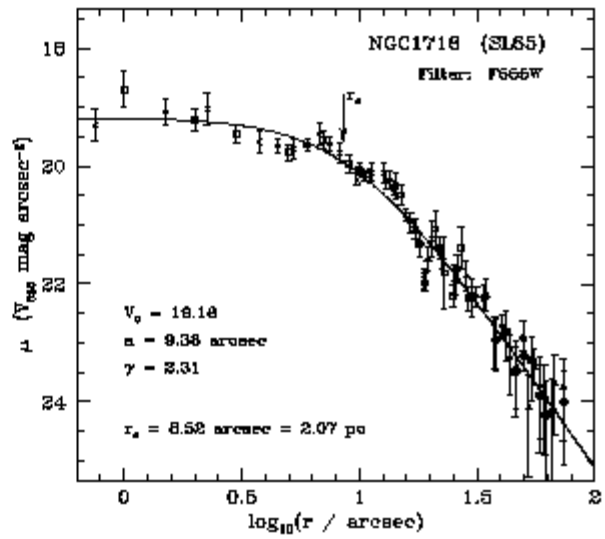
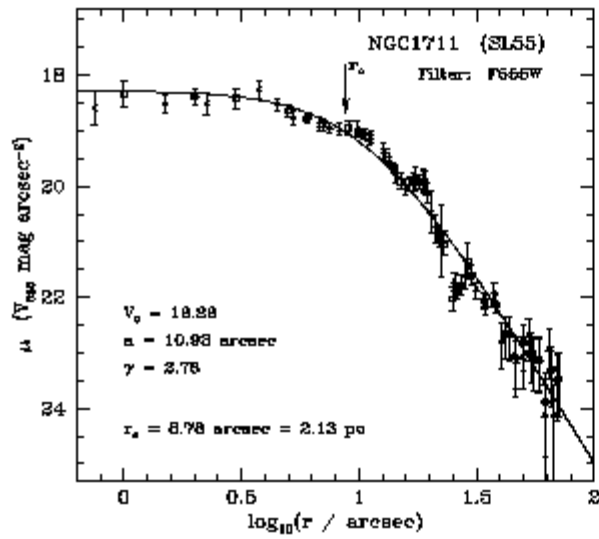
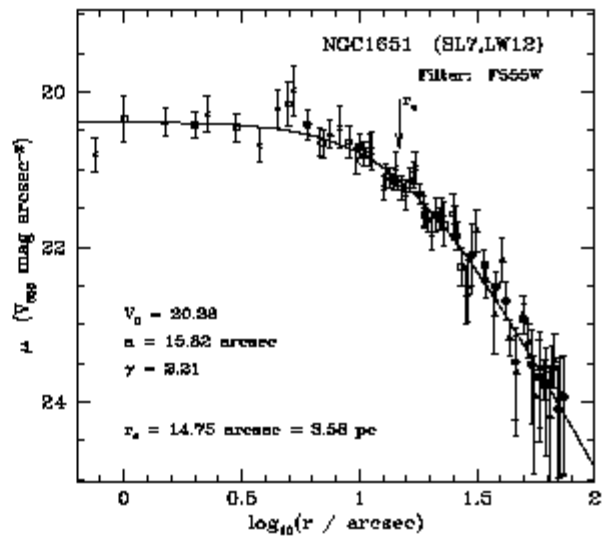
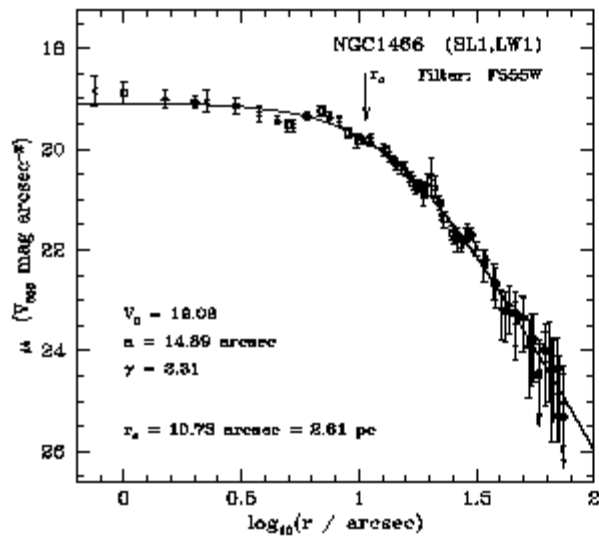
**Figure 14.** Core radius vs. age for all clusters in the sample. Ages are the literature estimates from Table 2, and the core radii as listed in Table 4. The points marking clusters with radii smaller than  $\sim 1$  pc should be considered upper limits, as discussed in Section 5.

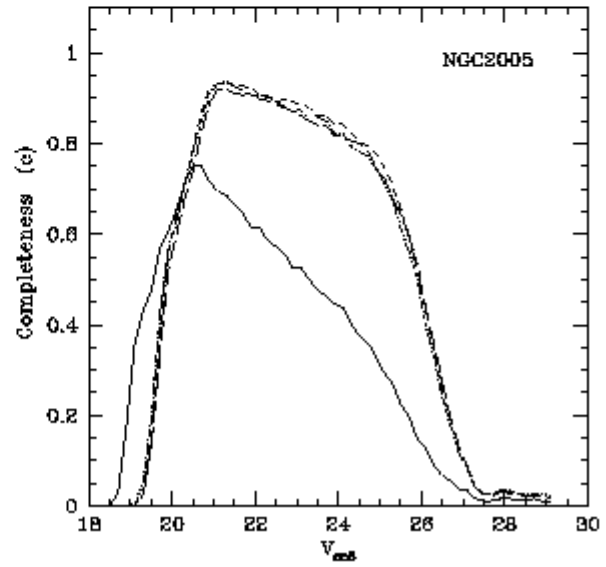
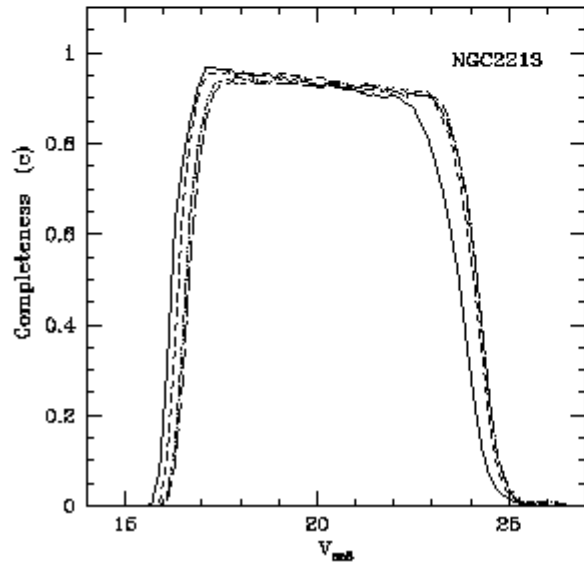
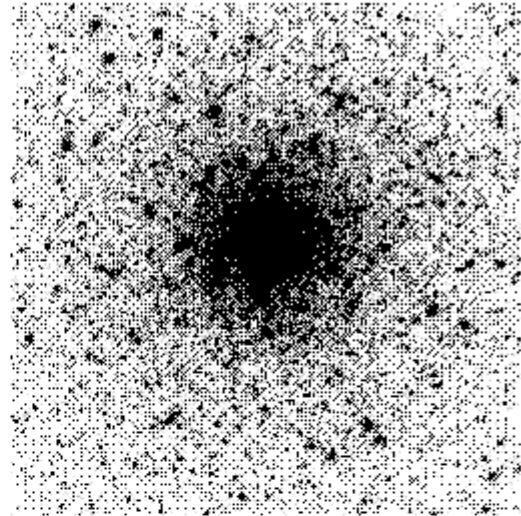
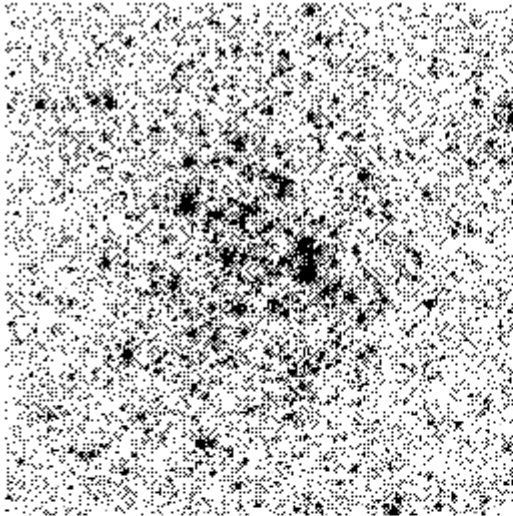
**Figure 15.** Asymptotic mass vs. age for all clusters in the sample. Again, ages are the literature estimates from Table 2, while the masses are from Table 6.

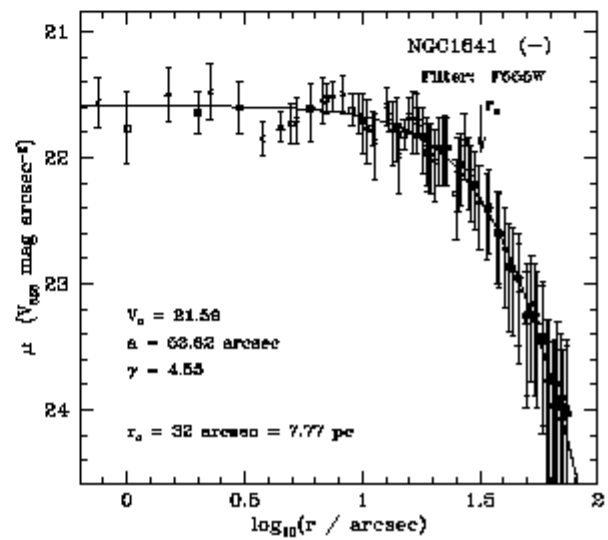
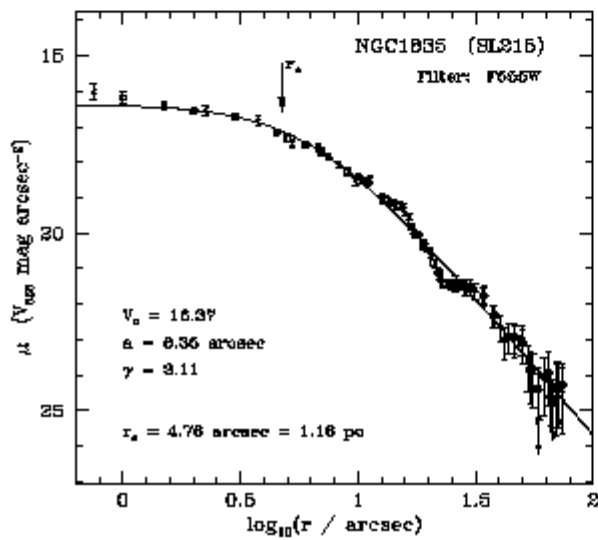
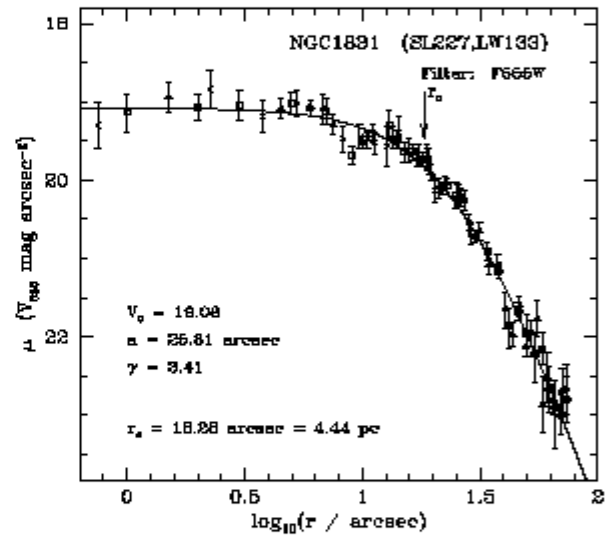
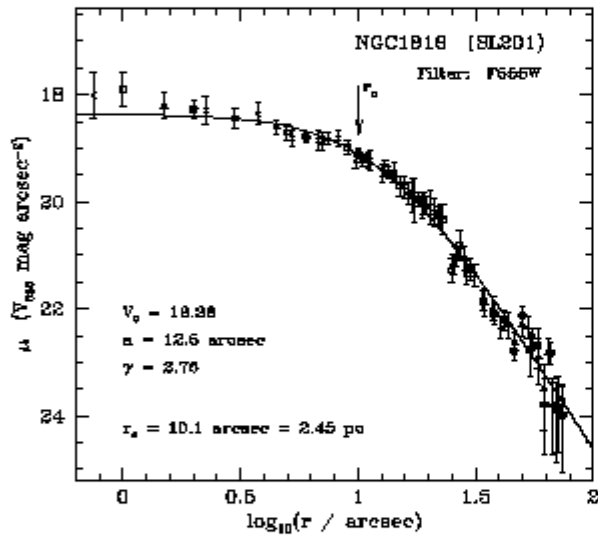
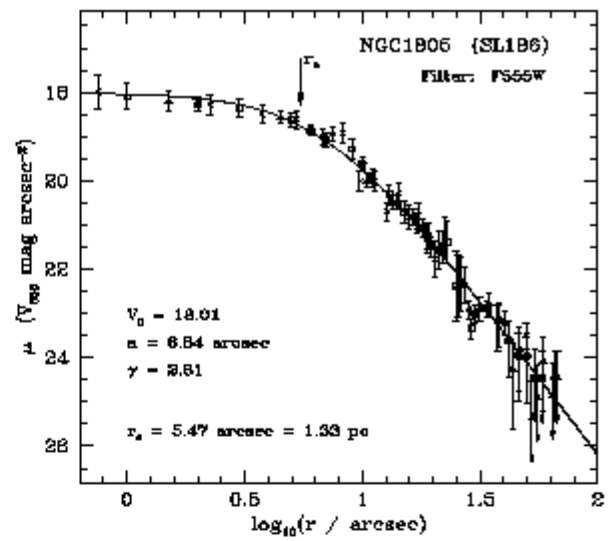
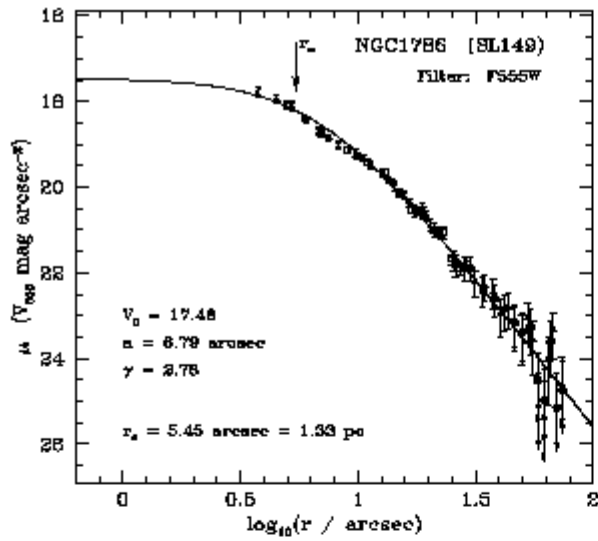
**Figure 16.** Asymptotic mass vs. core radius for all clusters in the sample. Core radii are from Table 4, and masses from Table 6.

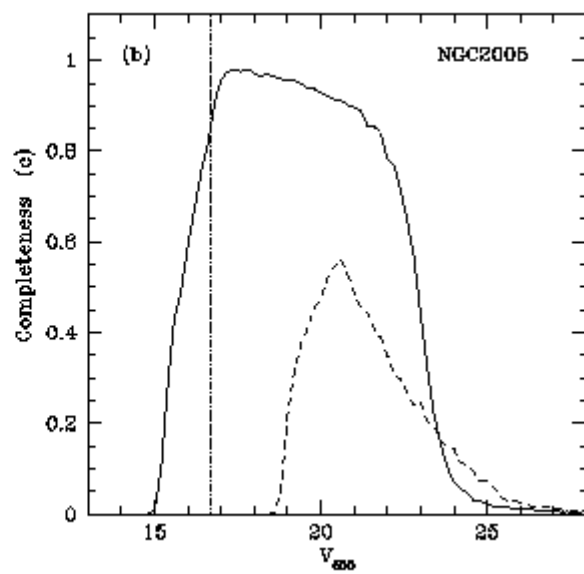
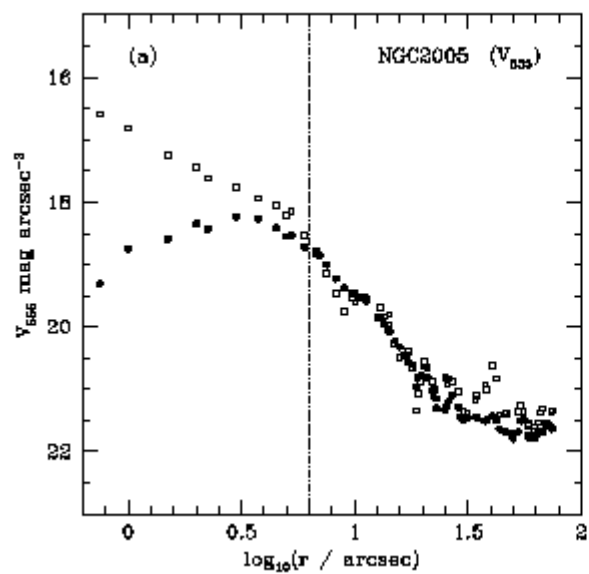


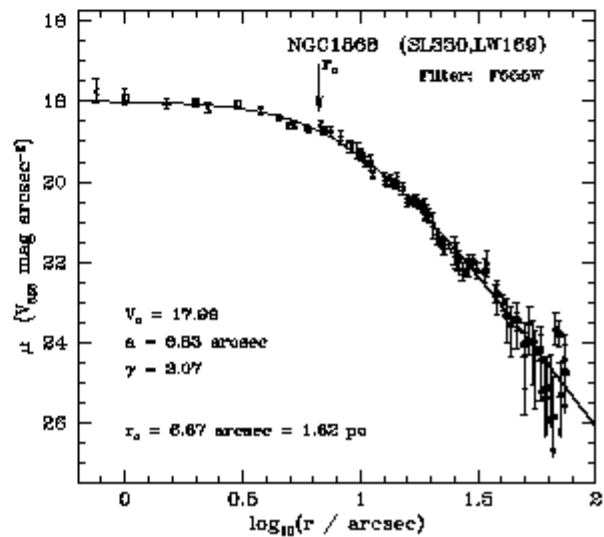
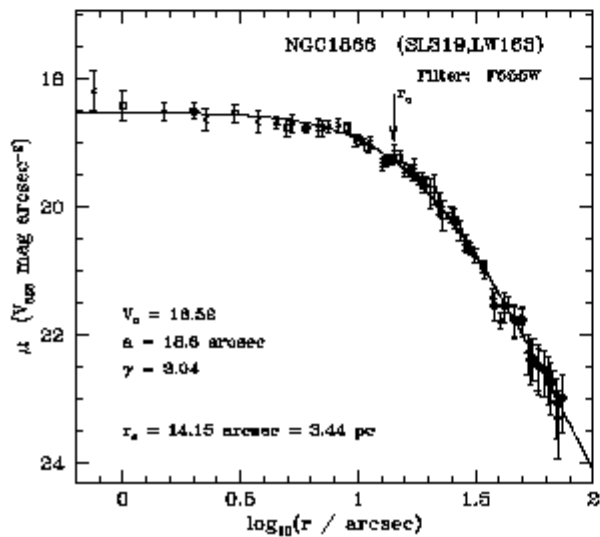
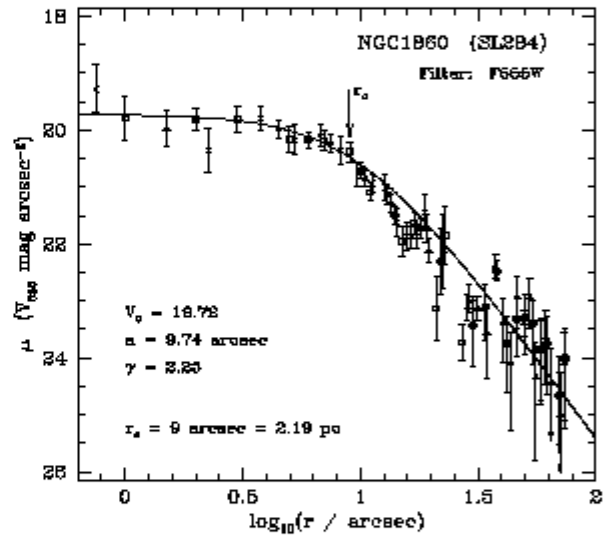
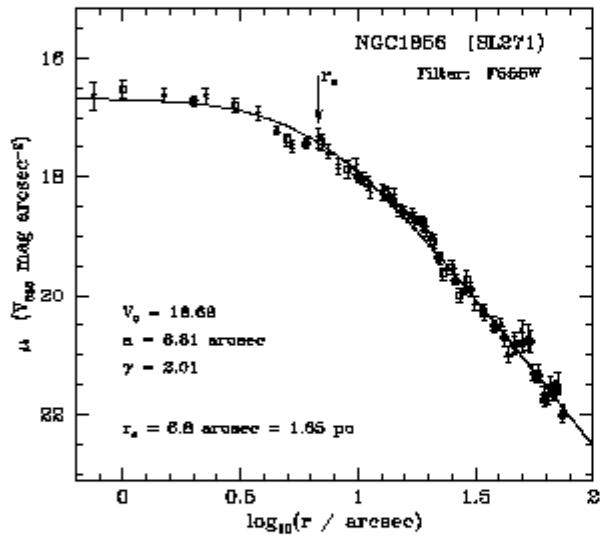
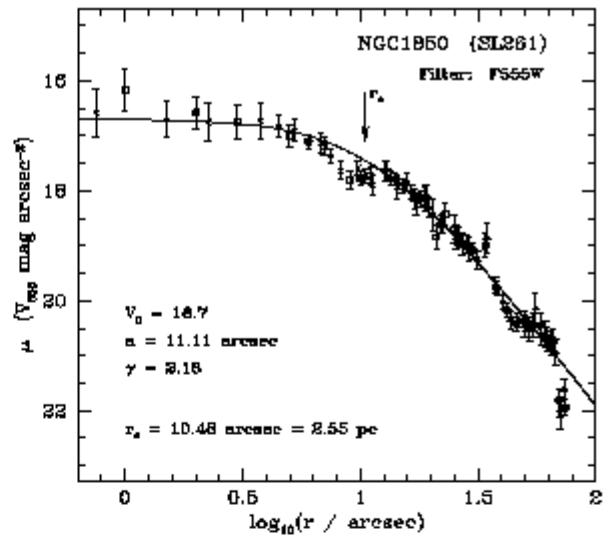
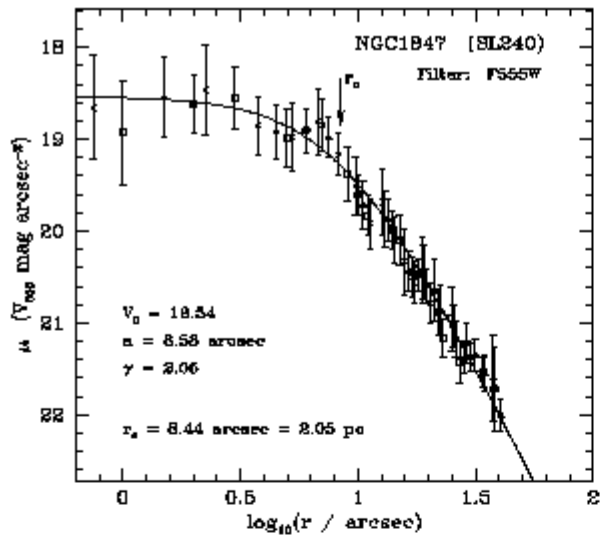


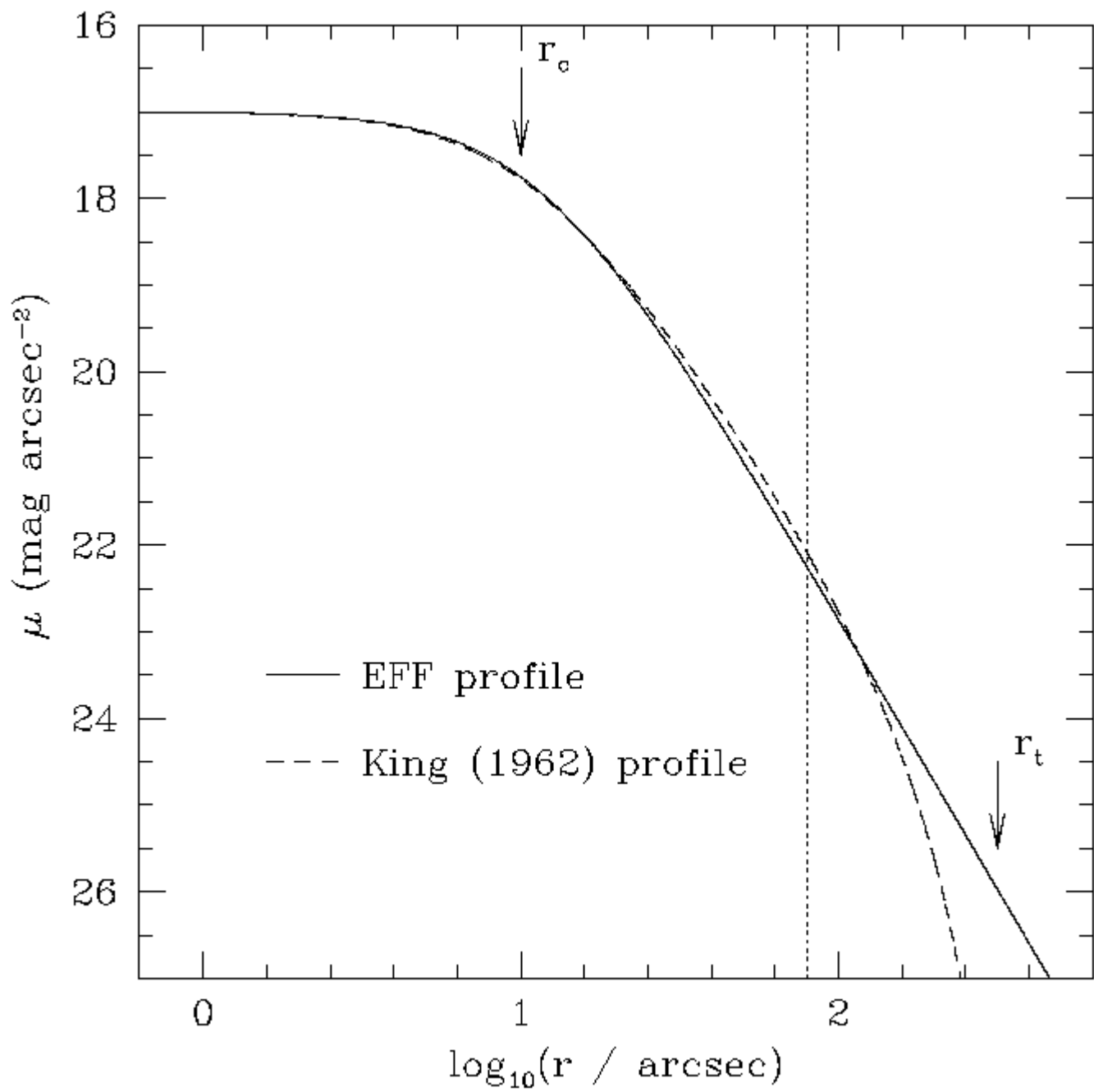


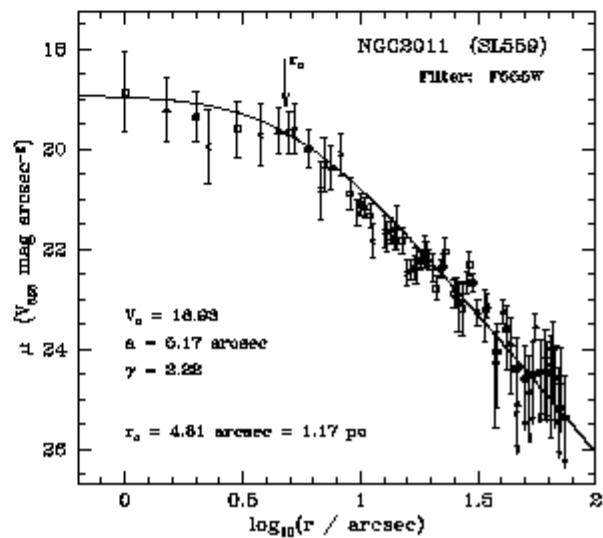
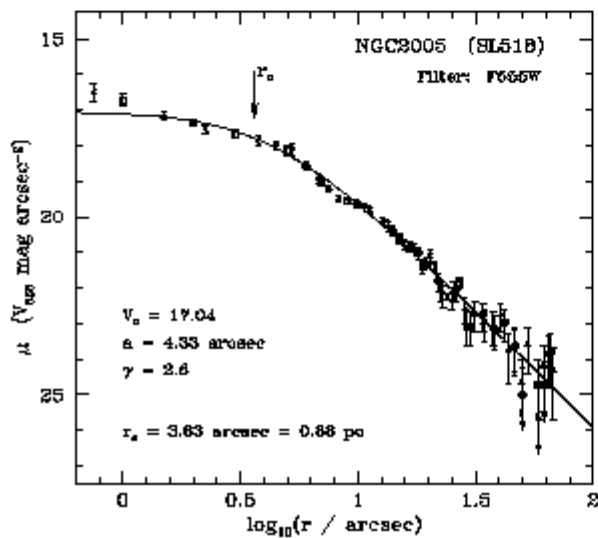
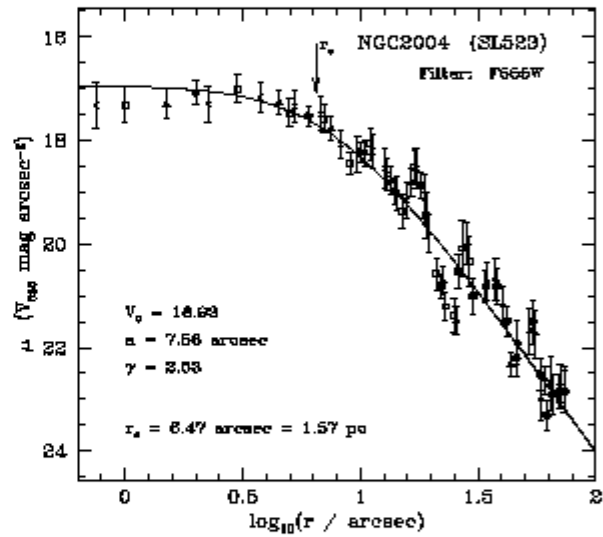
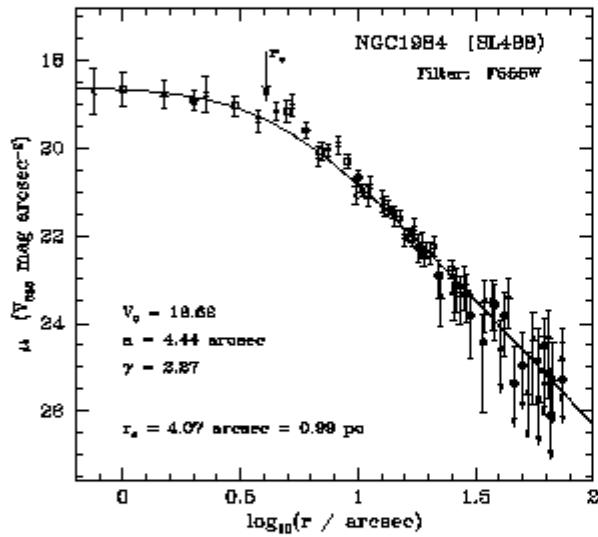
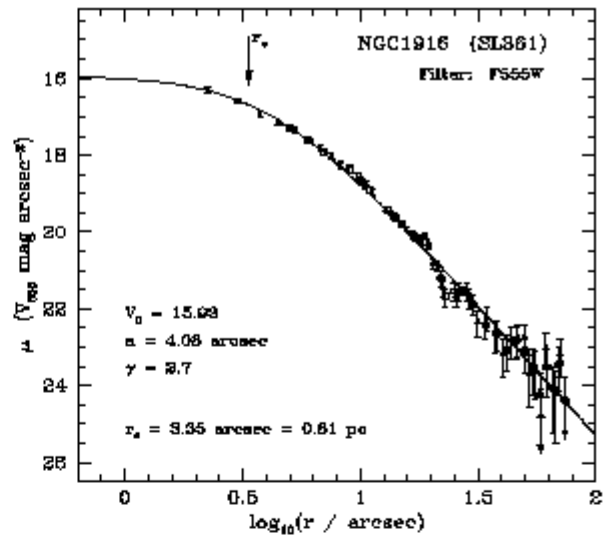
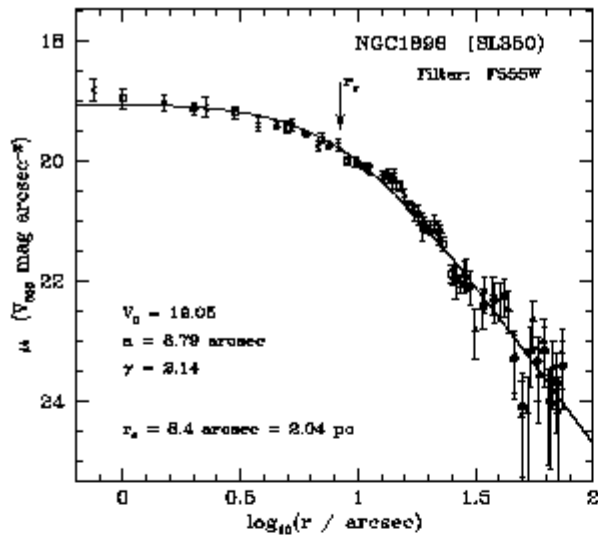




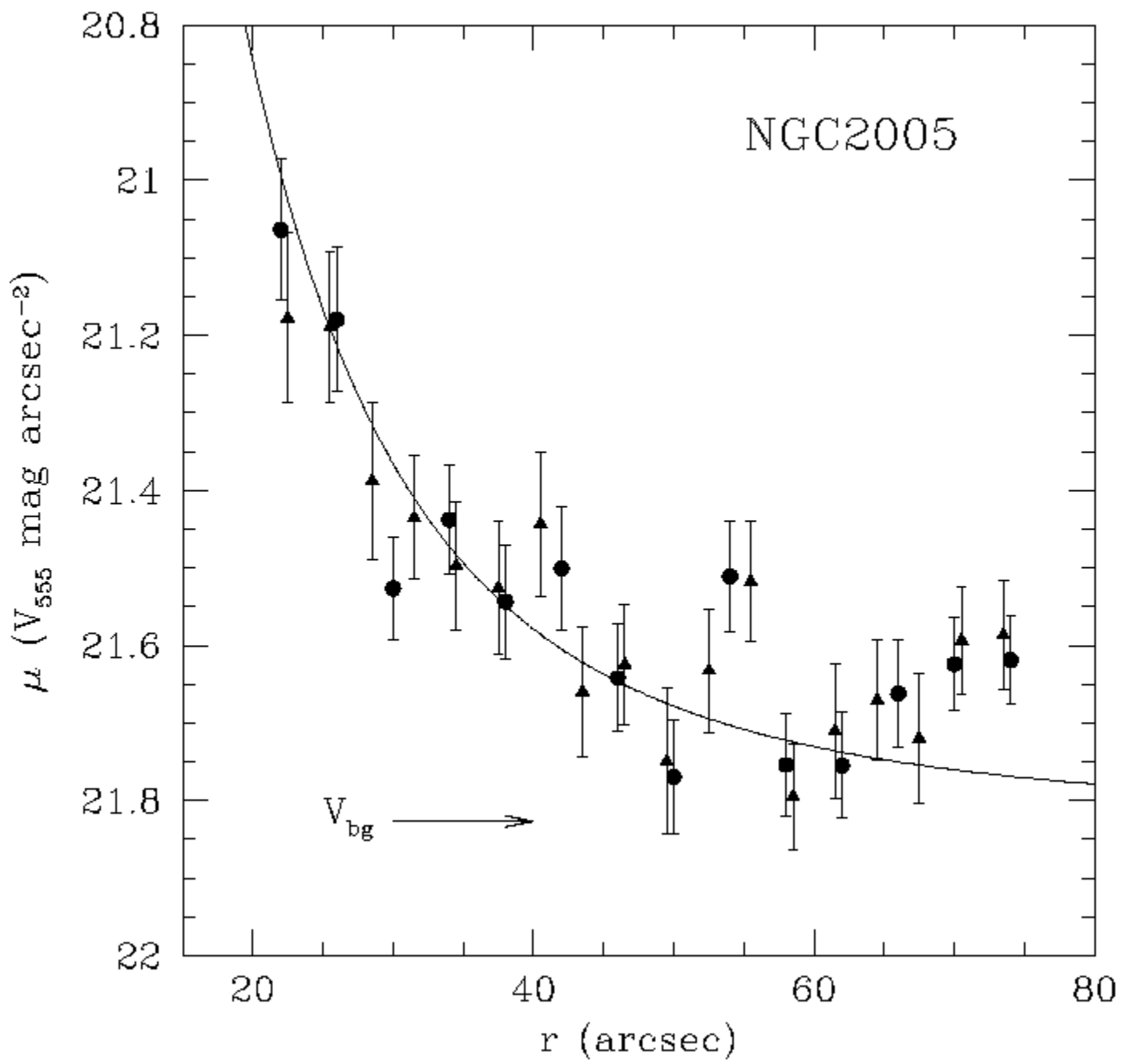


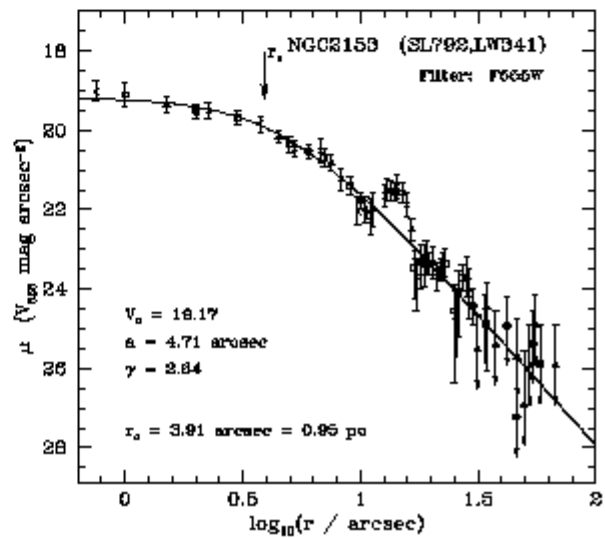
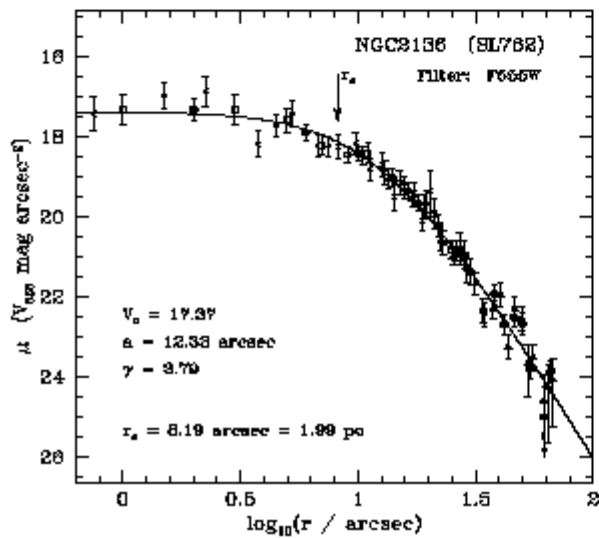
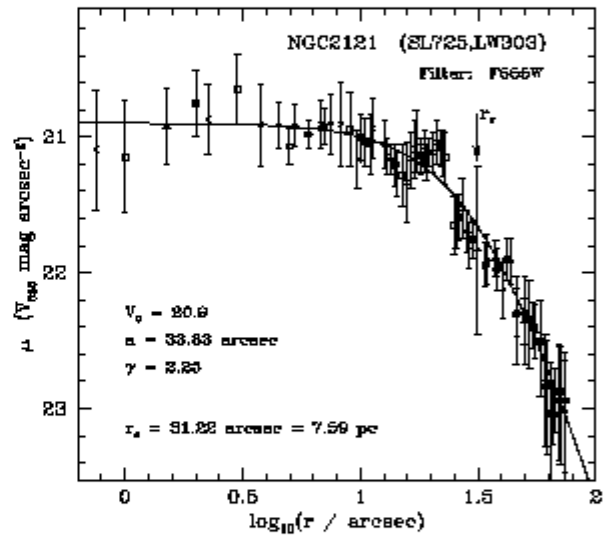
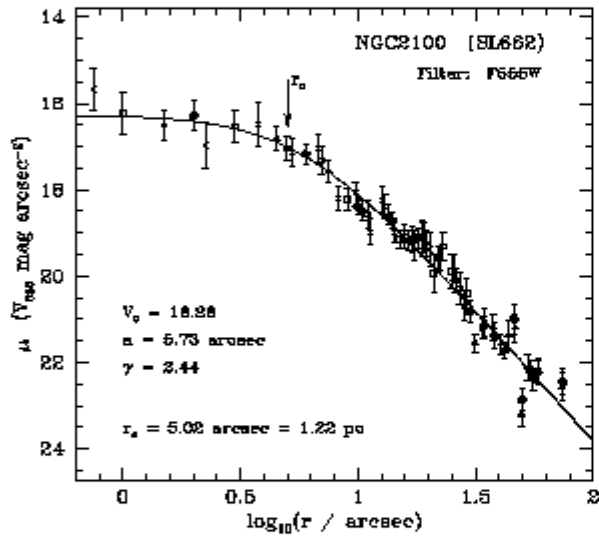
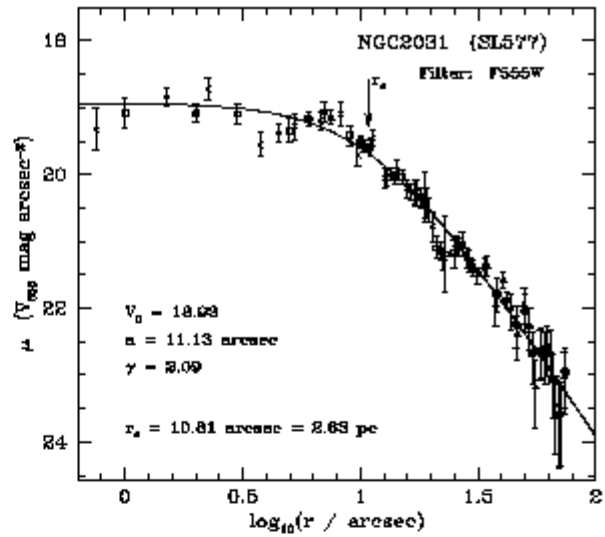
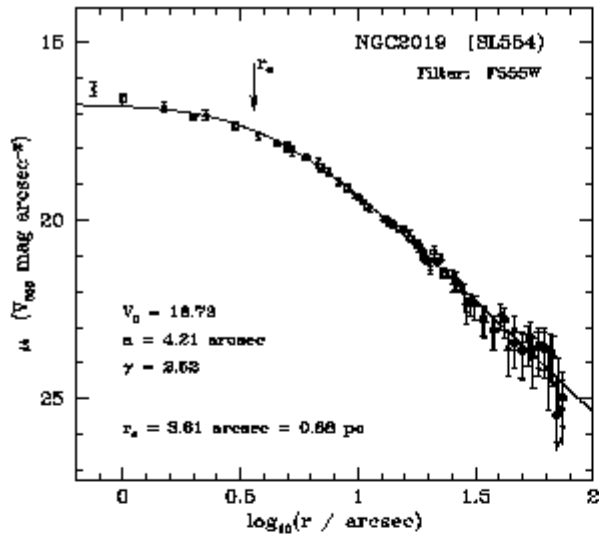


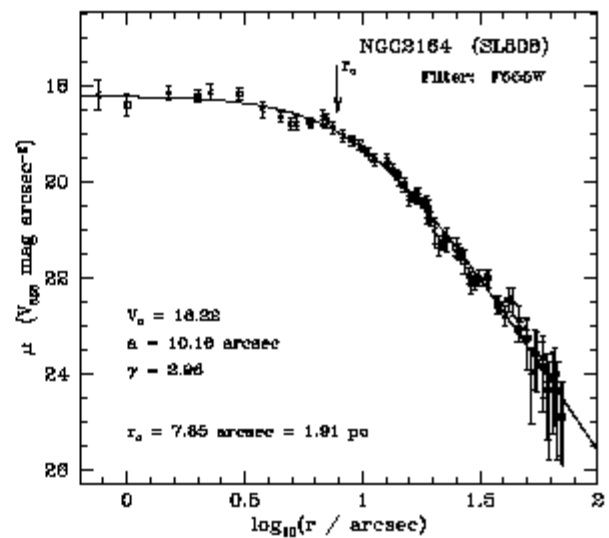
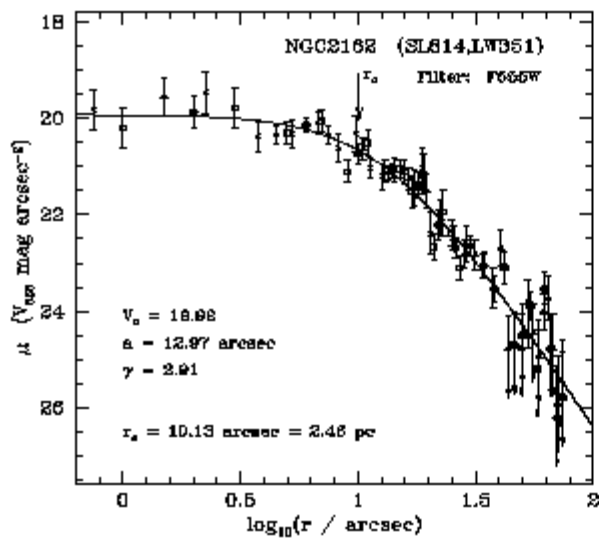
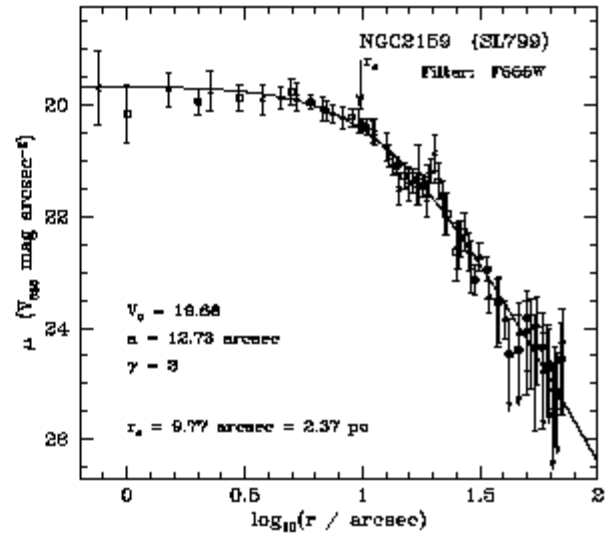
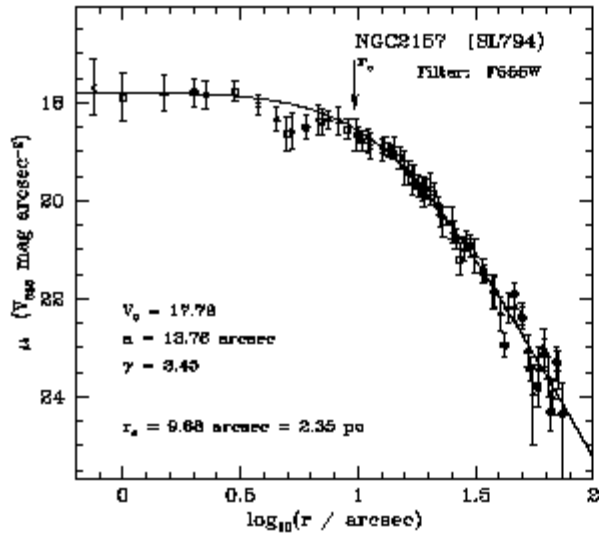
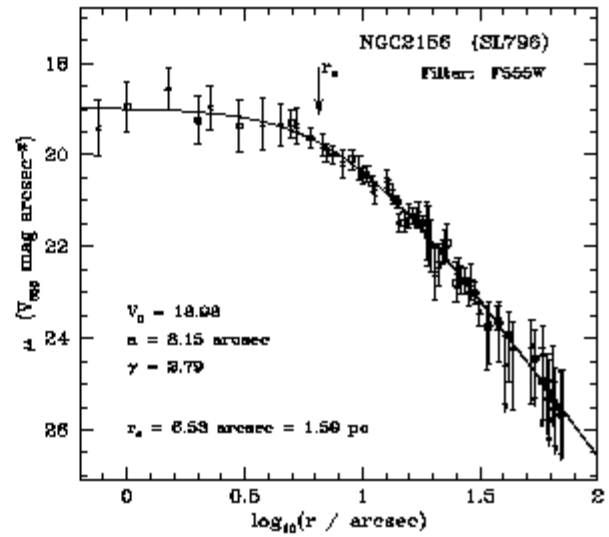
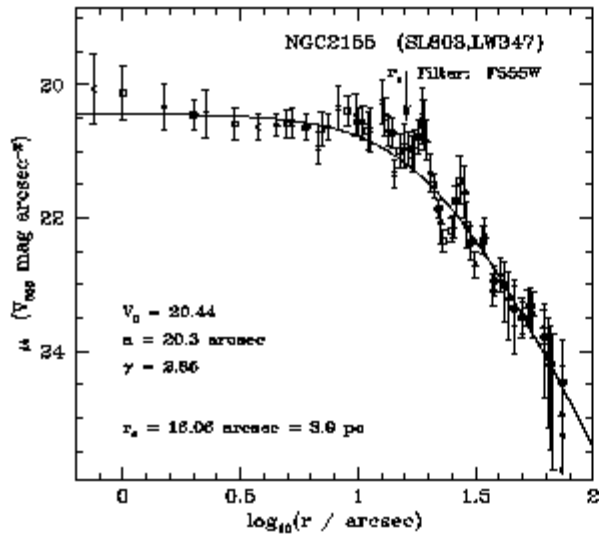


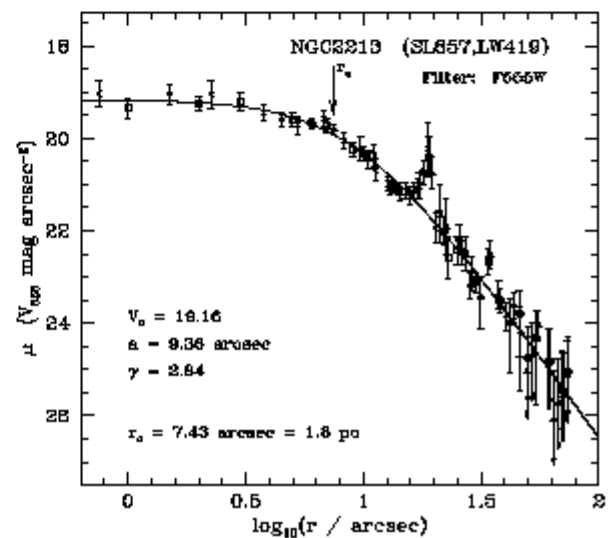
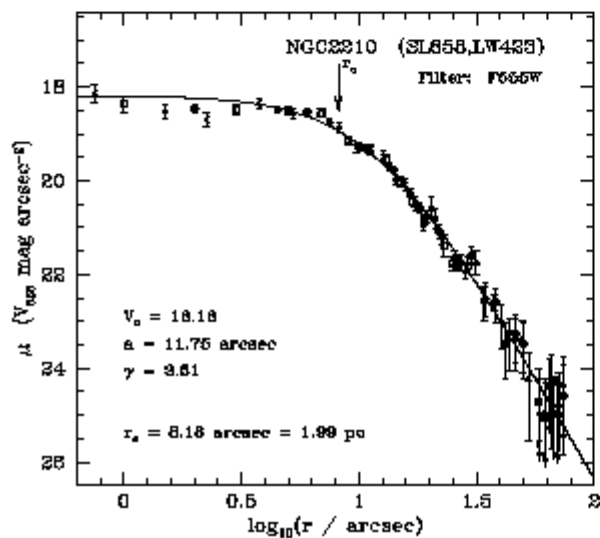
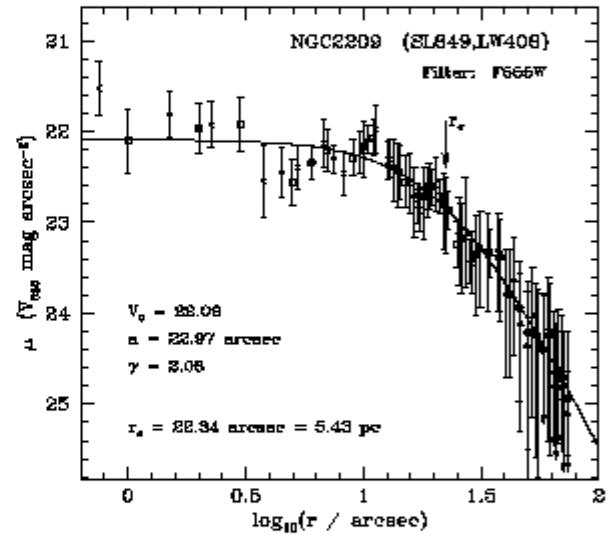
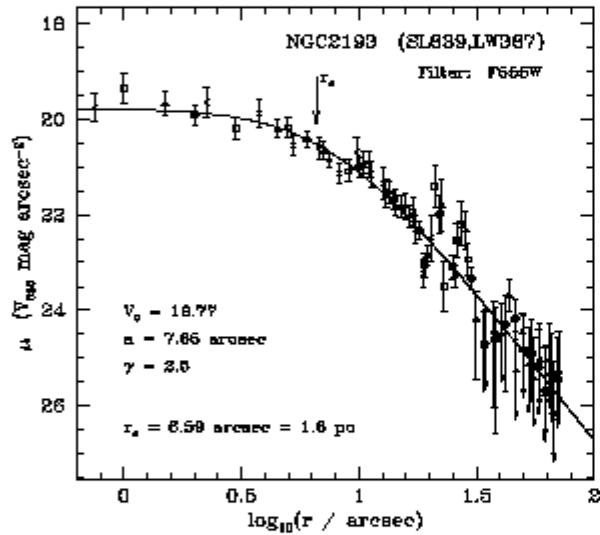
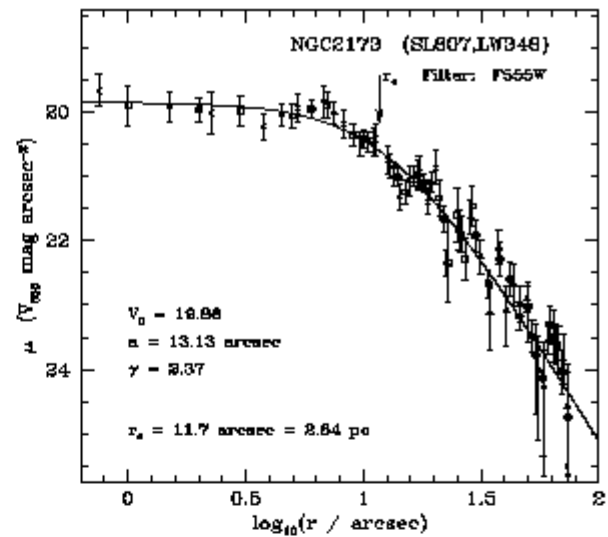
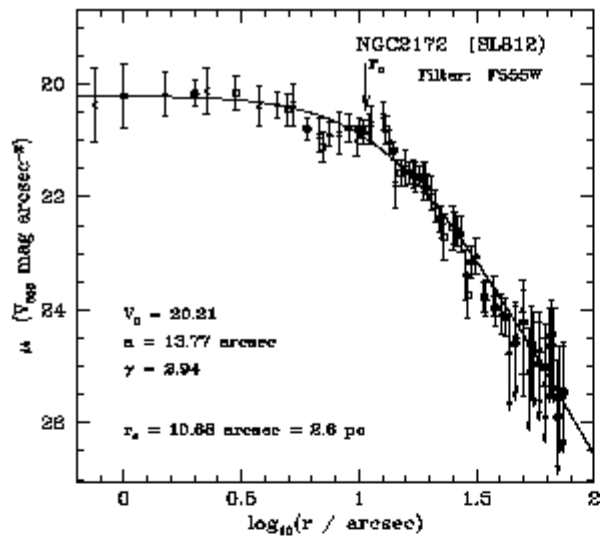


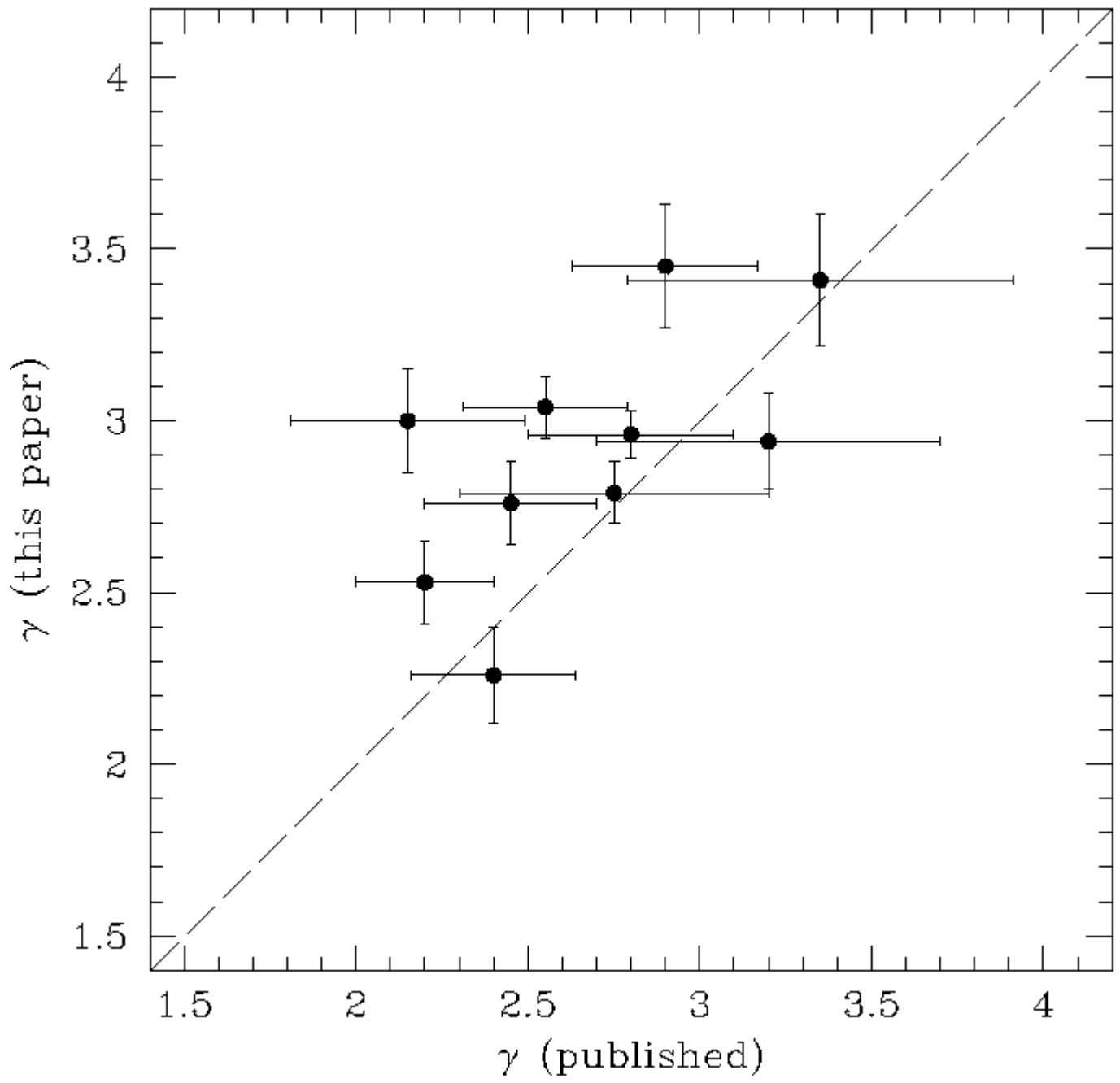


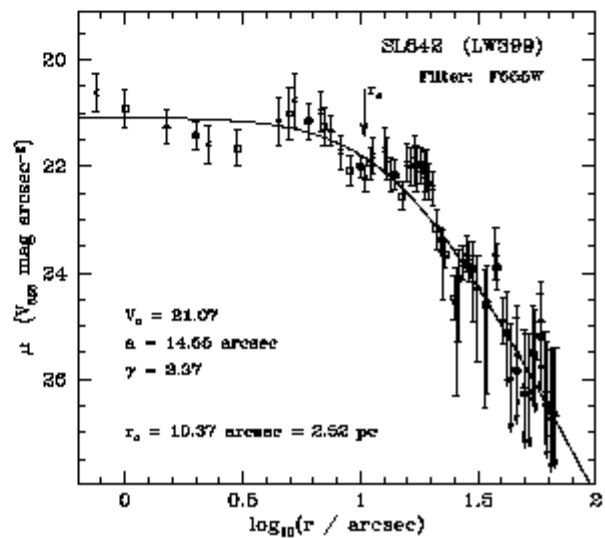
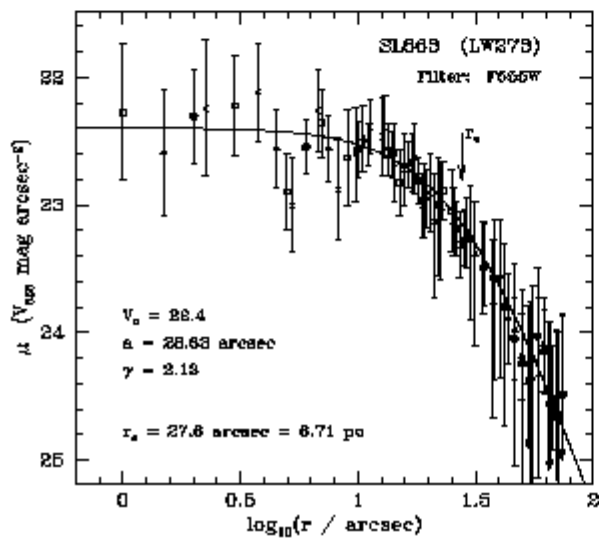
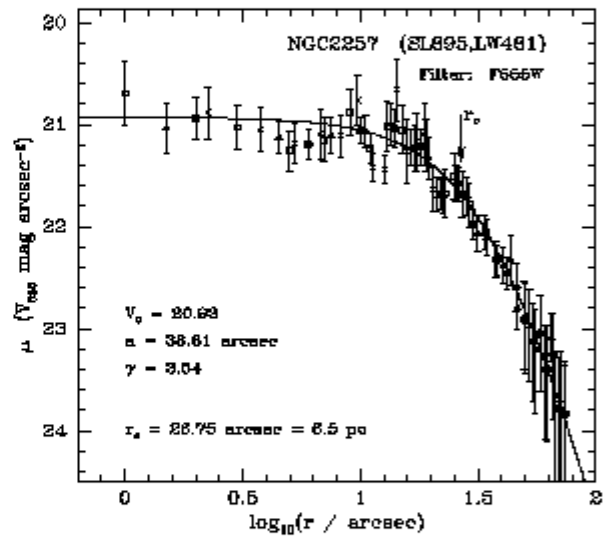
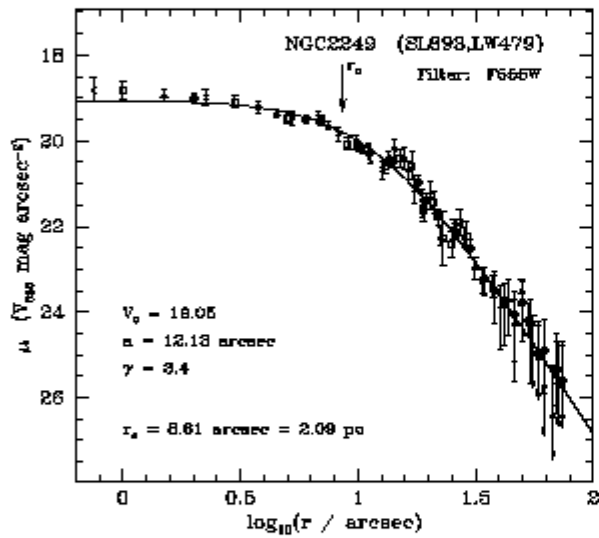
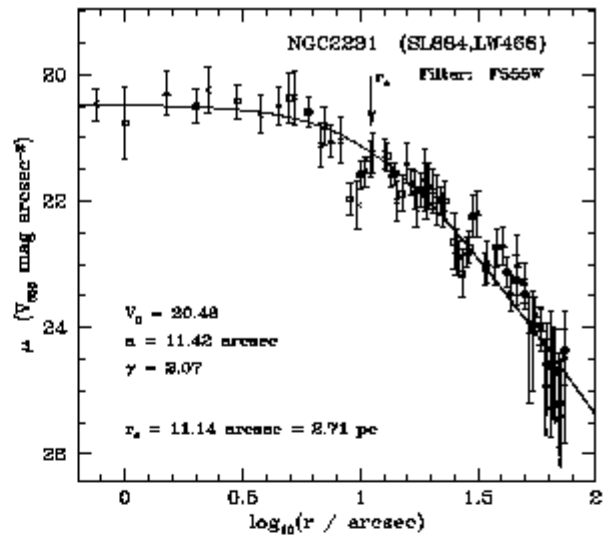
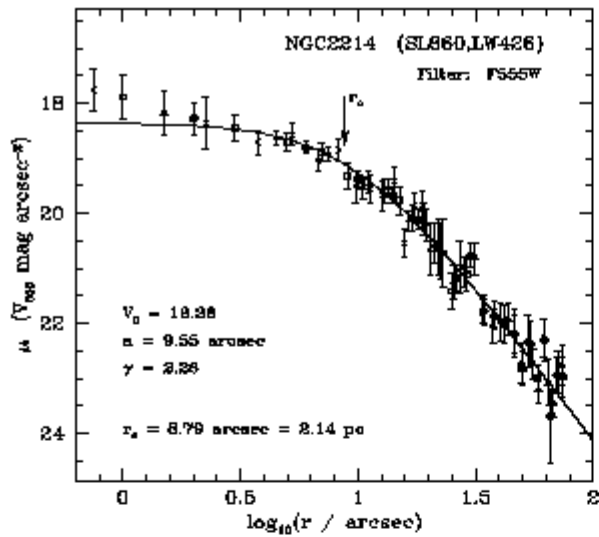


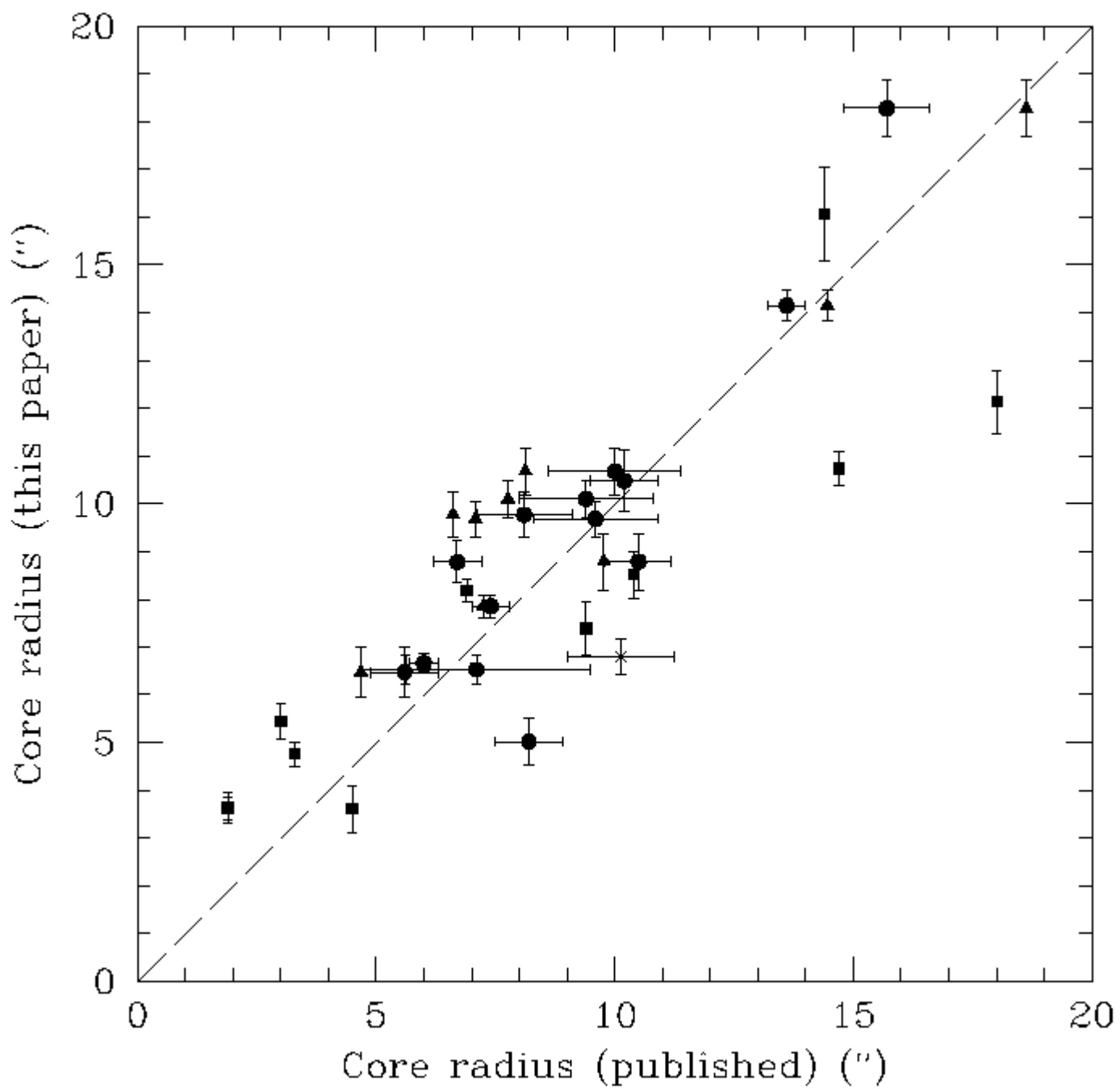












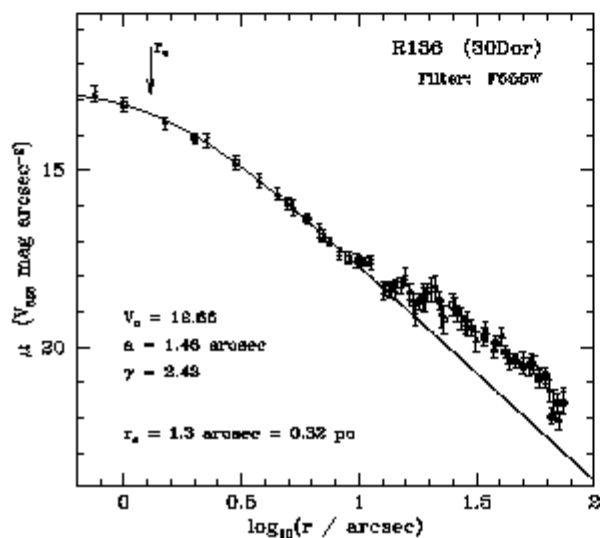
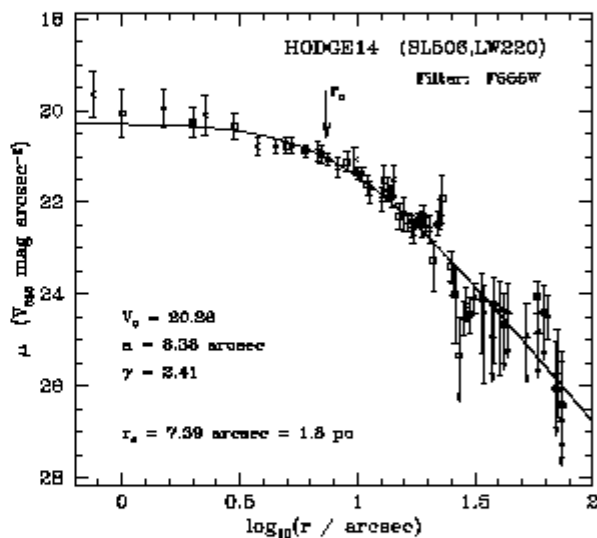
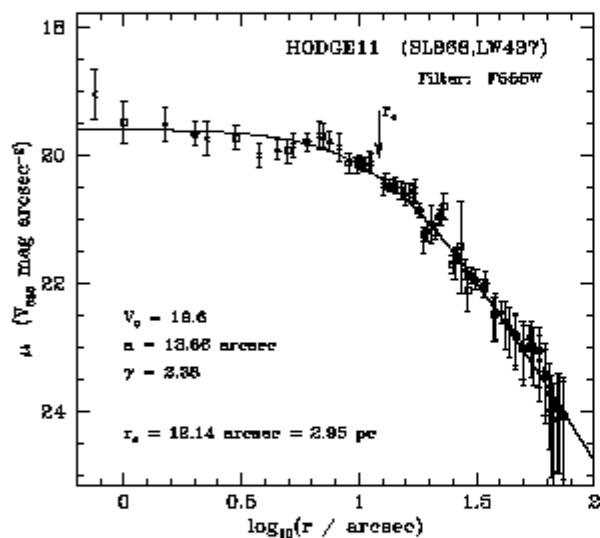
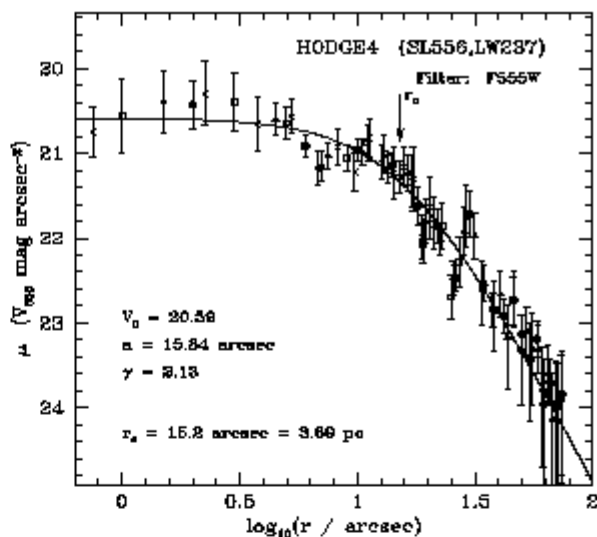
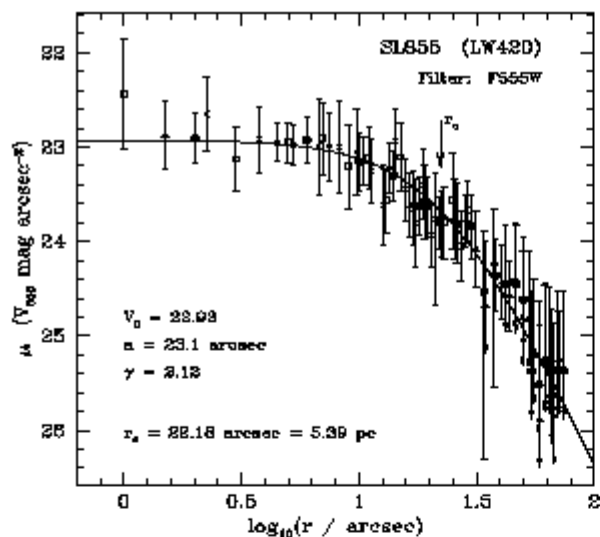


**Figure 6.** Background-subtracted F555W surface brightness profiles for each of the 53 clusters in the sample. The four different annulus widths are marked with different point types: 1''.5 width are crosses, 2'' width are open squares, 3'' width are filled triangles, and 4'' width are filled circles. Error bars marked with down-pointing arrows fall below the bottom of their plot. The solid lines show the best-fit EFF profiles. For each cluster the core radius  $r_c$  is indicated and the best-fit parameters listed. When converting to parsecs, we assume an LMC distance modulus of 18.5.



